Master's Thesis

NANOEMULSIONS FOR GENE THERAPY

June 2^{nd} 2022

Nanobiotechnology, Cristina Úbeda i Nicolau
Department of Materials and Production, Aalborg University

Department of Materials and Production
Nanobiotechnology
Skjernvej 4A
9220 Aalborg Øst

AALBORG UNIVERSITET
STUDENTERRAPPORT

Title:
Nanoemulsions for Gene Therapy

Project:
Master's Thesis

Project period:
September 3rd 2021 to June 2nd 2022

Group:
5.317

Participants:
Cristina Úbeda i Nicolau

Supervisors:
Leonid Gurevich & Peter Fojan

Number of pages:
107

Number of appendices:
1

Finish date:
June 2nd 2022

Abstract:

This project aims to test different techniques to generate nanoemulsions to encapsulate plasmid DNA and test the transfection efficiency into HeLa cells. The nanoemulsions obtained via electrospray (ES) and high-speed stirring (HSS) had sizes ranging from 200 nm up to 1,300 nm. Furthermore, different microfluidic chips were designed using AutoCAD and LayoutEditor, to be manufactured via 3D printing and soft lithography. Simulations using COMSOL® v5.6 were performed on the microfluidic chips in 2D using the level set method. The goal was to study how the geometry and channel height affected the size of the droplets. Simulations showed that flow-focusing geometries with 400 μm height channels generated droplets with sizes in the range of 60 μm, while the smallest droplets generated in the 100 μm height channels were in the 30 μm range. No results were obtained for the T-junction in either of the sizes. Transfection of the TagRFP in HeLa cells could be observed after 24 and 48 hours with the plasmid incubated with poly-L-lysine, however, no transfection was observed for the cells incubated with the droplets.

Preface

This report is written by Cristina Úbeda i Nicolau as the master thesis of the Master's degree in Nanobiotechnology at the Department of Materials and Production at Aalborg University. This project was written over a period of 10 months from September 3^{rd} to June 2^{nd} 2022, with supervision from Leonid Gurevich and Peter Fojan.

This project is focused on the encapsulation of DNA encoding a fluorescent protein (TagRFP) in nanoemulsions. The nanoemulsions will be produced using different techniques, and different microfluidic geometries, which later will be characterised by nanoparticle tracking analysis (NTA) and scanning electron microscopy (SEM). The nanoemulsions will be then incubated with mammalian cells and their transfection efficiency was evaluated by fluorescence microscopy in cooperation with AAU Health Science and Technology.

The report is written in British English and the Oxford comma is used. The references use the Vancouver citation system which means that citations will be given a number corresponding to a source in the bibliography. Figures, graphs, and tables without citations were carried out by the author. All abbreviations are defined in parenthesis in each section when mentioned for the first time.

Cristina Úbeda i Nicolau

Aalborg University, June 2^{nd} 2022

Acknowledgements

I would like to thank both Leonid Gurevich and Peter Fojan for their support and guidance throughout this thesis. Without your help, this project would not have advanced so far. I would also like to show my gratitude to Pablo Pennisi without whom the experiments with HeLa cells would not have been possible.

Thanks to my friends and family who have always believed in me even when I did not believe in myself. To Konstantinos and Kristian for making the waiting periods more bearable. And special thanks to Aleks for keeping up with me a whole year, being there at my lowest, and for making it easier to keep going.

Contents

List of Abbreviations

Name	Abbreviation
Adeno-associated Virus	AAV
Adenosine Triphosphate	ATP
Adenovirus	AV
Caveolae-mediated Endocytosis	CLIC
Charge-Coupled Device	CCD
Clathrin-mediated Endocytosis	CME
Computer-Aided Design	CAD
Cyan Fluorescent Protein	CFP
Desoxyribonucleic Acid	DNA
Drug Delivery Systems	DDS
Dulbecco's Modified Eagle Medium	DMEM
Escherichia coli	*E. coli*
Electrospray	ES
Ethanol	EtOH
Ethylenediaminetetraacetic Acid	EDTA
Fluorescence Microscopy	FM
Fluorescent Proteins	FP(s)
Guanosine Triphosphate Hydrolase	GTPase
High-Speed Stirring	HSS
Lentivirus	LV
Lysogeny Broth	LB
Mass Spectrometry	MS
Micro Electro-Mechanical Systems	MEMS
Nanoemulsions	NE
Nanoparticle Tracking Analysis	NTA
Nanoparticles	NP(s)
National Institutes of Health	NIH
Numerical Aperture	NA
Oil-in-Water	O/W

Name	Abbreviation
Phosphate Buffered Saline	PBS
Polydimethylsiloxane	PDMS
Poly-L-Lysine	pll
Quantum Dots	QD(s)
Quantum Efficiency	QE
Recombinant DNA Advisory Committee	RAC
Refractive Index	RI
Retrovirus	RV
Room Temperature	RT
Scanning Electron Microscopy	SEM
Sodium Dodecyl Sulfate	SDS
Soft lithography	SL
Ultraviolet	UV
Water-in-Oil	W/O
Yellow Fluorescent Protein	YFP
(Wild-type)Green Fluorescence Protein	(wt)GFP

Chapter 1

State of the Art

Drugs have been used to heal and prolong lives in the past by ancient populations such as Egypt, and China. However, drug formulation has been developed along with the technology. [1] Over the last 70 years, the development of new technologies, such as recombinant DNA technology, have contributed to the development of both, new methods and new pharmaceuticals to treat and address many diseases. [2]

However, even with all the technological advances, the implementation of novel drugs has been significantly slow. [2] This lack of new drugs is associated with their limited physicochemical properties, e.g., low bioavailability altogether and their difficult production. Furthermore, many conventional drugs act systemically presenting many beneficial effects, yet they also present numerous disadvantages such as side effects or low dosage due to their toxicity. [3]

The development of nanotechnology early in the 00s allowed researchers to study the exceptional properties offered by nanoparticles (NPs) due to their large surface area, stability and tunable rheology. [4] Over the years, with the development of robotics, genomics and characterisation techniques it was evident that particles in the nanometre range could be applied not only in the field of materials (i.e, quantum dots (QD)) but also in the medical and biomedical fields, nowadays being a multidisciplinary filed. [5] Their interest in biomedical applications is due to their chemical, mechanical, and biological associated with their small size. Furthermore, nano-scale particles can also self-assembly and order under certain forces (magnetic fields, pH gradients, etc.). [5]

New pharmaceutical formulations, with different modes of delivery, were developed altogether with nanotechnology. [4] Nowadays, together with cancer research, one of the main focuses is the development of drug delivery systems to overcome the disadvantages that conventional drugs present. One example are nanoemulsions, a particular class of emulsions with sizes ranging from 10 to 1000 nm. [6]

One of the approaches to generate nanoemulsions are microfluidics due to reproducibility and working with small samples (typically μL range but up to pL) associated with the reduction of reagents and therefore, lower costs. Microfluidics can allow droplet size tunability by changing parameters such as phase velocities or channel size, and allow the loading of different cargos, e.g, cells, or DNA. [7], [8]

1.1 Problem Analysis

An important and long-term goal of the pharmaceutical industry is to develop new therapeutic agents that can overcome drawbacks present in conventional drugs such as poor aqueous solubility, inadequate and/or non-specific biodistribution, cytotoxicity, or the poor drug distribution throughout the tissue or organ. [9]–[11] One interesting approach to overcome these drawbacks is the use of nanoemulsions as drug delivery systems, as their reduced size modifies the pharmacokinetics of the drug. [9], [12] Another interesting property of nanoemulsions is that they can be used to encapsulate both hydrophobic and hydrophilic drugs by exchanging the continuous and dispersed phases, generating oil-in-water (O/W) or water-in-oil (W/O) emulsions respectively. [4], [13]–[15] Nowadays, W/O emulsions are being used as drug carriers, but nanoemulsions are also being used in cosmetics and pesticides among others. [4], [16]–[19]

1.2 Problem Statement

In this project, the goal is to generate water/oil submicron droplets using different techniques such as electrospray, high-speed stirring and microfluidics to encapsulate a plasmid a red fluorescent protein (TagRFP) for later transfection into mammalian cells i.e., HeLa cells. The microfluidic systems are to be designed with AutoCAD and LayoutEditor, and manufactured by 3D printing and soft-lithography. The microfluidic systems will also be simulated using COMSOL Multiphysics® to study the best parameters for droplet generation. The transfection efficiency into HeLa cells will be studied with fluorescence microscopy

Chapter 2

Introduction

The focus of this chapter is on the main topics that are relevant to the project and the experiments carried out to investigate the problems discussed in chapter one.

2.1 Gene Therapy

Gene delivery has been the focus of research since 1928, when Frederick Griffith infected mice with a mixture of living bacteria of the non-virulent R form of Type I *pneumococcus* and heat-inactivated bacteria of the virulent S form of Type II *pneumococcus* resulting in the mice death concluding that the *pneumococcus* converted the R form to the S form, and transformed from Type I to Type II. [20] Over time different genetic transfer mechanisms were discovered: conjugation in 1947 by Tatum and Lederberg, transduction in 1952 by Zinder and Lederberg, and due to viral infections in 1961 by Temin. [21]–[23]

Even though the discoveries of genetic transfer mechanisms along with cell transformation studies lead to the thought that genetic diseases could be treated using genetic engineering, it wasn't until 1988 when the Recombinant DNA Advisory Committee (RAC) approved the first clinical protocol to introduce a foreign gene into humans. [20] The introduction of a foreign gene into a cell is known as gene therapy which is a biotechnological technique that uses genes to produce a therapeutic effect or to treat a disease by genetically modifying cells, by delivering genetic material to the nucleus of the cell. [20], [24]–[27]

Since the first clinical trial was approved in 1988 more than 2600 gene therapy clinical trials have been carried out over the last decades, and most of them are still in phase I, I/II, or II; and only 22 have been approved as gene therapy drugs. [20], [28]–[30] The majority of the trials, up to 65%, aim to treat cancer, followed by monogenic and cardiovascular diseases. [20], [28], [30]

One of the main challenges of gene therapy is protecting the DNA from being degraded DNases in both *in vivo* and *in vitro* systems which can be avoided by encapsulating the DNA into vectors. An ideal vector should have specific gene delivery, transfer precise amounts of genetic material, accommodate genes of different sizes, long-term gene expression, non-toxic, non-immunogenic, and safe. [24], [31]

Viral vectors such as retrovirus (RV), adenovirus (AD), adeno-associated virus (AAV), and lentivirus (LV) have been the most commonly used vectors due to their transfection

efficiency, and simple preparation and administration. [29], [32] However, using viral vectors entails drawbacks like high toxicity, immunogenicity, mutagenicity, low target cell specificity, unsuitability for large-sized genes, and high cost.[32], [33] To overcome this, non-viral systems have been developed.

2.1.1 Non-Viral Vectors

During the past decades, non-viral vectors, which are synthetic and based on not viral vectors, have been the focus of researchers to overcome the problems associated with viral vectors for gene delivery. [30] Several non-viral vectors have been developed where the nanoparticle-based carriers are the most promising such as polymeric nanoparticles (NPs), inorganic or metal NPs, quantum dots (QDs), dendrimers, liposomes, or micelles. [30], [32]

Even though non-viral vectors have lower transfection efficiency compared to viral vectors, they are cheaper, safer, and their production can be upscaled. [26], [30]–[32] Furthermore, the nanoparticle-complexes can be modified reducing their toxicity and enhancing their stability and cell specificity. [32], [34]

One of the major advantages of polymeric NPs over other nanoparticulate-complexes is their customisation, as their composition can be selected depending on their function or target cell. Moreover, polymeric NPs have higher loading capacity and offer protection

2.1.2 Red Fluorescent Protein

After the discovery of the green fluorescent protein (GFP), other fluorescent proteins (FPs) were developed using mutagenesis on the wtGFP, obtaining different FPs such as cyan fluorescent protein (CFP), or yellow fluorescent protein (YFP). [35] It was in 1999 that GFP-like proteins were isolated from different *Anthozoa* spices. [36], [37] However, natural FPs in the orange to far-red spectra, such as DsRed, are dimeric or tetrameric making them unsuitable for fusion tags or proteins as they tend to aggregate and perturbate the function of a fused protein [35], [38]–[42] To overcome these problems mutagenesis, both random and directed, was performed to DsRed obtain monomeric variants known as "mFruits", yet, these variants are significantly less bright. [36], [38], [41], [43], [44]
The eqFP578 protein is a dimeric red GFP-like protein, from the sea anemone *Entacmaea quadricolor* which shares a 76% homology with eqFP611, a protein with a *trans*-isomerised state of the chromophore. [38], [45] Since both proteins contain the same chromophore-forming amino acid triad Met-Tyr-Gly (marked yellow below), it is assumed that the eqFP578 protein also has a *trans*-isomerised state of the chromophore associated with a higher fluorescence brightness. [38], [46], [47]

```
eqFP578    MSELIKENMH MKLYMEGTVN NHHFKCTSEG ERKPYEGTQT MKIKVVEGGP   50
TurboRFP   MSELIKENMH MKLYMEGTVN NHHFKCTSEG EGKPYEGTQT MKIKVVEGGP   50

eqFP578    LPFAFDILAT SFMYGSKTFI NHTQGIPDLF KQSFPEGFTW ERITTYEDGG  100
TurboRFP   LPFAFDILAT SFMYGSKAFI NHTQGIPDFF KQSFPEGFTW ERITTYEDGG  100

eqFP578    VLTATQDTSL QNGCIIYNVK INGVNFPSNG SVMQKKTLGW EANTEMLYPA  150
TurboRFP   VLTATQDTSF QNGCIIYNVK INGVNFPSNG PVMQKKTRGW EANTEMLYPA  150

eqFP578    DGGLRGHSQM ALKLVGGGYL HCSFKTTYRS KKPAKNLKMP GFHFVDHRLE  200
TurboRFP   DGGLRGHSQM ALKLVGGGYL HCSFKTTYRS KKPAKNLKMP GFHFVDHRLE  200

eqFP578    RIKEADKETY VEQHEMAVAK YCDLPSKLGH R-------               231
TurboRFP   RIKEADKETY VEQHEMAVAK YCDLPSKLGH R-------               231
```

Merzlyak *et al.* optimised eqFP578 protein via random mutagenesis obtaining the dimeric protein TurboRFP protein with an excitation peak at 553 nm and an emisson peak at 574 nm compared to the 552/578 nm (excitation/emission) of eqFP578. With the following random mutations R32G, T68A, L79F, L110F, S131P, and L138R (marked green). [38]

```
TurboRFP   MSELIKENMH MKLYMEGTVN NHHFKCTSEG EGKPYEGTQT MKIKVVEGGP   50
pTagRFP    MSELIKENMH MKLYMEGTVN NHHFKCTSEG EGKPYEGTQT MRIKVVEGGP   50

TurboRFP   LPFAFDILAT SFMYGSKAFI NHTQGIPDFF KQSFPEGFTW ERITTYEDGG  100
pTagRFP    LPFAFDILAT SFMYGSRTFI NHTQGIPDFF KQSFPEGFTW ERVTTYEDGG  100

TurboRFP   VLTATQDTSF QNGCIIYNVK INGVNFPSNG PVMQKKTRGW EANTEMLYPA  150
pTagRFP    VLTATQDTSL QDGCLIYNVK IRGVNFPSNG PVMQKKTLGW EANTEMLYPA  150

TurboRFP   DGGLRGHSQM ALKLVGGGYL HCSFKTTYRS KKPAKNLKMP GFHFVDHRLE  200
pTagRFP    DGGLEGRSDM ALKLVGGGHL ICNFKTTYRS KKPAKNLKMP GVYYVDHRLE  200

TurboRFP   RIKEADKETY VEQHEMAVAK YCDLPSKLGH R-------               231
pTagRFP    RIKEADKETY VEQHEVAVAR YCDLPSKLGH K-------               231
```

Performing several rounds of mutagenesis on the TurboRFP, Merzlyak *et al.* obtained the final variant named TagRFP. There are 21 mutations in total were K42R, K67R, A68T, I93V, F110L, I115L, N122R, R138L, H157R, Y169H, H171I, H193Y, M216V, K220R, and R231K (grey) are random mutations, and N122R, R155E, Q159D, S173N, F192V, and F194Y (yellow) are monomerising mutations. The resulting TagRFP is a monomeric protein with excitation/emission peaks at 555/584 nm. [38]

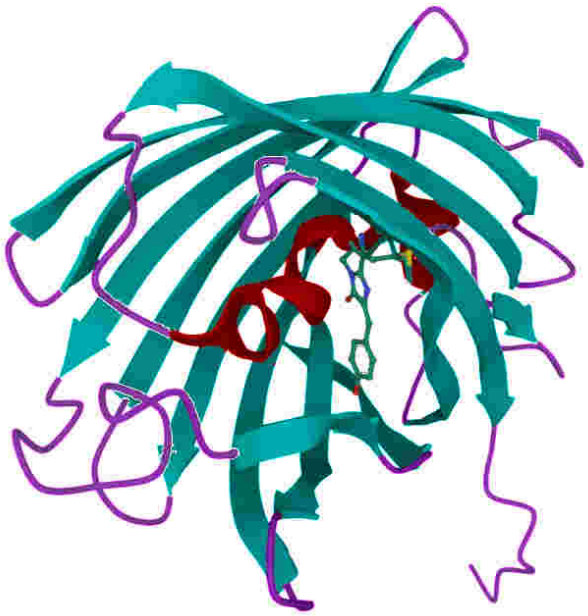

Figure 2.1. Structure of TagRFP. In blue the β-sheets, in red the α-helices, in purple the loops, and in green the chromophore. Figure adapted from the Research Collaboratory for Structural Bioinformatics Protein Data Bank.[48]

TagRFP is a monomeric protein composed of 237 amino acid residues and a molecular weight of 27 kDa. The structure of TagRFP is shown in figure 2.1 and consists of 11 β-sheets forming a β-barrel, and two α-helices. [49]

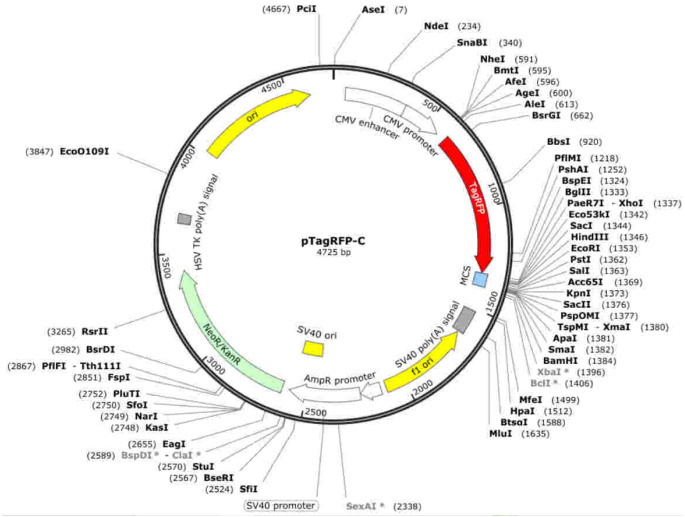

Figure 2.2. Sequence of plasmid pTagRFP-C. [50]

In this project, the TagRFP protein is encoded in the pTagRFP-C vector which sequence is shown in figure 2.2. The pTagRFP-C is a mammalian expression vector suitable to be propagated in host strains such as *Escherichia Coli DH5α*. *E. coli* is resistant to kanamycin (30 μg/mL) with a copy number $\sim$ 500. [51]

2.2 Drug Delivery

Drug delivery systems (DDS) can be described as engineered formulations or devices that allow a therapeutic agent, either drug or gene, to reach its target without interacting with other cells, organs, or tissues, therefore improving its efficiency and safety. [27], [52]

An ideal DDS should be biocompatible, protect the drug or gene from inactivation during transport to the target cells, non-immunogenic, minimal interaction with non-target cells, stable in different conditions, increase the drug bioavailability, and easy to eliminate or degrade, to name a few. [27] But the most important factor for the DDS is to be able enter the cells to allow the delivery of the drug or gene into the cytoplasm or nucleus.[27]

The internalisation of DDS by endocytosis is heavily dependent on their shape, surface charge, and size. [53]–[55] Different studies carried out by Zhao *et al.* and Chithrani *et al.* found that spherical particles had better affinity, biocompatibility, and cellular uptake than rod-like particles. [56], [57]

The surface charge of DDS affects its behaviour in the circulation system as well as the uptake mechanism. [53], [58] It has been reported that positively charged particles have higher uptake due to the strong electrostatic interaction with the cell membrane. [53], [59]–[61] Despite that, positively charged particles are cytotoxic and produce a stronger immune response than negative or neutral particles. [53], [62], [63] However, studies carried out by Chung *et al.* concluded that the uptake process depends on both, surface charge and the cell type. [64]

Nevertheless, it is the size of the DDS that plays a major in the internalisation pathway. Experiments carried out by Rejman *et al.* concluded that the size of the DDS determined the endocytosis route (see subsection 2.2.1). [65] Studies carried out by Desai *et al.* and Cai *et al.* found that the cellular uptake decreases with the increase in size as it increases the cholesterol consumption and therefore reduces the uptake efficiency. [53], [66], [67]

2.2.1 Internalisation Pathways

Endocytosis altogether with exocytosis are fundamental to maintain the cell homeostasis by exchanging material between the cell and the environment. [68], [69] Endocytosis can be described as the energy-dependent process used by cells to internalise molecules from the environment. [53], [68] Endocytosis can be divided into two different types depending on the cell type, phagocytosis only takes place in some specialised mammalian cells, and pinocytosis is performed by almost any eukaryotic cells. [53], [54], [68], [70] Additionally, pinocytosis can be divided into different internalisation mechanisms: clathrin-dependent endocytosis (clathrin-mediated endocytosis), and clathrin-independent endocytosis (caveolae-mediated endocytosis, or macropinocytosis) where the main difference between them depends on the proteins and lipids involved. [53], [54], [68], [70]

Clathrin-mediated endocytosis (CME) is the most studied mechanism, as it is present in all mammalian cells, and is responsible for the uptake of essential nutrients as well as other functions such as cell homeostasis, or intercellular communication [54], [68], [70], [71] CME involves the internalisation of the particle which is triggered by the specific interaction between the particle and membrane receptors. [54], [68] The internalisation is carried out by “coated pits” which are formed by the assembly and polymerisation of

cytosolic proteins, where clathrin, forming a trimer, is the main unit. [54], [68], [70], [71] Once the vesicle has been formed it is detached from the membrane by dynamin, a GTPase. [54], [70]–[72] CME is the dominant mechanism for the internalisation of particles smaller than 200 nm in diameter, as the size of the vesicles formed ranges between 80-200 nm. [53], [54], [65], [72], [73]

Caveolae-mediated endocytosis is a widely studied clathrin-independent carrier (CLIC) mechanism responsible for different biological functions such as cell signalling, lipid regulation, or vesicular transport. [68] This endocytic mechanism is similar to CME but it is based on the formation of lipid rafts by the assembly of caveolins, 21 kDa dimeric membrane proteins that bind to cholesterol. [54], [68], [70], [73], [74] Caveolar vesicles are flask-shaped with diameters between 50-80 nm. [54], [68], [70], [72], [74] *In vitro* caveolae-mediated endocytosis is slower than CME, with an internalisation half-time of 20 minutes, and in some cases, it can avoid lysosomes. [54], [70], [72] The avoidance of lysosomes, and therefore, hinders lysosomal degradation making the caveolae-mediated endocytosis a promising candidate for cellular delivery of proteins and DNA. [70], [75]

Particles larger than 200 nm are internalised by cells via macropinocytosis, a special clathrin- and caveolae-independent endocytosis. [70] Macropinocytosis is regulated by actin, and unlike the previously described endocytic mechanisms is not directly dependent on the cargo or its receptors. [68], [73] The interaction between the particle and membrane activates a signalling cascade, which triggers the formation of membrane protrusions that collapse and fuse with the plasma membrane. [54], [70] The vesicles formed are bigger than the ones obtained with the other endocytic mechanisms, with sizes that range from $\sim$ 500 nm up to 10 μm. [68], [70], [72], [73]

2.3 Cells

Different cells have been used in this project, *Escherichia Coli* for DNA amplification, and mammalian cells for the transfection, and this section serves to describe them.

2.3.1 *Escherichia Coli*

Escherichia coli or *E. coli* is a rod-shaped Gram-negative bacterium commonly used for recombinant protein expression. [76] It is a facultative anaerobe, producing ATP in the presence of oxygen, however, under anaerobic conditions, it can switch to fermentation. The majority of *E. coli* strains are non-pathogenic, like the strains that colonise the gut in humans and animals as part of the intestinal flora. However, some strains present pathogenic properties, most likely obtained via plasmids, transposons, or bacteriophages. [77] Even though there are many advantages of using *E. coli*, one of the most important is a generation time of only 20 minutes. Furthermore, it is easy to maintain, and has a quick and easy transformation.
The easiest cultivating setup is to introduce the *E. coli* cells into lysogeny broth (LB) medium keeping the temperature at 37$^{\text{o}}$C, which typically yields a cell density of $<1\times10^{10}$ cells/mL. [76] Many different *E. coli* strains exist all with their advantages and disadvantages. In this project, the cloning strain DH5α has been used.

The DH5α *E. coli* strain was developed in the laboratory as a cloning strain. DH5α, like other cloning strains, have the ability to accept plasmids ensuring good stability of

the inserted DNA. [78]

2.3.2 HeLa Cell Line

HeLa cells are an immortal human cell line, derived derived from cervical cancer cells, and used for scientific research. The immortality is the result of unlimited cell division associated with an active version of telomerase, which prevents the shortening of the telomeres which eventually leads to cellular death, and therefore avoiding the Hayflick limit. [79] Since the successful cloning in 1953, HeLa cells have been widely used for different research such as cancer, AIDS, gene mapping, or effects of radiation among others. [80]

2.4 Nanoemulsions

Emulsions are a type of colloid, a heterogeneous system which consists of two immiscible phases, the continuous phase, and the dispersed phase. [81]–[83] The emulsions can be divided into different types depending on their physicochemical properties as can be seen in table 2.1, mainly macroemulsions, microemulsions, and nanoemulsions.

Emulsion type	Size	Thermodynamic Stability	Kinetic Stability	PdI
Macroemulsions	1-100 μm	Metastable	Stable	>0.4%
Microemulsions	10-100 nm	Stable	Unstable	<0.1%
Nanoemulsions	<200 nm	Metastable	Stable	0.1-0.2%

Table 2.1. Classification of emulsion types depending on some physicochemical properties, where PdI is the polydispersity index. [82]

Nanoemulsions (NEs) are sub-micron emulsions, where the major differences with conventional emulsions (macroemulsions) are their size, and size distribution, with higher monodispersity. [81], [84] The smaller size of the nanoemulsions makes them transparent, as their size is smaller than the visible wavelength. [82]–[86] Furthermore, their small size provides them with higher kinetic stability against sedimentation, coalescence and fluctuation, as the Brownian motion effects dominate over the gravitational and viscosity forces which govern the induced kinetic instability. [17], [81], [82], [85], [86]. The dominating destabilisation mechanism in NEs is Ostwald ripening due to the difference in chemical potential of the droplets, but is reduced due to their lower polydispersity. [81], [84], [86]

The nanoemulsion procedure requires four components, an oil phase, an aqueous phase, emulsifier(s), and energy. The energy is required as the nanoemulsion process usually is non-spontaneous and be estimated with the equation 2.1. [82]–[87]

$$\Delta G = \Delta A\gamma - T\Delta S \tag{2.1}$$

Where ΔG is the energy required, ΔA is the increase in the interfacial area, γ is the surface tension, and TΔS is the dispersion entropy at an absolute temperature T.

The emulsifiers, which can be polymers (proteins, peptides, or polysaccharides), or surfactants (usually anionic or zwitterionic), are critical in the nanoemulsion formation as

they reduce the surface tension (γ) between the oil and water phases and are adsorbed in the oil/water interface and stabilise the NEs sterically, electrostatically or a combination of both. [82], [84], [85] The reduction of γ results in a reduction of the Laplace pressure (ΔP) following the equation 2.2, where r is the droplet radius. [85], [88]

$$\Delta P = 2\gamma/r \tag{2.2}$$

The Laplace pressure (ΔP) is proportional to the Weber number (W_e), a dimensionless number used in fluidic mechanics to describe droplet distortion. W_e measure the ratio between the inertia and interfacial tension (ΔP from equation 2.2) as shown in equation 2.3. [85], [89]

$$W_e = \frac{G\eta_d r}{2\gamma} \tag{2.3}$$

Where G is the velocity gradient, η_d is the dispersed phase velocity, r is the droplet radius, and γ is the surface tension. Therefore, for a given r, a reduction in γ results in higher values of W_e, which indicate greater droplet deformations, which means that smaller droplets are obtained with the same energy. [85]

2.4.1 Electrospray

Electrospray (ES) is a soft ionisation technique discovered in the late 80s that uses a high voltage to dissipate a liquid sample into an aerosol-generating highly charged droplets. [90], [91] This technique is widely used for both chemical and biochemical analysis such as mass spectrometry (MS). [91] The liquid is dispensed through an emitter connected to a power supply. When a difference of potential is applied the liquid forms a Taylor cone, a jet with a equipotential surface generating particles at the top of the cone which are radially dispersed. The generation of droplets occurs when the electrostatic force is greater than the surface tension. [90] The diameter of the droplets depends on different parameters such as the potential applied and the flow rate. [90] However, high voltages could also result in an unstable Taylor cone. Nowadays ES has several applications like MS, electrospinning to create thin fibres, to deposit single particles on surfaces, or the fabrication of drug carriers. [92]–[94] The use of ES for drug delivery is as a consequence of the sub-micrometre-sized particles with higher surface area. This higher surface area increases the dissolution rates of the drugs as well as their bioavailability. Furthermore, reducing the dosage used and the associated side effects side effects. [95] Polymeric DDS generated with ES have already been used in the medical field for immunotherapy and delivery of nucleic acids. [96], [97]

2.4.2 High-Speed Stirring

One of the techniques that will be used in this project to obtain the nanoemulsions is high-speed stirring, a high energy method that depends on mechanical devices to generate high disruptive forces to reduce the size of the droplets. [17], [82], [85], [98] High energy methods consist of three consecutive steps. The first step consists in preparing a macroemulsion by mixing the oily and aqueous phase, with emulsifiers. The second step consists of the deformation and disruption into smaller drops. Last, is the adsorption of the emulsifier/surfactant on the water/oil interface stabilising the drops. [18], [99], [100]

High-speed stirring of the disruptive forces required to generate smaller droplets is achieved by a rotor-stator homogeniser. [81] A rotor-stator homogeniser is formed by a fast-spinning inner rotor, and a perforated stator, as stationary outer sheath. [100], [101] The fluid enters the rotor accelerating the fluid. The blades of the rotor redirect the fluid through the stator slits. [100] In high-speed stirring the driving force is hydrodynamic shear. [100], [102] The shear forces are generated by the high-velocity gradient in the gap between rotor and stator. This gradient is a consequence of the velocity difference between the fluid close to the rotor, and the fluid close to the stator, which is stationary. [103]

One of the factors that affect the droplet size are the applied shear forces. [99] The applied shear forces can be described by Taylor's equation (equation 2.4) which assumes that the dispersed phase viscosity (η_d) is negligible compared to the continuous phase viscosity (η_c), so $\eta_c >> \eta_d$. [17]

$$r \sim \frac{\gamma}{\eta_c \sigma} \tag{2.4}$$

Where r is the radius achieved, σ is the applied shear rate, and γ is the interfacial tension. The shear forces deform the interface of the droplet, then, due to the interfacial tension a capillary instability is generated which results in the break of the droplet into smaller ones. [17] To form nanoemulsions with a mean size of 100 nm the shear rates required are in the range of 10^8 s^{-1}. [81], [99], [104]

2.4.3 Microfluidics

Microfluidics emerged in the beginning of the 80s along with the development of microsystems after the success in the field of miniaturisation. [105], [106] Microfluidics can be defined as the processing and manipulation of flows circulating in a microsystem. The typical dimensions of this microdevices range from 10-500 micrometres (μm), and can manipulate small volumes of fluids 10^{-9}-10^{-12} litres. [105], [107] Additionally, the small dimensions of the microfluidic devices allow the manipulation of smaller volumes and energy, and thereby, reduced costs. [107], [108]

The reduced dimensions of the system due to miniaturisation disrupt the equilibrium of forces that dominate in the macroscopic scale and therefore affecting the physical behaviour of the fluid. [106] In microfluidics, the surface effects dominate over volumetric effects as a consequence of the high surface-to-volume ratio (κ). [107], [109]

$$\kappa = \frac{\text{surface area}}{\text{system volume}} \sim \frac{l^2}{l^3} = l^{-1} \tag{2.5}$$

From equation 2.5 we see that $\kappa \to \infty$ when $l \to 0$, where l is the system's length. This implies that surface-related forces are dominant when reducing the size. [107] This different behaviour can be described using dimensionless numbers, which reduce the number of variables into unified parameters to correlate physical phenomena. [110] These unified parameters come from the incompressible Navier-Stokes equations of continuum and momentum for Newtonian fluids, equation 2.6 and equation 2.7 respectively. Both equations present a linear proportionality between viscous stresses and the strain rate. [89], [108], [111]

$$\frac{\partial \rho}{\partial t} + \nabla \cdot (\rho \mathbf{u}) = 0 \tag{2.6}$$

$$\rho\frac{\partial \mathbf{u}}{\partial t} + \rho(\mathbf{u}\cdot\nabla)\mathbf{u} = -\nabla p + \mu\nabla^2\mathbf{u} + \rho\mathbf{g} \tag{2.7}$$

Where ρ is the density, t is the time, $\boldsymbol{u}$ is the velocity field, p is the static pressure, μ is the fluid viscosity, and $\boldsymbol{g}$ is the gravitational acceleration. Droplet generation by emulsion is achieved by mixing two phases, and since the momentum equation only considers a single-phase system an additional term is introduced. This term treats the interface between both phases as a boundary, adding an interfacial stress ($\boldsymbol{F}_S$), modifying equation 2.7 as: [89], [108]

$$\rho\frac{\partial \mathbf{u}}{\partial t} + \rho(\mathbf{u}\cdot\nabla)\mathbf{u} = -\nabla p + \mu\nabla^2\mathbf{u} - \mathbf{F}_S + \rho\mathbf{g} \tag{2.8}$$

As can be seen in equation 2.8, since the interfacial stress is a force, the term $\mathbf{F}_S$ is added to the right side of the equation, while the left side represents the acceleration. [89], [108] Furthermore, many microfluidic systems usually use low fluid flow velocities (up to 1 cm/s), and therefore incompressible flows can be considered. Assuming incompressible flows simplifies equation 2.6 as follows: [89]

$$\nabla\cdot\mathbf{u} = 0$$

Reynolds number (Re) is a dimensionless number widely used to judge if the flow is laminar (low Re) or turbulent (high Re) by comparing inertial (f_i) to viscous forces (f_v). [89]

$$Re = \frac{f_i}{f_v} \sim \frac{\rho u^2}{\mu u/L} = \frac{\rho u L}{\mu}$$

However, due to the small dimensions of the microfluidic systems (L), Re is low which indicates that the viscous forces dominate, resulting in a laminar flow. [89]

The capillary number (Ca) is the most important dimensionless number in droplet generation as it compares the viscous force (f_v) to capillary pressure (f_γ). The capillary pressure takes into account the surface tension, which plays a major role in droplet generation. [89]

$$Ca = \frac{f_v}{f_\gamma} \sim \frac{\rho u^2}{\gamma/L} = \frac{\mu u}{\gamma}$$

As can be seen in the equations above, the viscous force (f_v) and capillary pressure (f_γ) are inversely proportional to the characteristic length (L), which are enhanced with the reduced dimensions and dominate over inertial force (f_i), and gravitational forces ($f_g \sim \rho g L$). [89]

The last dimensionless number with importance for droplet generation is the flow rate ratio (R_f). R_f is the ratio between the flow rates of the dispersed and continuous phases, Q_d and Q_c respectively. [89], [108], [112]

$$R_f = \frac{Q_d}{Q_c}$$

Passive droplet generation is a consequence of the fluid instabilities caused by the competing stresses between surface tension and viscous stress, by trying to reduce the surface area of the interface, and by extending and dragging the droplet respectively. [108], [113] There are five breakup modes squeezing, dripping, jetting, tip-streaming, and tip-multi-breaking, where the most common are the first three. [108], [113] Both Ca and R_f have an important role in the different regimes. [112]

The squeezing break-up mode usually happens at low values of Ca (10^{-2}), and is due to the Rayleigh–Plateau instability. In this regime, the shear stresses exerted on the drop interface are not sufficient to distort the drop. As a consequence, there is a build-up pressure due to the blockage of the cross-section of the channel due to the growth of the droplet. This increase in pressure leads to the squeezing of the droplet of the neck of the liquid thread. [108], [112]–[114] In the dripping regime the shear forces applied to the droplet interface are bigger which results in the detachment of the droplets before filling the channel. Dripping occurs at a small Ca range ($\sim$ 0.1-0.2). [112] Jetting break-up mode is observed at high values of Ca. In this regime, both phases flow parallel to each other creating a jet before a droplet is formed downstream of the channel. [112], [115] In figure 2.3 the different breakup modes are shown.

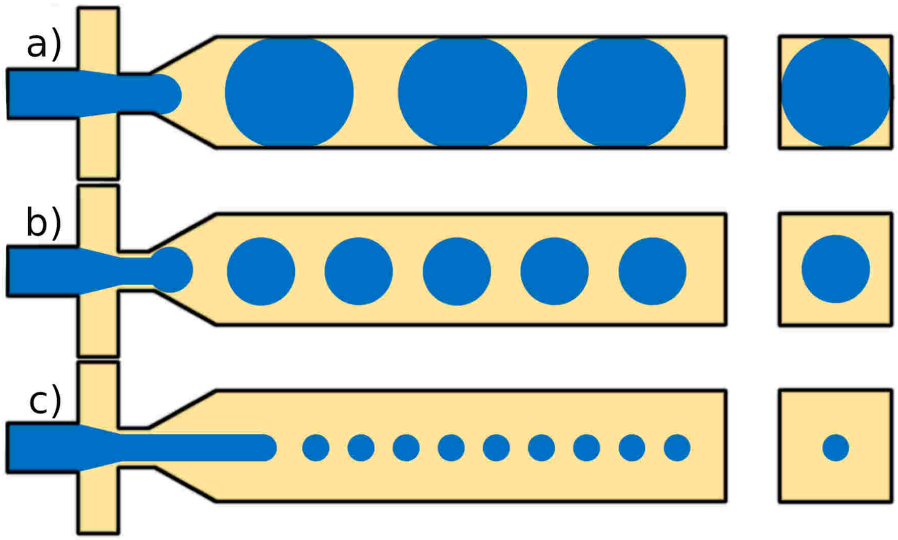

Figure 2.3. On the left, droplet formation for the three dominating regimes where **a)** is the squeezing regime, **b)** the dripping regime, and **c)** the jetting regime.. On the right cross-section of the channel for each breakup regime. The continuous phase is represented in yellow, and the dispersed phase is in blue.

Another important factor for droplet generation is the geometry of the microfluidic device providing a boundary of the microflow. [108], [112] Depending on their geometry the microfluidic devices can be classified as cross-flow, co-flow, or flow-focusing as can be seen in figure 2.4.

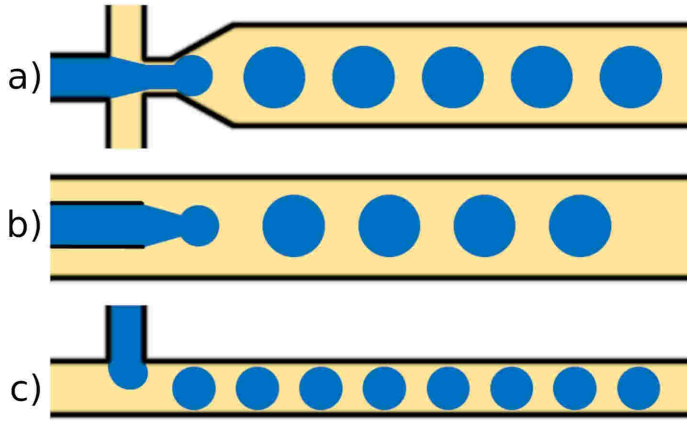

Figure 2.4. The three main techniques for droplet generation, where **a)** is flow-focusing, **b)** co-flow, and **c)** cross-flow. The continuous phase is represented in yellow, and the dispersed phase is in blue.

In the flow-focusing geometry hydrodynamic focusing of the two immiscible fluids is used to create the droplets, shown in figure 2.4 **a)**. [108] In the cross-flow geometry, the continuous and dispersed phases are parallel to each other (θ=180º) as can be seen in figure 2.4 **b)**. [108], [116] Last, in the cross-flow geometry the two immiscible fluids meet at an angle θ (between 0º-180º). However, the most common geometry is the T-junction, represented in figure 2.4 **c)**, where the two phases meet orthogonally. [108], [116]

2.5 Droplet Generation

This section serves to describe different polymers used to generate the nanoemulsions throughout the project. Gene encapsulation is commonly done using microgels as biomaterials. Microgels are colloidal particles formed by a three-dimensional network of cross-linked polymer chains in the nanometric range (5-500 nm). [117]–[119]

2.5.1 Alginate

Alginate is a natural anionic polysaccharide synthesised by bacteria such as *Pseudomonas aeruginosa* or *Azobacter* but is typically extracted from brown seaweed or algae. [120]–[122] Alginate is a linear block copolymer formed by (1→4)-linked β-D-mannuroic acid (M block) and α-L-guluronic acid (G block). Both blocks have a six-membered ring structure ($C_6H_8O_6$) and are linked together covalently. Typically, calcium ions (Ca^{2+}) are used as a cationic cross-linker due to their high affinity with alginate and due to their biocompatibility. [123] In this project, the Ca^{2+} ions are contained in the oil phase (continuous phase) and will be externally introduced, by dripping the alginate solution (dispersed phase) into the continuous phase. This, will create an external gelation due to the Ca^{2+} gradient, which is described by Fick's law of diffusion (equation 2.9). [124]

$$\mathbf{J} = -D \cdot \nabla c \tag{2.9}$$

Where $\mathbf{J}$ is the diffusive flux, D is the diffusion coefficient, and ∇c is the concentration gradient vector. A negative sign is included in Fick's law as the diffusion occurs from high to low concentration areas.

The initial cross-linking on the droplet surface creates a semi-solid membrane surrounding the aqueous core modifying the initial Ca^{2+} gradient, as semi-solids have lower diffusion ratios than liquids. This will affect the concentration of alginate, creating a non-homogeneous droplet. [125]

2.6 Microfluidic Chip

This section will serve to describe the design of the microfluidic chip as well as the manufacturing techniques. The goal of the chip is to be capable of performing continuous gene encapsulation into oil/water nanoemulsions. Hence the chip has to contain an oil and water reservoir, a droplet generator junction, and a droplet collector. A schematic representation of the microfluidic chip set up is shown in figure 2.5.

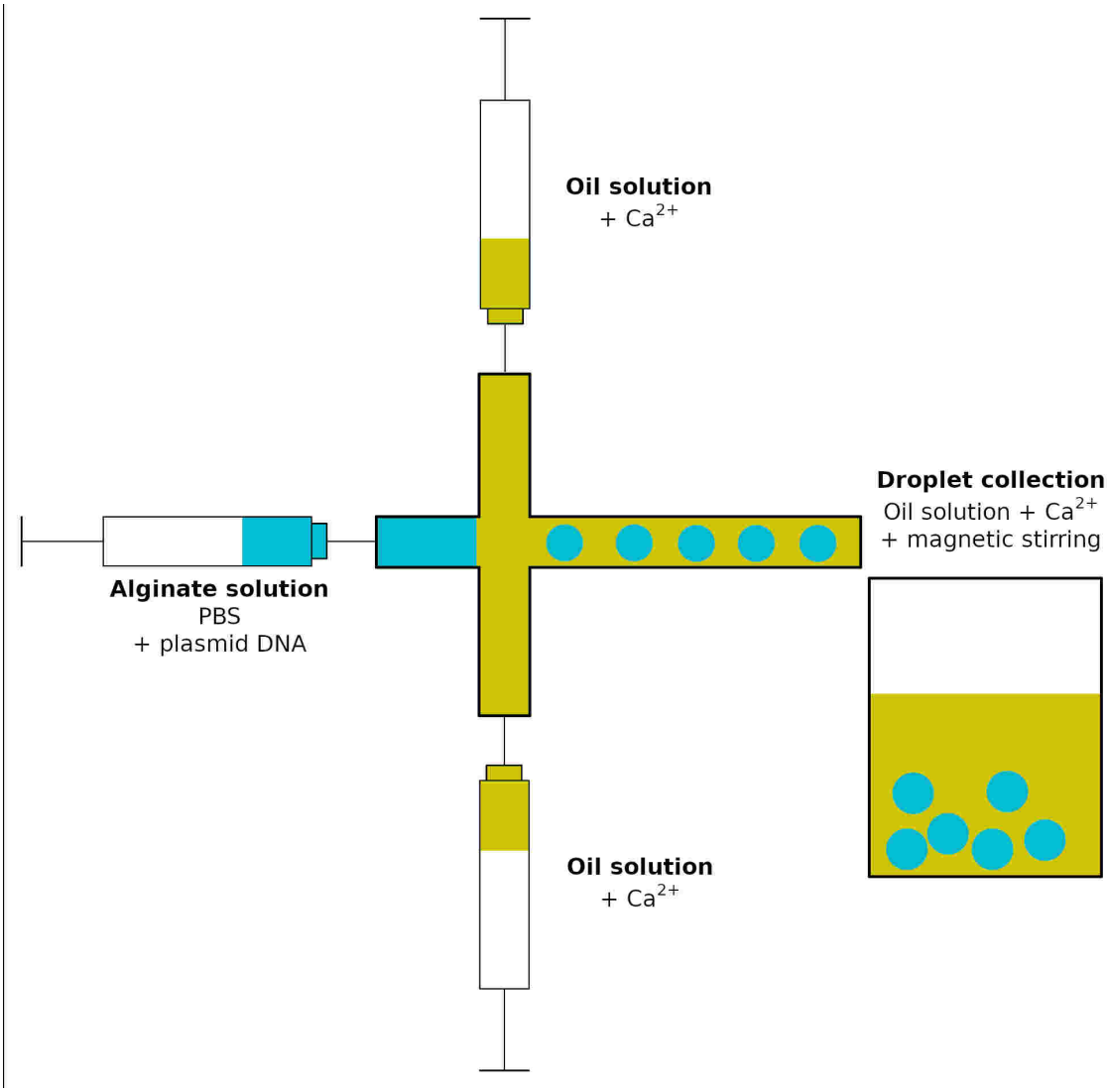

Figure 2.5. Caption

Three different channel heights will be tested. Smaller channel heights 50 μm, and 100 μm were manufactured by soft lithography and cast in SU-8 photoresist. The 400 μm channel was manufactured by 3D-printing using a standard clear UV resin. The inlets consist of

syringes that are connected to a pump where the flow rate Q is adjusted. The droplets are collected from the outlet in a beaker which contains an oil solution with Ca^{2+} ions under magnetic stirring. The droplet collection is carried out to ensure the external gelation of the droplets.

2.7 3D-Printing

Three-dimensional printing, or 3D-printing, is a form of additive manufacturing which consists of the manufacturing of a 3D object layer by layer either from a computer-aided design (CAD) model, or a digital 3D model. [126]–[128] Even though the first robotic 3D printer was developed in 1984 by Charles W. Hull, and later commercialised in 1989. In the 2010 gained popularity as low-cost 3D printers became available. [126], [129] Nowadays, 3D-printing is used in many different industries such as aerospace, automotive, electronic, food, or healthcare among others. [130]–[136] The 3D-printing process consists of three main steps: modelling, printing, and postprocessing.

2.8 Photolithography

Photolithography is a patterning technique that uses light to transfer the patterns from a mask to a photosensitive resin. [137]–[139] This technique has been widely used in the past 30 years due to its easiness, and reproducibility of the desired structures. [137] Nonetheless, one of the limits of photolithography is the wavelength used to irradiate the photoresin with a resolution up to 100 nm that can be reduced to 50 nm when deep ultraviolet light is used. [137], [140] The photolithography process is the following: first, the photoresist is added over a silicon substrate and spin-coated to evenly coat the substrate surface. Then a soft-bake is carried out, typically at 95ºC, to remove the excess of solvent and improve the adhesion between resin and substrate. After the soft baking, the coated substrate is aligned with a photomask and irradiated typically with UV light (∼350 nm). Last, there is the development process where the photoresin that is not cross-linked is removed by a chemical developer. [139] The final pattern after the development process depends if the resin used is positive or negative. In a positive photoresin the unexposed resin is not soluble with the developer and will remain on the substrate. A negative photoresin is the other way, the exposed resin remains on the substrate while the unexposed resin is dissolved. [139]

The SU-8 resist is an epoxy-based, acid-catalysed and chemically amplified negative photoresist. [141]–[143] SU-8 is widely used for the fabrication of micro-electro-mechanical systems (MEMS) due to its high chemical, thermal (degradation temperature $\sim 380^{\circ}$ C), and mechanical stability ($E \sim 4 - 5$ GPa). [141], [142] Furthermore, the layer's thickness can be adjusted depending on the SU-8 formulation viscosity. [142]

SU-8 photolithography is divided into five processing steps: deposition, soft bake, exposure, post-exposure treatment, and development. First, the resin is deposited onto a substrate, commonly by spin-coating. Then, the substrate is soft baked, usually at 95ºC, to remove the casting solvent and improve the adhesion between resin and substrate. After the soft baking, the coated substrate is aligned with a photomask and irradiated typically with UV light (∼350 nm). In the exposed areas hexafluoroantimonic acid is formed protonating the epoxy groups. The protonated oxonium ions react with neutral epoxides which end

up in the cross-linking of the resin, which renders it chemically inert. After irradiation, a post-exposure bake is performed to increase the cross-linking, and fully polymerise the resin. The last step is the developing and cleaning, where the unpolymerised SU-8 is removed by submerging the substrate in the developer, followed by a rinsing, and drying steps. [141], [142]

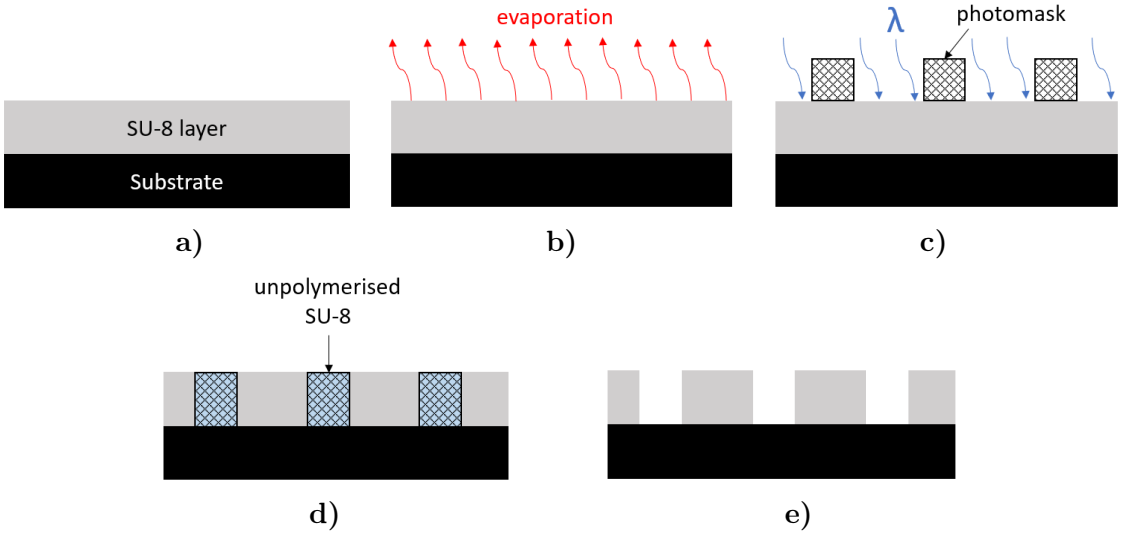

Figure 2.6. Schematic representation of SU-8 photolithography processing steps. **a)** deposition step, **b)** soft-bake step, **c)** exposure step, **d)** post-exposure treatment, and **e)** developing step.

The photolithography processing steps for SU-8 resin are shown in figure 2.6. For the microchips to work, the geometries cast in SU-8 resin are covered in polydimethylsiloxane (PDMS) to close the circuit.

2.9 Characterisation Techniques

This section will serve to describe the different characterisation techniques used throughout the project. This chapter has been divided into two, the techniques used to characterise the droplets, and the techniques used to evaluate the transfection efficiency.

Characterisation of Droplets

In this part of the section are described the different techniques used to characterise the nanoemulsions.

2.9.1 Nanoparticle Tracking Analysis

Nanoparticle tracking analysis (NTA) is a real-time characterisation technique of nanoparticles in solution. NTA uses both, light scattering and Brownian motion of the nanoparticles. Each particle is analysed and visualised separately, allowing an estimation of the particle size distribution and particle concentration using a direct frequency distribution. The principle of operation of the NTA is a high-intensity laser beam combined with a low-background optical configuration, which allows the visualisation of the nanoparticles in suspension associated with the refractive index (RI). [144] For particles with high RI, typically inorganic nanoparticles such as gold sizes up to 15 nm can be resolved, however, nanoparticles with low RI, polymeric nanoparticles, have a minimum resolution up to 30 nm. [144] Yet the minimum resolution of the NTA for biological nanoparticles is 10 times higher than flow cytometers. [144]

2.9.2 Scanning Electron Microscope

The scanning electron microscope (SEM) is an electron microscopy technique that even though its development started in the late 20s, the first commercial SEM was not marketed until 1965 by the Cambridge Instrument Company. [145] Even though that SEM has the same working principle as an optical microscope the major difference is the source used to obtain the images, while an optical microscope uses light as a source SEM uses a beam of electrons. [146] When the electrons hit the sample they produce different signals (i.e., electrons, X-rays) that give information about topology, morphology, or composition to name a few. [146] An SEM contains an electron beam to emit the electrons, typically with a tungsten cathode, however other materials are also used such as lanthanum hexaboride (LaB_6) or field emission guns. The electron beam is generated by applying a high voltage to the cathode, and usually has energy ranging from 0.2-40 keV. The electron beam is focused by condensers, and passes through an electron column, and finally through a lens which deflects the beam allowing the scan of the sample in the xy-plane. [145], [147] One of the advantages of SEM is the higher resolution up to 3Å compared to the 200-300 nm of optical microscopes. However, some major drawbacks of SEM are that the samples must be dry as a high vacuum is required, and conductive to prevent the accumulation of electrostatic charge. To analyse non-conductive samples (i.e., biological) the samples are coated with conductive materials typically Au but also Au/Pd, Pt or Ir. [148]

Evaluation of Transfection

This part of the section serves to describe the techniques used to evaluate the transfection efficiency by localising the fluorescent proteins encoded in the genes by fluorescence measurements.

Fluorescence can be described as the emission of light after the absorption of light. [149]–[151] Fluorescence takes place when the electrons return to the ground state (S_0) after their excitation to the excited states (S_1, S_2, or S_n) releasing the excess of energy as photons. [149]–[151] The fluorescence process can be observed in figure 2.7 below.

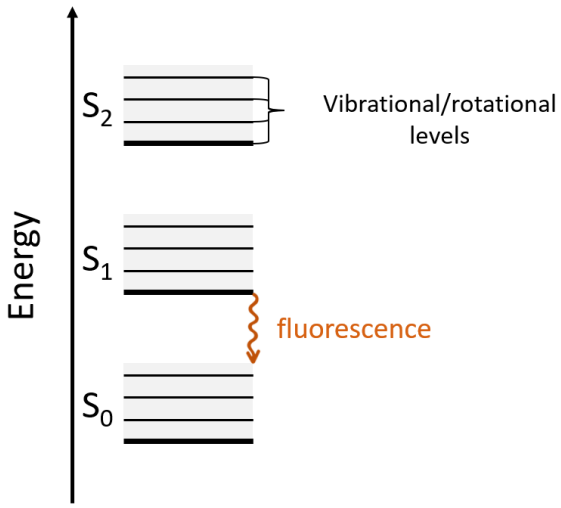

Figure 2.7. Jablonski diagram showing different energy states (S_0, S_1, and S_2) of a molecule as well as the different electronic transitions during excitation and emission. [149], [150]

To produce fluorescence, the minimum energy required is the one that can promote the transition of an electron to the first excited state (S_1). This energy is inversely related to the photon wavelength as can be seen in equation 2.10, where h is Planck's constant, and c and λ are the speed and wavelength of light in a vacuum respectively. [150], [152]

$$E = h \times c/\lambda \tag{2.10}$$

The electronic excitation usually has a bigger energy than the energy needed for the transition from the ground state to an excited state. This excess of energy is later discarded through vibrational relaxation or internal conversion. As a result, the emission energy is smaller than the excitation energy, provoking an increase of the emission wavelength, known as the Stokes shift. [149], [150], [152]
The Stokes shift varies from one fluorophore to another and ranges from 50 to 200 nm. The greater the shift is, the easier to separate the exciting and emitted light. [150], [152], [153]

Even though there are some organic substances with intrinsic fluorescence, synthesised compounds are usually used. These synthesised compounds usually present conjugated double bonds and ring structures, with pi-bonds that allow the distribution of the electrons over large areas. [149], [150] The more conjugated bonds result in lower excitation energy

and a longer wavelength, which allows deeper penetration into tissues as it scatters less, and lower cell damage. [151]

Different parameters to take into account in a fluorophore are the fluorescence quantum yield, the molar extinction coefficient, quenching, and photobleaching. The fluorescence quantum yield or quantum efficiency (QE) equation 2.11 is the measure of the total light emission over the entire fluorescence spectral range. [149], [150]

$$QE = \frac{\#\text{ emitted photons}}{\#\text{ absorbed photons}} \tag{2.11}$$

On the other hand, the molar extinction coefficient (ε) is the probability of the fluorophore of absorbing a photon at a certain λ- The extinction coefficient follows the Lambert-Beer law (equation 2.12) and has units of $M^{-1}cm^{-1}$. [149], [150]

$$A = \varepsilon cl \tag{2.12}$$

Where A is the absorbance, ε is the molar extinction coefficient, c is the concentration, and l is the optical path (in cm).

2.9.3 Fluorescence Microscopy

Fluorescence microscopy (FM) is a characterisation technique similar to optical microscopy which is based on the detection of fluorescence. [150], [154] The sample is illuminated with a specific near-monochromatic light exciting the fluorophore, which emits light with a longer wavelength. The detected light is filtered to separate the desired wavelength from the surrounding radiation. [154] FM is widely used in biology and biomedical fields as fluorescence labelling is highly specific and therefore allows the study of the dynamics of proteins or DNA. [152], [155]

The typical set-up of the fluorescent microscope is epi-illumination, where the objective is used for imaging, magnifying, and as a condenser. The main advantage of this set-up is that only the small percentage of the exciting light that is reflected off the sample needs to be blocked. However, the main disadvantage is that the exciting and fluorescent lights overlap and have to be separated. [150]

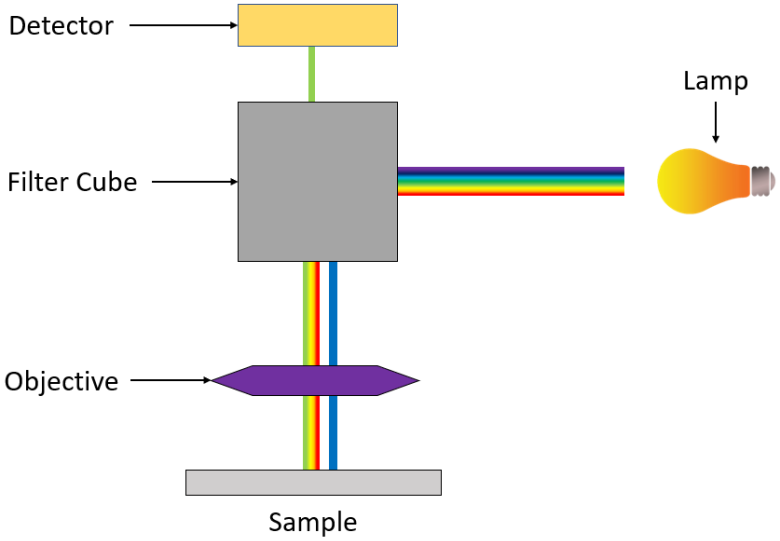

Figure 2.8. Scheme of epi-illumunation set-up in fluorescent microscope.

A fluorescent microscope using epi-illumination has the following components: light source, filter cubes, objective, and the detector, as can be seen in figure 2.8. The typical light sources used in FM are xenon or mercury arc lamps, but nowadays lasers and high-power LEDs are also used. Xenon lamps have an even coverage from UV to near-IR, while mercury lamps present intense peaks at 365, 405, 436, 546, and 579 nm. [149], [150]

The filter cubes are composed of excitation and emission filters, and a dichroic mirror, as shown in figure 2.9. The excitation filter are used to select a specific excitation wavelength to illuminate the sample by absorbing other wavelengths. Similar, emission filters only allow a specific wavelength to pass to the detector by blocking both the reflected exciting wavelength as well as other emitting wavelengths. [154], [156] The dichroic mirror is a type of filter that serves to split the excitation from the emitting light, and is usually set up at a 45° angle with respect to the light source. The dichroic mirror's principle is the reflection of high-energy wavelengths towards the sample and transmission of lower-energy wavelengths towards the detector. [151], [154]

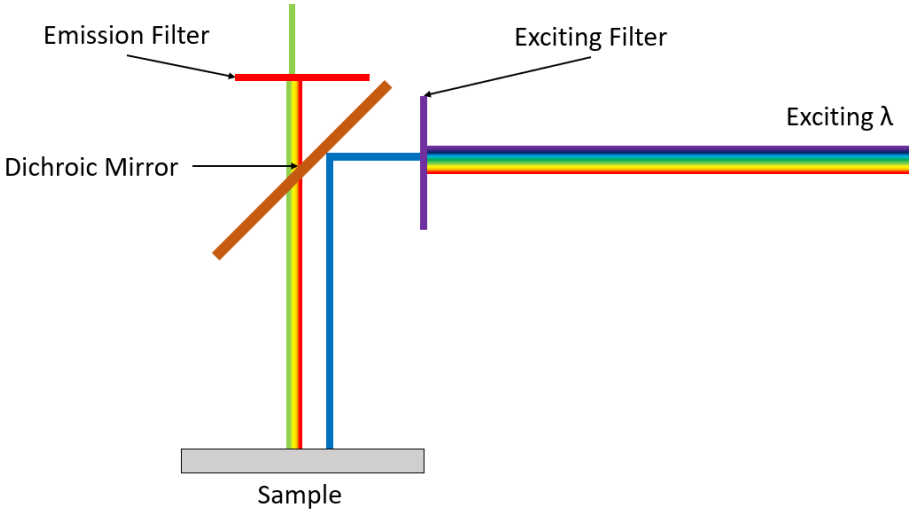

Figure 2.9. Schematic representation of the filter cube. The components of the filter cube being the exciting filter, emission filter, and dichroic mirror are represented in purple, red, and brown respectively.

The objective is the most important part of the FM as it is used to condense the exciting light, magnify, and create the image. [149] An ideal objective would have a large numerical aperture (NA), few lens elements, and will pass exciting wavelengths of UV, visible, and near-IR. Large NA would increase both, the observed intensity which is proportional to $(NA)^4$, and the resolving power; however, a large NA would reduce the image contrast. [150], [151] Fewer lenses would reduce the light loss caused by the reflection. [150]

$$\varepsilon = 0.61\frac{\lambda}{NA} \tag{2.13}$$

The resolving power would increase with large NA as the resolving distance would decrease following equation 2.13. Where ε is the resolving distance, and λ is the exciting wavelength both in nanometers.

The most commonly used detectors in FM are cooled charge-coupled device (CCD) camera systems. [157], [158] A CCD is an integrated system formed by an array (usually 2D) of pixels represented by p-doped metal–oxide–semiconductor (MOS) capacitors. The emission photons generate photoelectrons when they hit the surface of the capacitors. Then, the photoelectrons are moved throughout the array and at the end, the charge created by the photoelectrons is amplified and converted into a voltage. [159], [160] Each exposure produces a different charge distribution pattern on the CCD array, which is converted by the CCD system creating an image with proportional intensity distribution. [160]

Chapter 3

Methods

The focus of this chapter is to list the materials used throughout the project and to describe the experimental procedures carried out as well as the software used.

3.1 Software

This section serves to describe the different software used throughout the project. The specifications of the computer used are shown in table 3.1.

ASUS UX310UA
Intel(R) Core(TM) i5-6200U CPU 2.30 GHz 2.40 GHz
8 GB RAM
64-bit operating system, x64 based processor
Windows 10

Table 3.1. Specifications of the computer used to perform the simulations.

The software used will be described in their respective section.

3.1.1 AutoCAD

Developed and marketed by Autodesk Inc., AutoCAD ® is a computer-aided design (CAD) and drafting software application, allowing the creation of 2D and 3D geometries. The newest version of AutoCAD ® includes industry-specific toolsets, features and libraries. [161] Furthermore, AutoCAD ® geometries with file extension .dxf can be imported into simulation software such as COMSOL ® Multiphysics.

3.1.2 COMSOL Multiphysics

The droplet generator of the microfluidic chips used throughout the project was simulated using COMSOL Multiphysics® version 5.6 a cross-platform finite element analysis, solver and multiphysics simulation software. COMSOL Multiphysics® allows conventional physics-based user interfaces and coupled systems of partial differential equations (PDEs). The simulations carried out in the project were performed using the PARDISO linear system solver, the time-dependent solver, and the generalised alpha stepping method with

manual time steps set to 6.5×10^{-5}. The remaining solver settings were kept default and all meshing was user-controlled.

3.1.3 ImageJ

ImageJ is an image processing program, inspired by its predecessor NIH Image, developed in 1997 by the National Institutes of Health (NIH) and the University of Wisconsin. [162], [163] ImageJ is based on Java programming language with an open architecture which can be expanded via macros, scripts or plugins. [162]–[164]

ImageJ can display, edit, analyse, process, save, and print images (8, 16, and 32-bit). Additionally, ImageJ fixed one of the main problems of other image-processing programs by supporting different image file formats, such as TIFF, PNG, GIF, JPEG, or BMP, as well as stacks and hyperstacks, which are multiple images that are spatially or temporally related, in a single window [162], [163]

3.1.4 LayoutEditor

Developed in 2004, LayoutEditor is an editor for layout designs and schematics used in different areas such as micro- and nanoelectronics, integrated circuits, or micro-electromechanical systems (MEMS). LayoutEditor has a user-friendly interface that can be adjusted. As a default it works with the GDSII file format, however, it also works with other formats such as OASIS, OpenAccess, CIF, SVG, CSV, PNG, JPG, or ODB++ to name a few. Furthermore, it has a built-in scripting interface which allows the recording of macros. [165]–[167]

3.1.5 OriginPro

All graphs were edited using OriginPro® version 8.5, a data analysis and graphing software with an intuitive user interface. Furthermore, Origin supports customised analysis as well as graphing tools, and templates to name a few, also allowing a technical scientific programming environment for C and Python.

3.2 Microfluidic Droplet Generation

This section serves to describe the geometry and the physics governing the droplet generation in COMSOL Multiphysics ® as well as the experimental procedures carried out in the laboratory.

3.2.1 Simulations

For the simulations, the level set and phase field interfaces from the two-phase flow module were used. Both interfaces are coupled with the laminar flow interface.

The Navier-Stokes equations govern fluid flow and solve for the fluid velocity and the pressure fields. Concerning the modelling, the equations are solved within each of the domains. However, immiscible fluids present a problem regarding their fluid properties. This problem arises due to the drastic variation of both viscosity and density change across the interface between fluids, compared to other fluid systems where they are either constant or vary smoothly. Hence, surface tension effects and the contact angles at wetted walls must be considered.

Laminar Flow

The laminar flow interface computes pressure and velocity fields for single-phase fluid flows in a laminar flow regime. The laminar flow regime is applicable for low Reynolds (Re) number before turning into turbulent flow. The critical Reynolds number is dependent on the geometry, which for pipe flow case $Re_{crit} \sim 2000$. [168] The Laminar Flow interface solves the Navier-Stokes equations for conservation of momentum (equation 3.1) and the conservation of mass (equation 3.2). Furthermore, it supports non-Newtonian fluids as well as different flows.

The laminar flow interface allows stationary and time-dependent analysis. Fluid properties, wall, and initial values nodes are also added to the interface. The boundary conditions are described by the wall node and are set to no-slip by default. [168]

Level Set

The Level Set interface solves the problems where the computational domain can be split into two separate domains, by representing moving boundaries or interfaces using a fixed mesh. The equations solved are the incompressible Navier-Stokes equations, and are solved for each finite element in the mesh. [168]

ρ	Density
$\mathbf{u}$	Velocity field
p	Fluidic pressure
$\mathbf{I}$	Identity matrix
$\mathbf{F}_{st}$	Surface tension force

$$\rho\frac{\partial \mathbf{u}}{\partial t} + \rho(\mathbf{u}\cdot\nabla)\mathbf{u} = \nabla\cdot[-p\mathbf{I} + \mu(\nabla\mathbf{u} + \nabla\mathbf{u}^T)] + \mathbf{F}_{st} \quad (3.1)$$

$$\nabla\cdot\mathbf{u} = 0 \quad (3.2)$$

In COMSOL, the level set function (ϕ) is a smooth step function. In one domain $\phi = 0$, and $\phi = 1$ in the other domain. In these simulations when $\phi < 0.5$ corresponds to the dispersed phase while $0.5 < \phi$ corresponds to the continuous phase. On the other hand, the interface between immiscible fluids is defined as the 0.5 isocontour, i.e. the level set. The interface moves along with the velocity field u, and is calculated by solving the transport equation (equation 3.3) for the level set function. [168]

γ Reinitialisation parameter
ε Interface thickness parameter

$$\frac{\partial \phi}{\partial t} + \nabla(\mathbf{u}\phi) = \gamma \nabla \cdot \left(\varepsilon \nabla \phi - \phi(1-\phi)\frac{\nabla \phi}{|\nabla \phi|} \right) \tag{3.3}$$

The left-hand side of the equation makes sure of the interface's correct motion while the right-hand side provides numerical stability. The interface thickness parameter (ε) is the thickness where ϕ goes smoothly from $0 \rightarrow 1$. By default ε is constant and and equals the largest value of the mesh size. The reinitialisation parameter (γ) determines the stabilisation or amount of reinitialisation of the level set function, and to keep the gradients in the level set function focused on the interface of the fluids. If γ is too high the interface will either move incorrectly, if γ is too low the interface will not remain constant due to numerical instabilities. By default γ is 1 m/s, however, it is recommended to set the value of γ as the maximum magnitude of the velocity field $\mathbf{u}$. [168]

The level set function is also integrated into the density and viscosity of the two immiscible fluids as shown in equation 3.4 and equation 3.5 respectively.

ρ_c Continuous-phase density
μ_c Continuous-phase viscosity
ρ_d Dispersed-phase density
μ_d Dispersed-phase viscosity

$$\rho = \rho_c + (\rho_d - \rho_c)\phi \tag{3.4}$$

$$\mu = \mu_c + (\mu_d - \mu_c)\phi \tag{3.5}$$

The laminar flow interface is automatically applied once the level set interface is chosen. The interfaces, and the physics are correlated by a multiphysics module. The multiphysics module adds a wetted-wall boundary condition, which makes sure that the interface can move along the walls when the wall is in contact with a fluid-fluid interface. The laminar flow satisfies the non-penetration condition, and a wall-force ($\mathbf{F}_w$), shown in equation 3.6 and equation 3.7 respectively.

$\mathbf{F}_\theta$ Boundary force
θ_w Contact angle
δ Dirac δ function
$\mathbf{F}_{fr}$ Frictional force
$\mathbf{n}_{int}$ Interface's normal vector
β Slip length
σ Surface tension
$\mathbf{u}$ Velocity field
μ Viscosity
$\mathbf{n}_{wall}$ Wall's normal vector

$$\mathbf{u} \cdot \mathbf{n}_{wall} = 0 \tag{3.6}$$

$$\mathbf{F}_w = \mathbf{F}_\theta + \mathbf{F}_{fr} = \sigma\delta(\mathbf{n}_{wall} \cdot \mathbf{n}_{int} - cos\theta_w)\mathbf{n}_{int} - \frac{\mu}{\beta}\mathbf{u} \tag{3.7}$$

By default, the slip length (β), and the contact angle θ_w are set to the local mesh element size (h) and $\pi/2$ respectively.

Geometry

For 3D-printing three different microfluidic chips have been designed and simulated: a T-junction, and two different geometries of flow-focusing junctions. However, to reduce the computational time only the junctions shown in figure 3.1 have been simulated.

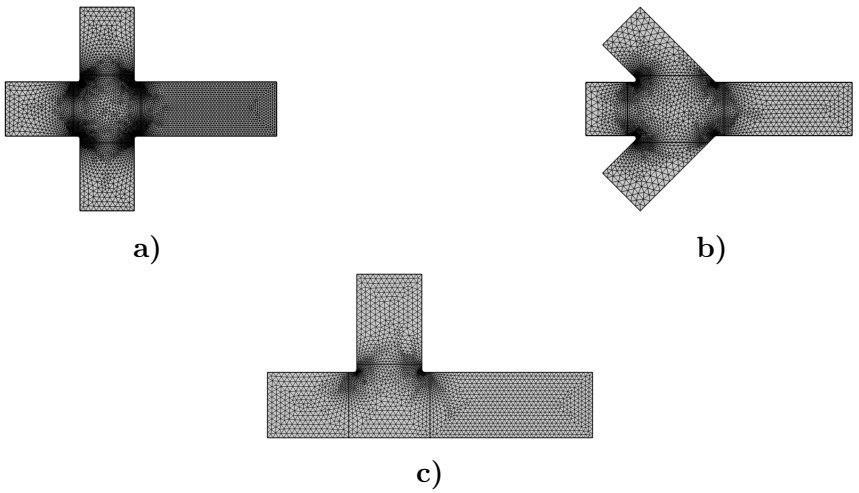

Figure 3.1. Geometries and meshes in numerical simulation of the different droplet generation junctions manufactured with 3D-printing. **a)** 90º flow-focusing junction, **b)** 45º flow-focusing junction, and **c)** T-junction.

All three geometries shown above have a total length of 2000 μm, from inlet to outlet, and the channels are 400 μ in height. To reduce the sharp edges, and therefore, the computational time, a fillet of 20 μm radius has been applied to all the junction's corners. In table 3.2 the fixed parameters used in the simulations are shown. However, different values of capillary number (Ca), flow rate (R_f), oil-phase velocity, and dispersed-phase velocity were used throughout the simulations.

Simulation parameters			
ρ_c	895 kg/m^3	ε	$5 \cdot 10^{-6}$ m
μ_c	27.64·10^{-3} Pa·s	γ	0.1 m/s
ρ_d	1000 kg/m^3 [169], [170]	β	5·10^{-6} m
μ_d	250·10^{-3} Pa·s [169], [170]	θ_w	$\pi - 2.7925268$ rad ($\sim 20^{\text{o}}$)
σ	9.4·10^{-3}		

Table 3.2. Initial simulation parameters for the alginate nanoemulsions.

For soft lithography six different microfluidic chips have been designed and simulated: T-junction, and two different geometries of flow-focusing junctions. Each junction has been duplicated, as one has a minimum element size of 100 μm, and the other geometry has a minimum size element of 48 μm. However, to reduce the computational time only the junctions shown in figure 3.2 have been simulated

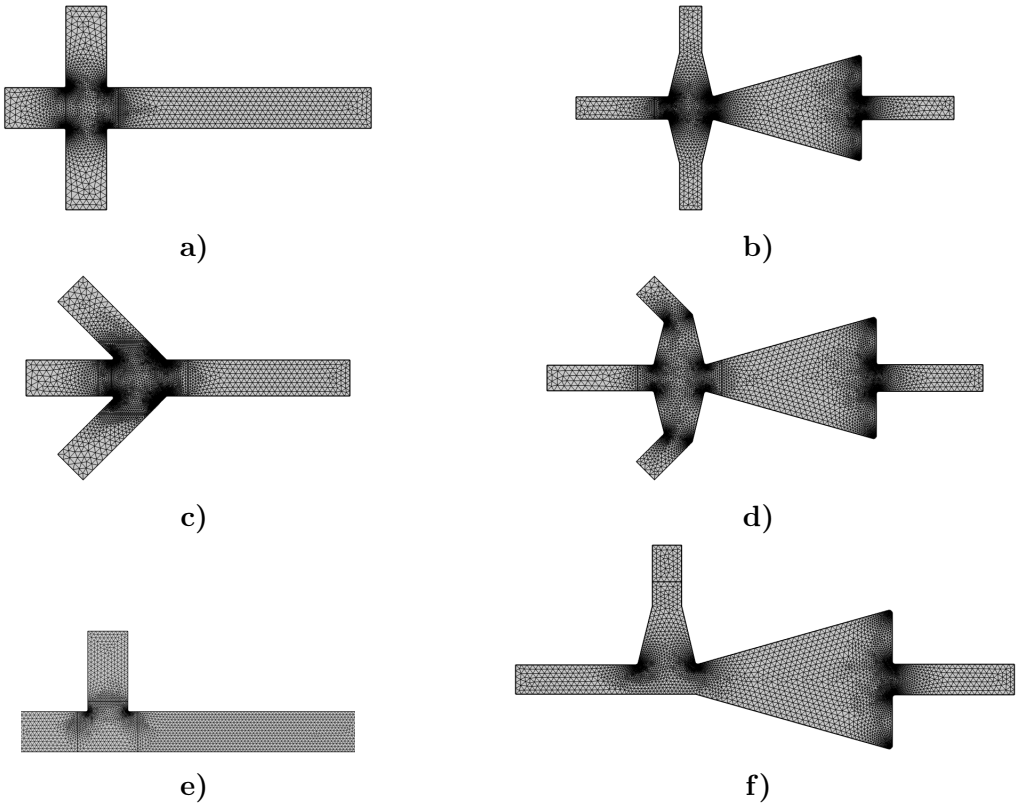

Figure 3.2. Geometries and meshes in numerical simulation of the different droplet generation junctions. **a)** 90º flow-focusing junction, **b)** 45º flow-focusing junction, and **c)** T-junction.

The simulation approach is to achieve a converging model with a rough mesh size and then refine the results with a smaller mesh until the solution no longer shows any significant change. The different models had user-controlled meshes calibrated for fluid dynamics. As mentioned before, the geometries were divided into different domains to reduce the computational time. The flow-focusing junction meshes had fine element sizes, while the rest of the geometry has a (custom) mesh with extra fine (size) element sizes. The simulated

time was based on the time needed to reach a steady-state of homogeneous sized droplets, also considering the computational cost.

3.3 3D-Printing of Microfluidic Chip

Once the the microfluidic chip designs were done, the AutoCAD file was saved as .STL file so it can be opened by Phonon Workshop, a 3D slicer software that converts the .STL files to .PWS, a file format that can be read by the 3D printer.

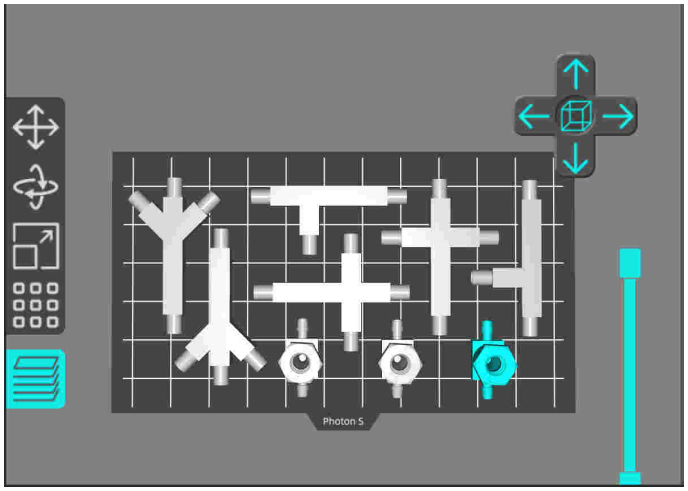

Figure 3.3. Screenshot of Phonon Workshop. In dark grey is the 3D-printer surface, and in white the geometries to print. In blue is a selected geometry.

In figure 3.3 is shown a screenshot of Phonon Workshop. The dark grey grid is the 3D-printer surface, and in white are the different microfluidic chips. The layer thickness was set to 40 μm, the normal exposure time was set to 5 seconds, the off-time was set to 8 seconds, the bottom exposure time was set to 60 seconds, and the bottom layer(s) was set to 3. The other parameters such as Z-lift distance, Z-lift speed, or Z-retract speed were kept as default.

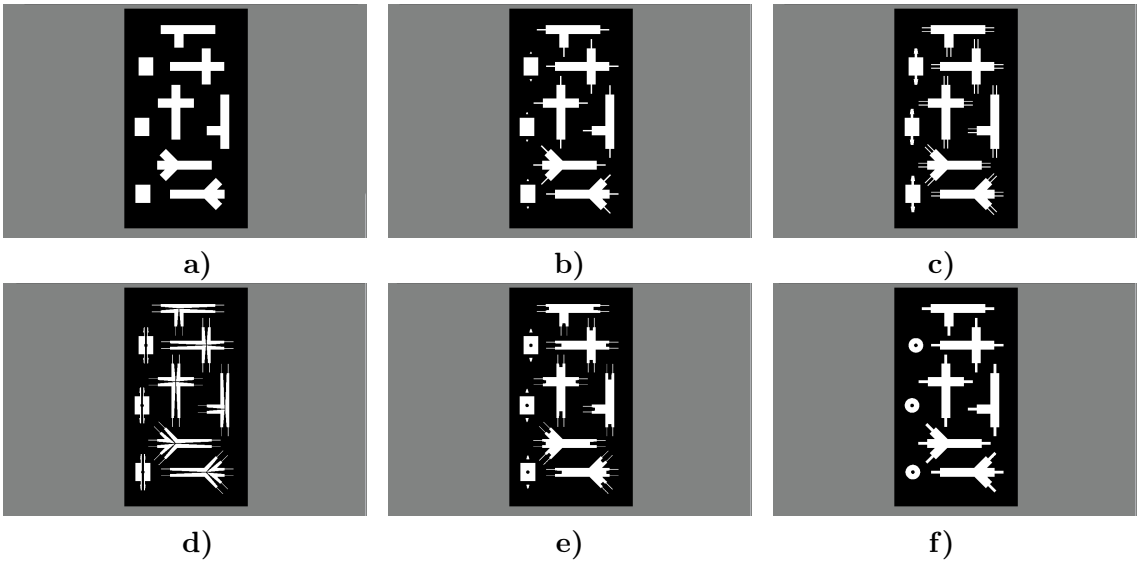

Figure 3.4. Screenshots of the different slices generated by Photon Workshop software. **a)** bottom layer (layer 0), **b)** layer 13, **c)** layer 24, **d)** layer 62, **d)** layer 83, and **f)** layer 108.

In figure 3.4 are shown six different slices generated by Photon Workshop. Each slice corresponds to a different printing time point. The 3D-printing of all the microfluidic chips shown in figure 3.3 has 378 layers in total, with an estimated printing time of around 2 hours, and an estimated printing volume of 8.859 mL of resin.

Anycubic Photon S Technical Data	
Printing Technology	LCD-based SLA 3D Printer
Light Source	Integrated UV light (405 nm)
XY-resolution	47 μm/pixel
Printing Speed	20 mm/h
Printing Material	405 nm Photosensitive Resin

Table 3.3. Technical data of the printer used for the 3D-printing of microchips. Data collected from the Anycubic webpage. [171]

The specifications of the 3D-printer, as well as the materials and equipment used for 3D-printing are listed in table 3.3 and table 3.4 respectively.

Material	**CAS no**	**Lot/Serial no**	**Supplier**
Isopropanol	0067-63-0		Sigma Aldrich
Photon S			Anycubic Technology
Photon Workshop Software			Anycubic Technology
Standard Clear UV resin			Prima Creator
Wash Away Resin			Prima Creator
Wash & Cure			Anycubic Technology

Table 3.4. Chemicals and equipment used in the 3D-printing of the microchips.

The procedure for 3D-printing is the following: The resin photoprotector is removed, and the resin volume is checked. Then, the .PWS file with the designs is selected and the 3D-printing starts. Once the 3D-printing is done the top part of the 3D-printer is carefully detached, as the printings are stuck there. Carefully, with the help of a metallic spatula, the 3D-printings are detached. Once the printings have been separated, the excess of resin of the lid is cleaned with isopropanol, and attached again to the printer. If the printed microchips have channels, these are unclogged by injecting nitrogen with a nitrogen gas. Then, the microchips are washed with a "resin away" bath for two to four minutes. Anycubic Wash & Cure is used for a last curing step, in which the microchips are exposed to a UV light of 405 nm for four minutes.

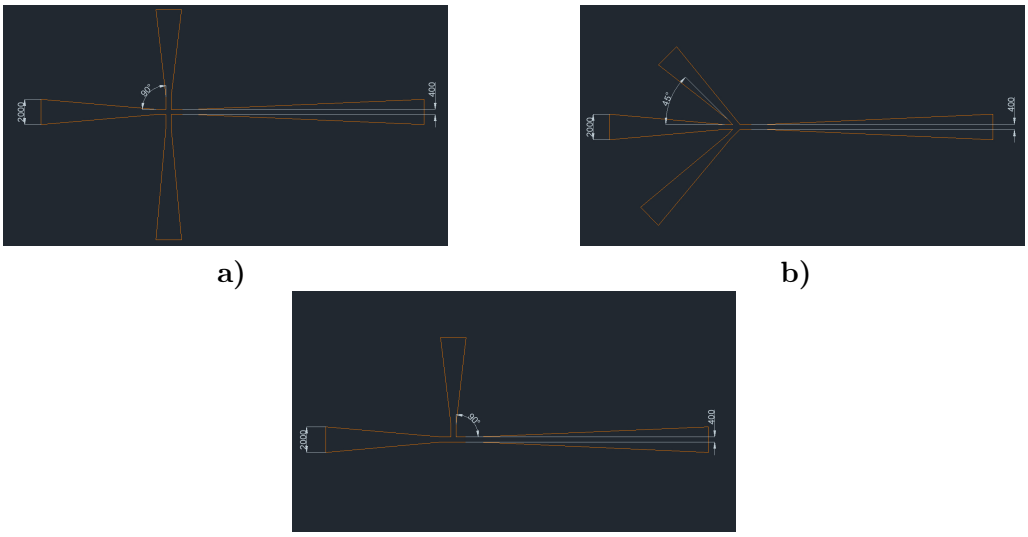

Figure 3.5. Dimensions of the channels designed with AutoCAD. **a)** 90º flow-focusing junction, **b)** 45º flow-focusing junction, and **c)** T-junction. dimensions are in μm.

For all the designs printed, each geometry had the same channel dimensions, as shown in figure 3.5. All channels were 3 mm in length, from inlet to outlet (left to right). The initial cross-section of the inlets is 2 mm in height which decreases over a length of 9 mm to a final cross-section of 400 μm. On the other hand, the outlet has an initial cross-section of 400 μm which increases over a length of 1.8 mm to a final cross-section of 2 mm.

3.3.1 PDMS Casting

Before casting the microchips in PDMS, the molds were washed in water at 80° overnight to remove resin residues that prevent the polymerisation of the PDMS. The casting of the microchips is described below, and the material used is listed in table 3.5.

Material	CAS no	Lot/Serial no	Supplier
Heat Cabinet		Kelvitron	Heraeus Instruments
Silicone Elastomer		0006065320	Sylgard
Silicone Elastomer Curing Agent		0006387182	Sylgard
Vacuum Chamber			

Table 3.5. Chemicals and equipment used to cast the microchips using 3D-printed negative molds.

To cast the microfluidic chips in PDMS a mixture of silane and curing agent with a 1:10 ratio was prepared and poured over the negative mold and frame. The mold containing the PDMS was placed in a vacuum chamber to degasify until no bubbles were visible. Then, the mold with PDMS was baked overnight in a heating cabinet at 80°C. After baking, the PDMS is cooled down at room temperature, and the PDMS is carefully peeled off the mold with a scalpel, cut, and pierced. Last, is the bonding of the PDMS with glass to close the channels. The bonding is possible after O_2 plasma etching for 2-10 minutes which cleans and activates the PDMS surface by transforming the Si-CH_3 terminals to Si-OH allowing the formation of Si-O-Si bonds with the glass.

3.4 Casting of Microfluidic Chip by Soft Lithography

The first step to cast the microfluidic chips using soft-lithography is to design the photomasks. The photomasks were designed using LayoutEditor. Six photomasks were designed, three photomasks, consisting on a T-junction, 90º flow-focusing geometry, and 45º flow-focusing geometry were designed with a minimum size element of 100 μm; the other three photomasks are also a T-junction, 90º flow-focusing geometry, and 45º flow-focusing geometry, but with a minimum size element of 48 μm and a slightly different geometry.

3.5 Droplet Generation

This section serves to describe the different procedures used to generate droplets. In table 3.6 is listed all the chemicals and equipment used in the procedures.

Material	CAS no	Lot/Serial no	Supplier
Calcium Chloride Dihydrate	10035-04-8	1.02382.0250	Supelco
Electrospinner 2.2.D-500			Y flow Nanotechnology Solutions
Ethanol 70%	64-17-5		
Magnetic stirrer			
Sodium Alginate	9005-38-3	MKBX6322V	Sigma Aldrich
Sodium Dodecyl Sulfate	151-21-3	STBD6276V	Sigma Aldrich
Span 80®	1338-43-8	MKCN9843	Sigma Aldrich
Syringe Pump		NE-1010X	Darwin microfluidics
T25 Digital ULTRA TURRAX®			IKA
Undecanol	112-42-5	A7Y2KEG	TCI Chemicals

Table 3.6. Chemicals and equipment used in microfluidic droplet generation.

3.5.1 Phase Solutions Preparation

Here are described the preparation of the different solutions used to generate droplets. The chemicals used are listed in table 3.6.

For electrospraying solutions with 1 wt% and 4 wt% alginate were prepared by dissolving sodium alginate into 30% ethanol (EtOH). A calcium bath was also prepared by dissolving $CaCl_2 \cdot 2H_2O$ (25 g/L) in water.

For high-speed stirring and microfluidics the solutions used were prepared as follows. The continuous-phase was prepared by dissolving calcium chloride dihydrate ($CaCl_2 \cdot 2H_2O$) in EtOH 70% in an Eppendorff, and then added to a bluecap bottle containing undecanol and Span 80®. The final oil solution has a 5 wt% Span 80 ®, and 1 wt% Ca^{2+} ions. The dispersed-phase was prepared by dissolving sodium alginate (1 wt%) and sodium dodecyl sulfate (5 wt%) in miliQ water. An additional solution was prepared for the collection of the droplets for the microfluidic chips. The collecting solution was

prepared by dissolving $CaCl_2 \cdot 2H_2O$ (10 wt%) in EtOH 70% and then mixing it with undecanol.

For the encapsulation of plasmid DNA, phosphate-buffered saline (PBS) solution is used instead of water.

3.5.2 Electrospray

The electrospray procedure is the following: the alginate solution is loaded into a syringe and connected to the pump, while the calcium bath is placed in a beaker inside the electrospinning chamber. The calcium bath is made conductive by placing an electrode inside connected to the base of the chamber. Then the chamber is closed and the electrospinner is turned on, enabling the movement of the emitter's x and y-axis. After adjusting the flow rate to 70 μL/min the pump was turned on. The voltage of the emitter is adjusted until a Taylor cone is observed as shown in figure 3.6, while the voltage of the calcium bath was kept at 0 (ground).

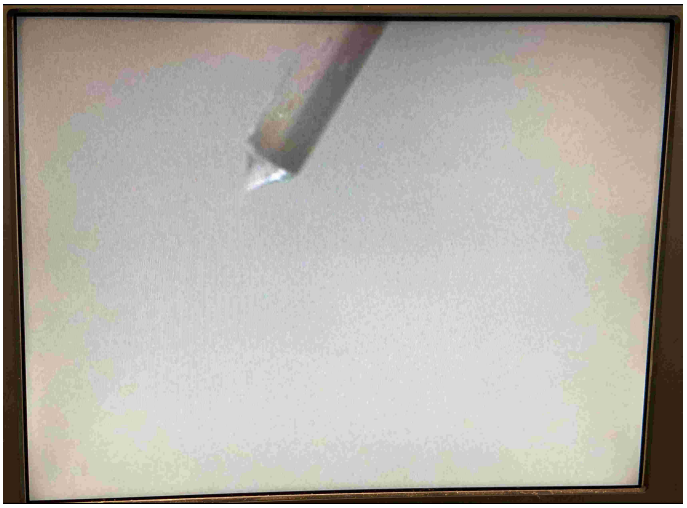

Figure 3.6. Taylor cone generated in during the electrospray procedure.

When the electrospray is done the emitter's voltage is turned off and the sample present in the calcium bath is transferred into 50 mL grinder tubes. The pipes of the electrospinner are rinsed a couple of times with water to avoid clogging and the machine is turned off. The sample is centrifugated at 7,000 rpm for 15 minutes at 21°C. The supernatant was carefully removed. Both pellet and supernatant were kept for later analysis.

3.5.3 High-Speed Stirring

High-speed stirring was carried out to reduce the size of the droplets previously obtained with the microfluidic chips.

Different droplet generation experiments were carried out using the high-speed stirring (HSS) technique. However, the procedure is the same for all the experiments, and is described below. The chemicals and equipment used are listed in table 3.6.

S25N-8G-ST Technical Data	
Stator diameter	8 mm
Rotor diameter	6.1 mm
Gap between rotor and stator	0.25 mm
Maximum speed	25000 rpm
Circumferential maximum speed	8.0 m/s

Table 3.7. Technical data of the rotor-stator used for the high-speed stirring

In table 3.7 are shown the specifications of the rotor-stator used in the homogeniser (T25 Digital ULTRA TURRAX®) to apply high shear stress to the two-phase mixture to create the nanoemulsions. The droplet generation protocol for HSS is the following: In a 50 mL Greiner tube were added 10 mL of the oil phase and the homogeniser was set. Then, 1 mL of alginate solution was added. Two different protocols were tested. In the first protocol, the homogeniser is turned on after adding the alginate solution. However, in the second protocol, the homogeniser is turned on before adding the alginate solution. Additionally to when the alginate solution was added, two different velocities 15,000 and 20,000 rpm were tested.

3.6 Droplet Characterisation

The droplets were characterised using a nanoparticle tracking analysis (NTA) and scanning electron microscopy (SEM). In table 3.8 is listed all material used.

Material	CAS no	Lot/Serial no	Supplier
Acetone	67-64-1		
Ethanol	64-17-5		
MiliQ water			
Nanoparticles Analysis System			NanoSight
Nitrogen Gun			
Isopropanol	67-63-0		
Scanning Electron Microscope			Gemini
Sputter Coater		S150B	Edwards
Ultrasonic Cleaner		Branson 2510	VWR international

Table 3.8. Chemicals and equipment used for droplet characterisation using NTA.

The characterisation procedure using the NTA is the following. The samples were loaded into the NTA chamber using a syringe making sure that no bubbles were present. Then power supply is connected and the laser is turned on. Before the analysis, the sample is focused using the microscope lenses, and the temperature in the chamber is measured. The temperature is then added to the measurement program. For the characterisation of the droplets, a standard measurement was carried out, with 3 captures per measurement,

and a capture duration of 60 seconds. Before running the experiment, the screen gain and camera level are adjusted.

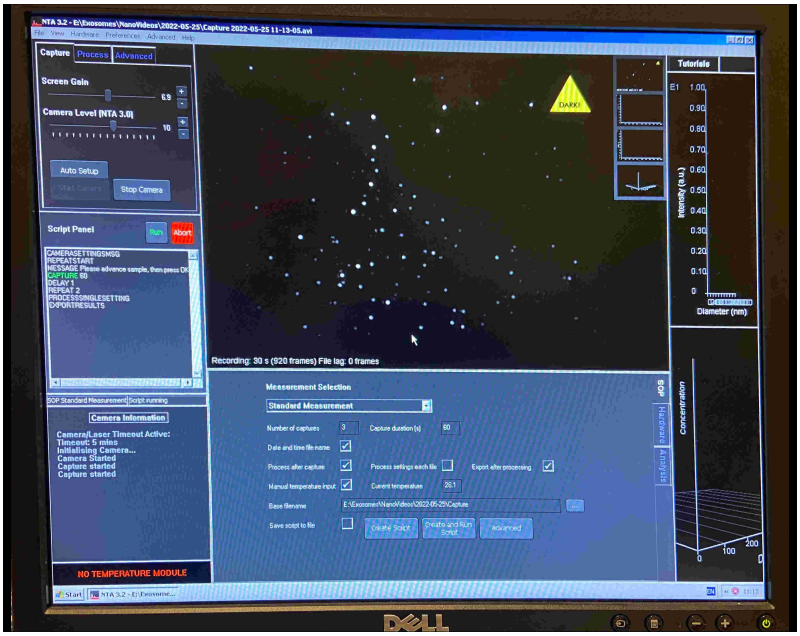

Figure 3.7. Screenshot of NTA v3.2. In the centre of the image droplets in suspension. On the left screen gain and camera level. On the bottom is the type of measurement with a number of captures and capture time.

After the measurement comes the processing, where the screen gain and detection threshold are adjusted, to visualise properly the particles and to avoid identifying noise as nanoparticles respectively. Once the experiment is over the sample is removed, and the chamber is cleaned by rinsing it with MiliQ water, ethanol, and dried out with a nitrogen gun.

To characterise the droplets with SEM, the protocol to prepare the samples is the following: A silica wafer was placed into a Greiner tube containing acetone, and sonicated for 10 minutes. The silica wafer is carefully picked up with tweezers and rinsed with isopropanpol the wafer is blow-dried with a nitrogen gun to avoid any impurity on the surface. Once the wafer is dried out the sample can be added to the surface. Three different protocols were used to deposit the samples onto the silica wafer substrate. In one the sample was left to dry, and on the other two, the sample was added and left to incubate for 5 and 10 minutes respectively. Then, the wafer is rinsed with distilled water and blow-dried with a nitrogen gun.

As the sample is non-conductive, before characterising it with the SEM, the sample is made conductive by gold sputtering with the following procedure. The samples are placed in a pin mount which is placed inside the sputter coater. Then the pump is turned on by pressing the "R.P" button. When the pressure has dropped to 10^{-1} bar Argon gas is flushed inside the chamber by opening the "pressure control" until the pressure inside the chamber reaches $\sim 3 \cdot 10^{-1}$. Then, the argon plasma is ignited (figure 3.8) by pressing simultaneously the high tension (H.T) and time (time) buttons. The deposition time is set to 1.5 minutes, and a current of 30 mA.

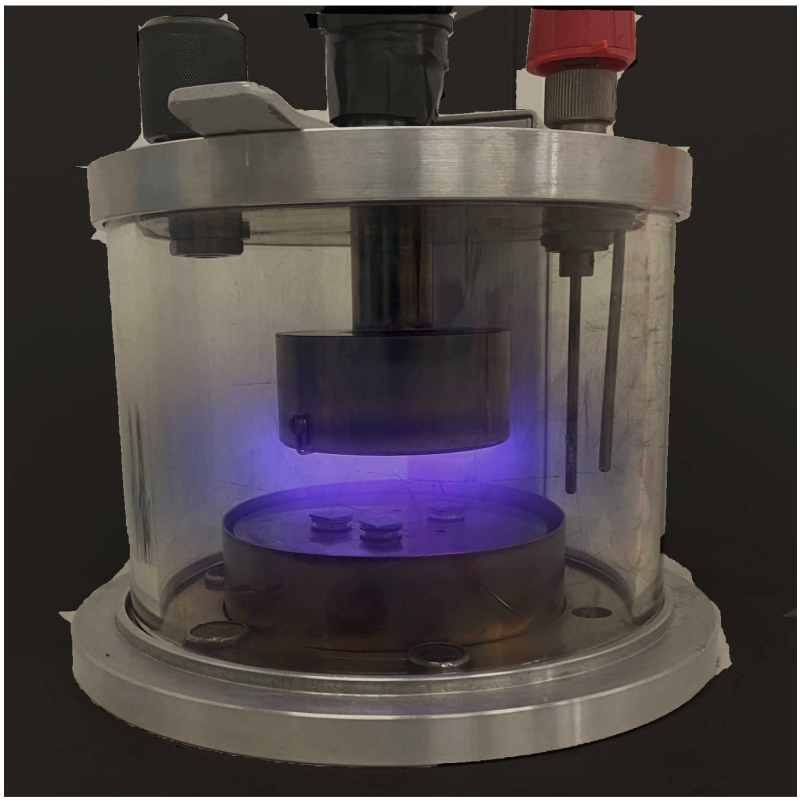

Figure 3.8. Image of Argon plasma used for the sputter coating of the samples.

Once the deposition is done, the "H.T" and "time" buttons are simultaneously turned off, the "pressure control" valve is closed, and the pump is turned off. To remove the samples, the chamber is vented by opening the "gas/air admit".

Once coated the samples can be introduced into the SEM for their characterisation with the following protocol. First, the chamber valve is closed and the loading chamber is purged (i.e., the vacuum is broken) so the pin mount with the samples can be introduced on top of the stage. Once loaded, the air is pumped out of the chamber. To introduce the mount into the inner chamber, the stage must be in the exchange position, then the mount is transferred with a manipulator, which is later removed. Once the mount is inside the chamber is purged bit, and the inner column chamber valve is opened. Then, the high tension (ETH) in the column is switched on ($\sim$ 20 keV). To remove the samples the reverse procedure is carried out.

3.7 Solutions and Medium Preparation

This section serves to describe the preparation of different growth mediums used in the experiments carried out throughout the project. All chemicals and equipment used are listed in table 3.9.

Material	CAS no	Lot/Serial no	Supplier
Agar	9012-36-6	080M1575	Sigma Aldrich
Autoclave			LH Laboratory services
Kanamycin Monosulfate	25389-94-0	104K01645	Sigma Aldrich
Sodium Chloride	7647-14-5	17L184138	VWR Life Sciences
Yeast Extract	8013-01-2	M0186W	VWR Chemicals

Table 3.9. Chemicals and equipment used for medium preparation.

3.7.1 Lysogeny Broth Growth Medium

Lysogeny broth (LB) growth medium was prepared by dissolving sodium chloride (10 g/L), tryptone (10 g/L), and yeast extract (5 g/L) in Mili-Q water. Later, to make LB-agar stock, agar (15 g/L) was dissolved in the LB medium. Both, LB medium and LB-agar were autoclaved. Then, LB medium was stored at 4^{o}C, and LB-agar solution was stored at 60^{o}C, ready to have kanamycin (30 mg/L) added, and used for plating.

3.8 Isolation of Plasmid DNA from *Escherichia Coli*

Different procedures were carried out for the amplification and isolation of the plasmid DNA from *Escherichia coli* (*E. coli*) for their encapsulation in the nanoemulsions.

3.8.1 Bacterial Growth

The chemicals and equipment used for the bacterial growth are listed in table 3.11, and the procedure followed is described below.

Material	CAS no	Lot/Serial no	Supplier
Incubator		Klevitron t	Heraeus Instrument
Incubator		Innova 4230	New Brunswick Scientific
Kanamycin			In house stock
Lysogeny Broth Medium		subsection 3.7.1	In house stock

Table 3.10. Chemicals and equipment used for *E. coli* growth

First, colonies of *E. coli* cells containing the desired plasmid were inoculated into new sterile lysogeny broth kanamycin (LB-kan) agarplates. The LB-kan agarplates were incubated at 37^{o}C for 18 hours. After the incubation, the plates were stored in the fridge at 4^{o}C for later use. For the plasmid isolation, precultures of *E. coli* cells were prepared by transferring *E. coli* cells into a 10 mL culture tube containing 5 mL of LB medium and kanamycin (30

mg/L). The solution was mixed until the transferred cells were completely dissolved. The preculture was incubated overnight at 37ºC and 300 rpm.

3.8.2 Plasmid Isolation

The chemicals and equipment used for the plasmid isolation are listed in table 3.10, and the procedure followed is described below.

Material	CAS no	Lot/Serial no	Supplier
Centrifuge		5804R and 5824R	VWR International
GeneJET Plasmid MiniPrep Kit		00714520	Thermofisher Scientific
Microcentrifuge			
Vortex		MS2 Minishaker	VWR Internation

Table 3.11. Chemicals and equipment used for plasmid isolation.

For the isolation of the plasmid DNA, the GeneJET Plasmid Miniprep Kit was used. The kit consists of an SDS/alkaline cell lysis which is then neutralised creating the optimal conditions to bind the plasmid DNA to the silica-based membrane in a spin column. The procedure is the following: The precultures were centrifuged at 8,000 rpm for 7 minutes at 21ºC. The supernatant, composed of the LB medium, was discarded by decantation, which left a pellet made up of cells. The pellet was dried out as much as possible by pouring the remaining LB medium over a tissue to avoid any interference of LB with the lysis solution. The pellet was then resuspended in 250 μL of resuspension solution, and vortexed until completely dissolved. The solution was then transferred into a new Eppendorf tube. Then, 250 μL of the lysis solution was added and the solution was mixed gently by flipping the tube. 350 μL of the neutralising buffer was added to the Eppendorf tube, and the solution was mixed once again. The solution was centrifuged, in a microcentrifuge at 12,000g for 10 minutes.
The supernatant, composed of plasmid DNA, was carefully pipetted and transferred into the spin column, and the pellet was discarded. The spin column was centrifuged for a minute at 12,000 g. The flowthrough, composed of debris of similar size to the plasmid DNA, was decanted away. The material left in the spin column was washed with 500 μL of the wash solution. The column was once again centrifuged under the same conditions for a minute and the flowthrough was discarded. This step was repeated once more, before centrifuging the columns for one minute without the wash solution to remove the remaining washing solution. The filter part of the spin column was moved to a new Eppendorf tube and 50 μL of the elution buffer were carefully added, ensuring the tip of the pipette was close to the membrane without touching it. The tube was incubated for two minutes at room temperature, and then centrifuged for another two minutes at 12,000 rpm. The supernatant was collected and transferred into a new Eppendorf tube and stored at 4ºC for later use. The presence of the plasmid was confirmed through agarose gel electrophoresis.

3.8.3 Plasmid Digestion

To determine the presence of the desired plasmid DNA, the plasmid DNA must be linearized by restriction enzyme digestion. The chemicals and equipment used to linearise the plasmid DNA are listed in table 3.12, and the procedure followed is described below.

Material	CAS no	Lot/Serial no	Supplier
AccuGENE Molecular Biology Water	8MB248	Lonza	
CutSmart 10x Buffer	B7204S	10015396	New England Biolabs
EcoRI-HF	R3101S	0151803	New England Biolabs
Microcentrifuge			
NdeI	#R0111S	0311409	New England Biolabs
PICODROP		Model 90021	ISS
Thermomixer Comfort			Eppendorff

Table 3.12. Chemicals and equipment used for the digestion of the plasmid DNA.

To linearise the plasmid DNA, 2 μL of isolated DNA (210 μg/mL) was mixed with 39 μL of DNase free water, 5 μL of 10x CutSmart buffer, and 2 μL of *NdeI* and *EcoRI-HF*. The solution, with a total volume of 50 μL, is centrifugated for one minute at 8,000 rpm and then incubated at 37^{o}C for one hour.

3.8.4 Agarose Gel Electrophoresis

The chemicals and equipment used for the plasmid isolation are listed in table 3.13, and the procedure followed is described below.

Material	CAS no	Lot/Serial no	Supplier
1 kb DNA Ladder	N3232S	100971	New England BioLabs
Agarose	9012-36-6	19H2056197	VWR Life Sciences
Electrophoresis equipment		Power PAC 3000	Bio-Rad
Ethidium Bromide	1239-45-8	SLBF7132V	Sigma Aldrich
Gel Loading Dye (6x)	B7024S	10055732	New England BioLabs
Heat Cabinet			Karner and Co
Power Supply			Bio-Rad
TAE Buffer			In house stock

Table 3.13. Chemicals and equipment used for agarose gel electrophoresis

First, a 1% agarose stock solution is produced by mixing agarose (10g/L) in 1x TAE buffer. The solution is stirred and later heated in a microwave until the solution becomes completely clear. The stock is stored in a heat cabinet at 60^{o}C, for later use.

The agarose gel is prepared by mixing approximately 30 mL of 1% agarose with the minimum amount of ethidium bromide, and transferred to a tray. To cover the tray

uniformly the tray is gently shaken, and then a comb is placed near the top to create the wells. Once gelated the tray is transferred to the electrophoresis chamber. The gel is completely submerged in 1x TAE buffer and the comb is removed. The wells are loaded with 6 μL of 1 kb DNA ladder and 6 μL of the sample, which consists of 1 μL of loading dye and 5 μL of the digested DNA. Once loaded, the lid is placed on the chamber. The electrophoresis is run at 60 V for an hour. The gel is analysed with UV light.

3.9 Mammalian Cell Culture and Trnasfection

This section serves to describe the culturing of HeLa cells used in this project. The materials used is listed in table 3.14.

Material	CAS no	Lot/Serial no	Supplier
Centrifugue Tube (15 mL, 50 mL)		Hounisen	
CO_2 Incubator		HERAcell vios 160i	Thermofisher Scientific
Culture Flask (75 mL)		Greiner	
DMEM			In house stock
Fluorescent Microscope		Axio Observer Z1	ZEISS
Hemocytometer			
Laminar flow fume hood		Airstream®	Holm & Halby
EnSpire Multimode Plate Reader		23001274	Perkin Elmer
PBS (1x)	10294922		Fischer Scientific
Poly-L-Lysine (0.01%)	75k2381		Sigma Aldrich
Trypsine/EDTA (0.05% in PBS)	15400-054		Thermo Fischer Scientific
96-well plate			

Table 3.14. Chemicals and equipment used for the characterisation of the nanoemulsion transfection.

The HeLa cells were cultivated in 75 cm^2 flasks as follows. First, an old passage of cells was placed under the inverted microscope to estimate the confluence. Then the medium was carefully removed and discarded, and fresh medium was added dropwise onto the cells. Then, the cells were incubated in a 5% CO_2 incubator at 37°C. For splitting and passaging the cells, the medium was carefully removed, and the cells were rinsed by adding approximately 15 mL of PBS, the flask was tipped to ensure all cells were covered. The PBS is then removed, and $\sim$ 3.75 mL of Trypsin-EDTA is added. The cells are incubated at 37°C until they are detached from the flask (approximately 3-4 minutes). The Trypsin-EDTA is inactivated by adding 7.5-11.25 mL of fresh medium and transferred into a new 15 mL tube. If the cell counting is too low, the cells are centrifuged at 300 g for 5 minutes, with both acceleration and break of 9, and the supernatant is removed, and the cells are resuspended in fresh medium.

The cell counting is the following. The hemocytometer is cleaned by rubbing 70% ethanol before covering the chamber with a cover glass. Then, 10 μL of cells are loaded into the chamber, and the hemocytometer is placed under an inverted microscope with a

10x objective. The desirable cell counting should have more than 100 cells in total, with 25 to 150 cells per quadrant. After the cell counting, the concentration of cells and the total cell counts are calculated as follows:

$$\textbf{Cell concentration} = \frac{\text{Cells counted}}{\#\text{ quadrants}} \cdot 10^4 \tag{3.8}$$

$$\textbf{Cell count} = [\text{Cells}] \times Volume \tag{3.9}$$

After calculating the total amount of cells, the number of cells was adjusted to plate 200 μL of suspended cells into a 96-well plate with a cell concentration of $8 \cdot 10^3$ cells/well and then incubated overnight at 37°C in a 5% CO_2 incubator for later transfection.

For the transfection, the medium was carefully removed with a pipette and a total volume of 200 μL of fresh medium mixed with the samples was added. The cells were then incubated for 24, and 48 hours.
The cells were incubated with free plasmid DNA, plasmid DNA with Poly-L-Lysine, and droplets obtained with electrospraying. Different samples obtained via ES are E5+10, E7+3_7, and E7+3_5.Where the 5 and 7 correspond to the total volume of alginate solution, 10 and 3 correspond to the amount of plasmid DNA (μL), and the subscripts 7 and 5 are related to the flow rate used for electrospraying, and correspond to 70 and 50 μL/min respectively. A study carried out by Daniel Joubert *et al.* in 2003 showed that incubating DNA with poly-L-Lysine (pll) with molecular weight ranging from 9 to 40 KDa increased the transfection efficiency. [172] The incubation protocol of the pll with DNA is the following. A 1:2 mass ratio mixture of DNA and pll (75-150 kDa) was incubated for 30 minutes at room temperature (RT). Then, the mixture was added to the 96-well plate and incubated with the HeLa cells.

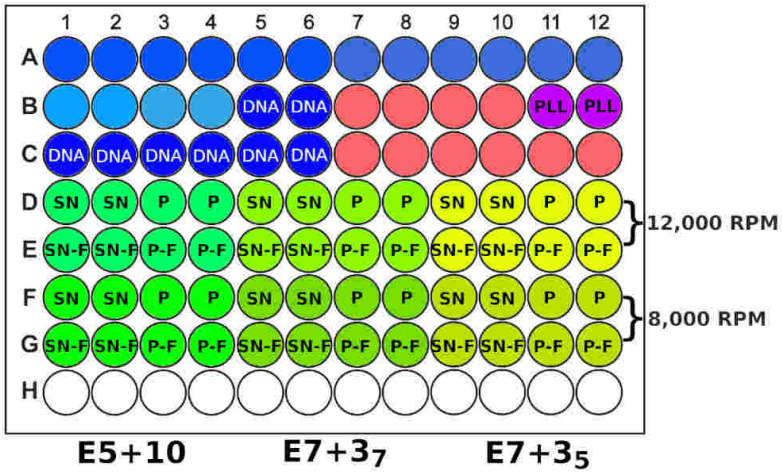

Figure 3.9. 96-well plate distribution.

Different purification procedures were tested for each sample. The purification procedure was carried out by centrifugation at 8,000 and 12,000 rpm, and an additional sterilisation by filtration (0.47 μm filter) was also carried out. Therefore, a total of 8 samples were obtained from the each sample, supernatant and filtered supernatant (SN and SN-F) for 8,000 and 12,000 rpm, and the pellet and filtered pellet (P and P-F) for 8,000 and 12,000

rpm. The distribution of the samples is shown in figure 3.9. A control with only plasmid DNA is shown in dark blue (B5, B6, and C1 to C6), a negative control in red (B7 to B10, and C7 to C12). The samples that contain the droplets created with ES are from D1 to G12. Wells 1 to 4 correspond to the E5+10, 5 to 8 correspond to E7+3_7, and 9 to 12 correspond to E7+3_5. Rows D and E, were centrifugated at 12,000 rpm, while rows F and G were centrifugated at 8,000 rpm. Furthermore, rows D and E were not filtered, while rows D and G, were filtered.

The transfection was characterised 24 and 48 hours after the incubation: First, the 96-well plate was checked with a fluorometer. For that, a new measurement protocol (SOP) was created to measure the TagRFP, the excitation wavelength was set at 555 nm, and the emission was measured from the bottom of the plate at 584 nm. Once the SOP was created each well was assigned either a control (plasmid), blank (negative), or unknown (sample), then the 96-well plate was loaded into the fluorometer and the SOP was run.

The transfection was also characterised using an inverted phase-contrast fluorescence microscope. The parameters, such as excitation wavelength, were set with ZEISS ZEN blue software. The cells were then placed under the microscope, focused, and the wells of interest were checked.

Chapter 4

Results

In this chapter, the results obtained throughout the project will be introduced.

4.1 3D printing

Several microchips were designed with AutoCAD and printed in this project. The first microchips printed are shown in figure 4.1. Where the T-junction geometry (**a)**) was $40 \times 17.5 \times 0.5$ mm, the 90° flow-focusing geometry (**b)**) was $40 \times 30 \times 0.5$ mm, and the 45° flow-focusing geometry (**b)**) was $40 \times 24.159 \times 0.5$ mm$(w \times h \times t)$.

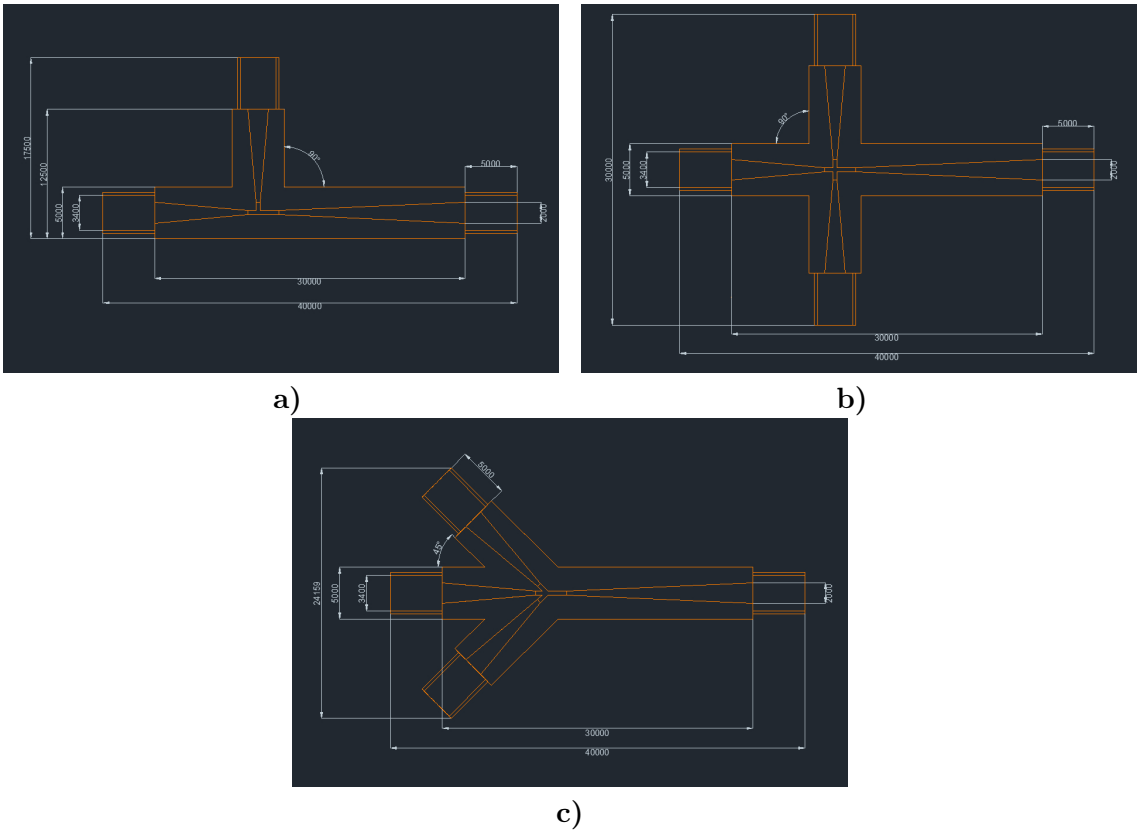

a) **b)**

c)

Figure 4.1. First AutoCAD designs of the microfluidic chips. **a)** T-Junction geometry, **b)** 90º flow-focusing geometry, and **c)** 45º flow-focusing geometry. Units are in micrometres.

To be able to connect the microchip to the syringe pump, a 5 mm long circular adapter with a 3.4 mm inner diameter has been added to all inlets, and the outlet. However, the thickness of the adapter was too thin and broke after the cleaning of the channels with the nitrogen gun.

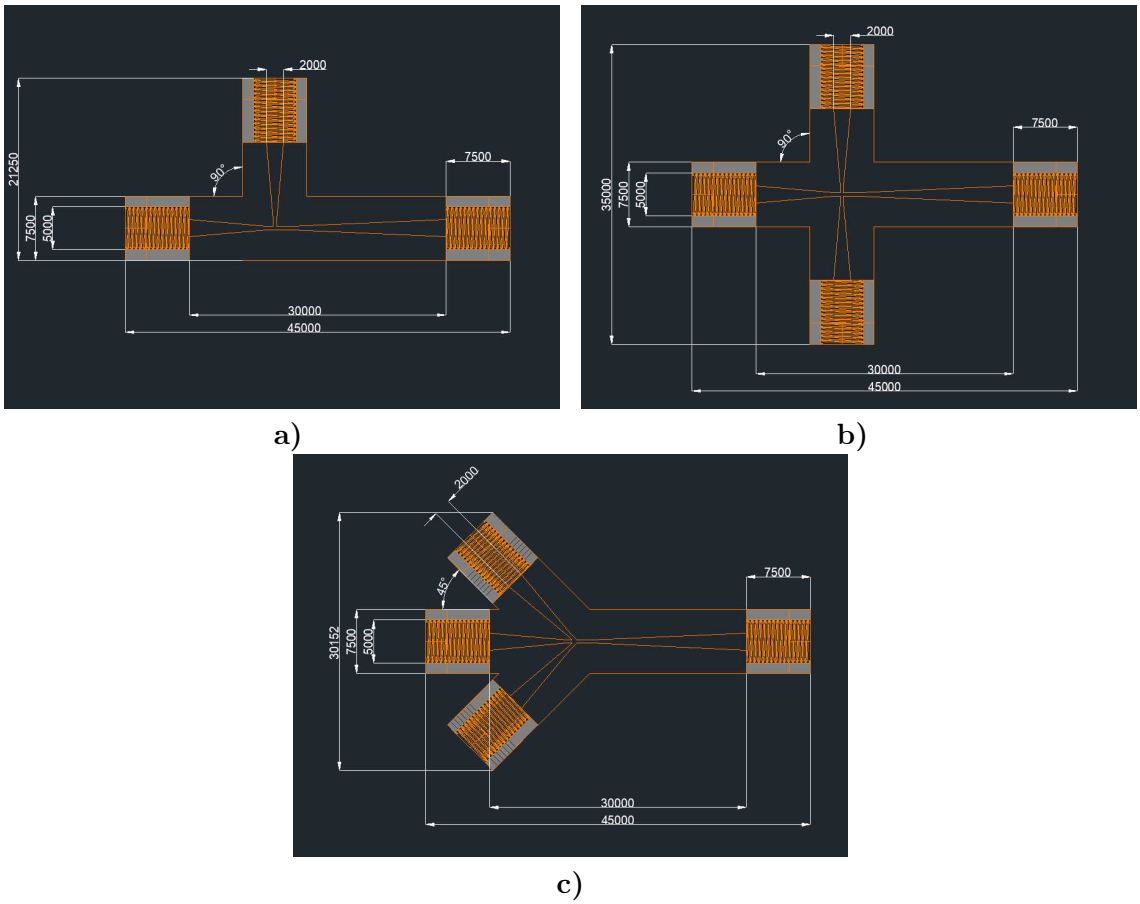

Figure 4.2. AutoCAD designs of the microfluidic chips with a thread at all inlets and outlet. **a)** T-Junction geometry, **b)** 90º flow-focusing geometry, and **c)** 45º flow-focusing geometry. Units are in micrometres.

Thicker microchips, with a different adapter were designed as shown in figure 4.2. The adapter consists of a 7.5 mm long M5x0.5 nut with an external diameter of 7.5 mm and a nominal hole diameter of 5 mm with a fine pitch of 0.5 mm (see appendix A). The dimensions of the microchips were $45 \times 21.25 \times 7.5$ mm for the T-junction (**a)**), $45 \times 35 \times 7.5$ mm for the 90° flow-focusing geometry (**b)**), and $45 \times 30.152 \times 7.5$ mm for the 90° flow-focusing geometry (**c)**). However, the channels of the microchips could not be unclogged.

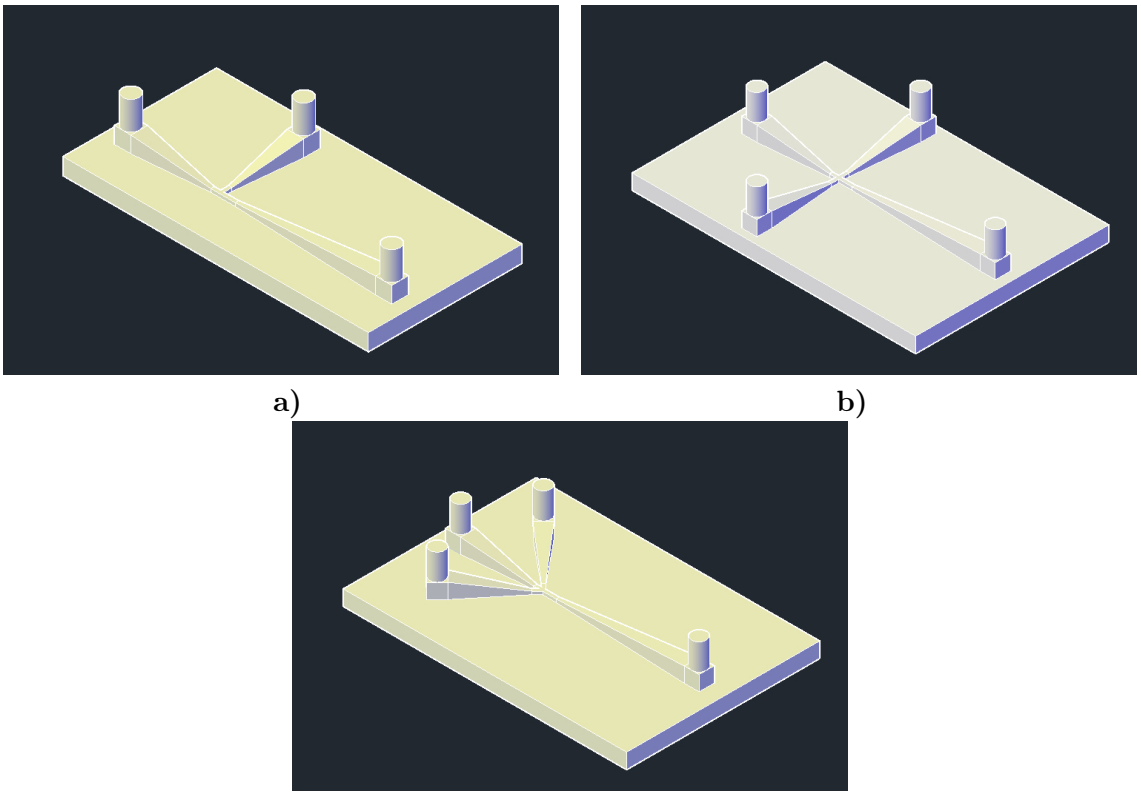

Figure 4.3. Screenshot of AutoCAD. Designs of the channels of the microchip, to be used as a negative mold. **a)** T-Junction geometry, **b)** 90º flow-focusing geometry, and **c)** 45º flow-focusing geometry. Units are in micrometres.

Another approach to generating the microchips was to print solid channels on top of a base as shown in figure 4.3. The printings serve as negative molds for a later casting. The dimensions of the channels are the same as stated in section 3.3. The base for all three geometries was 2 mm thick, however, the flow-focusing geometries were 37.99×25.87 mm, while the T-junction was 37.45×18.81 mm ($w \times h$). Additionally, 2 mm diametre, and 5 mm tall cylinders were added to the inlets and outlets, to allow the connection to the pumps.

4.2 Soft Lithography

Several microchips were designed with LayoutEditor and cast using soft lithography in SU-8 resin throughout this project.

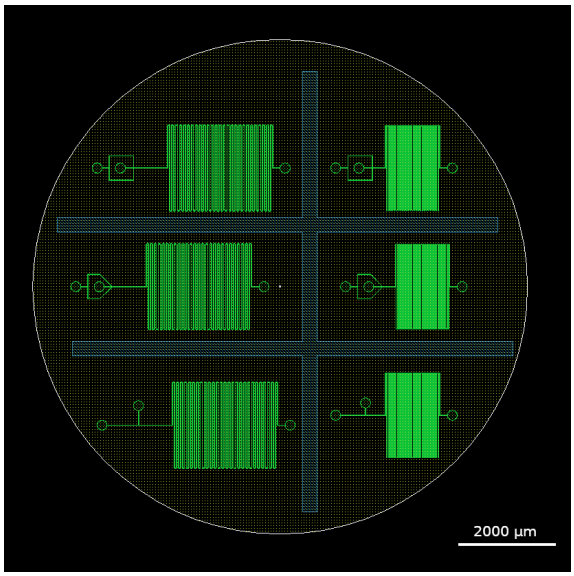

Figure 4.4. Photomasks designed with LayoutEditor. Represented in yellow is the wafer, in green the microfluidic channel, and in blue separation marks. The scale bar is 2000 μm.

In figure 4.4 are shown the photomasks designed. All microfluidic chip photomasks (green), were manufactured together in a 4×4" circular wafer (yellow). Furthermore, separation marks (blue) were also added to be able to separate the different photomasks without damaging any of the microfluidic chips.

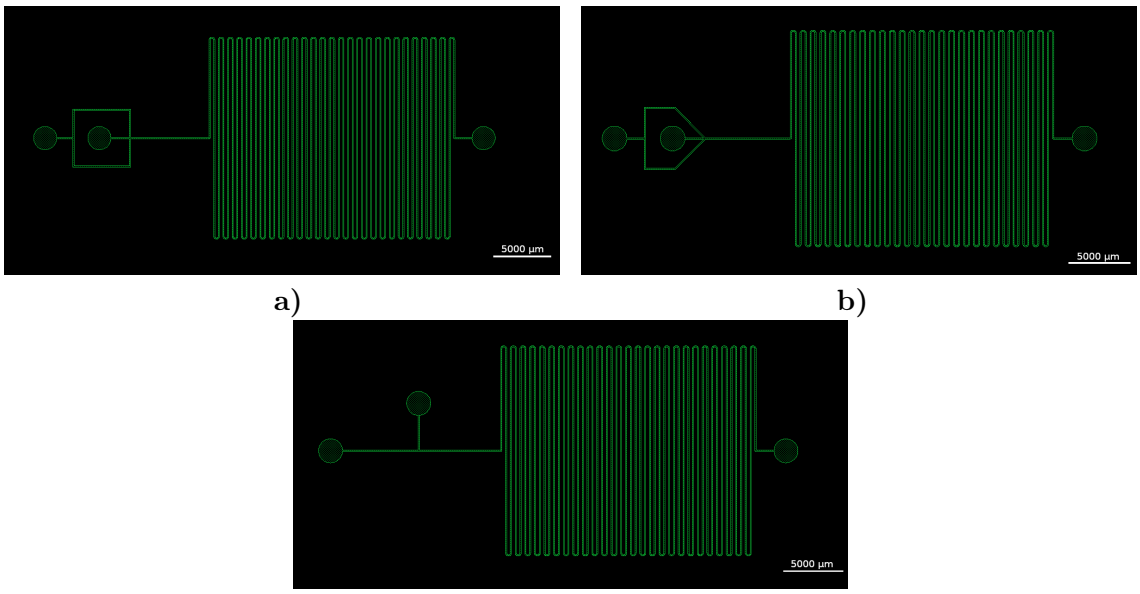

Figure 4.5. Photomasks of microfluidic chips with a minimum element size of 100 μm. **a)** 90º flow-focusing geometry, **b)** 45º flow-focusing geometry, and **c)** T-junction. All scale bars are 5000 μm.

In figure 4.5 the photomasks of the **a)** 90^{o} flow-focusing geometry, **b)** 45^{o} flow-focusing geometry, and **c)** T-junction are shown. The dimensions of the microfluidic chips are 40×17.5 mm ($l \times h$), and channel height of 100 μm. The outlet of the droplet generation junction is connected to a meander. All inlets and outlets have circular cross-section with a 2 mm diameter.

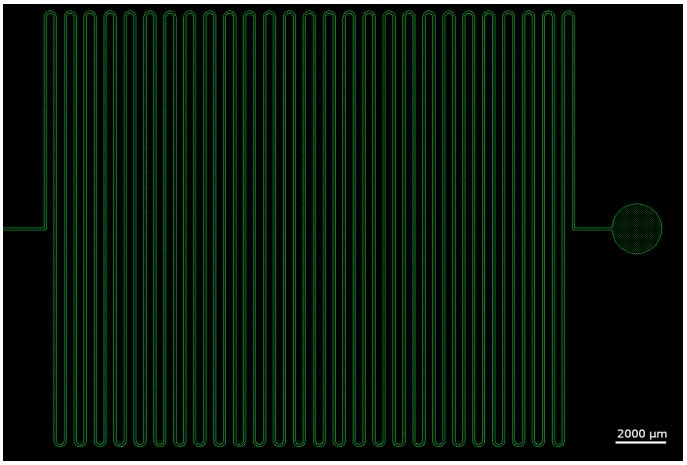

Figure 4.6. Photomask of the meander. The scale bar is 2000 μm

In figure 4.6 the geometry of the meander is shown. The meander is formed by 100 μm in height channels and consists of 2 turns of 8.45 mm long channels, and 52 turns of 17 mm long channels connected through 180^{o} arcs with a 200 μm radius. All channels are separated 300 μm. The length of the meander is approximately 93.42 cm.

4.3 Microfluidic Droplet Generation

This section serves to describe the results obtained regarding the microfluidic chip. Furthermore, this section has been divided into two: the results from the simulations using COMSOL Multiphysics ®, and the experimental results.

4.3.1 Simulations

The simulations performed with the level set physics were carried out to identify the optimal flow velocities for both phases, and therefore, the optimal flow ratio. To save some computational time, the duration of the initial simulations was 0.5 seconds with 0.1 second time-steps, however, after the optimal parameters were found the time-stepping was reduced to 0.01 seconds. The initial investigation also served to identify at which time a steady state of monodisperse droplets was achieved. The parameters used in the initial simulations were based on literature and the parameters determined in earlier studies by Djernæs *et al.* and Úbeda *et al.* for microfluidic droplet generation with different geometry. [173], [174].

3D printing Geometries

The first simulations were carried out by trial error, using Capillary numbers Ca 0.1 and 0.2, as according to literature it results in the dripping regime and therefore would yield a

steady-state of monodispersed droplets. [112]

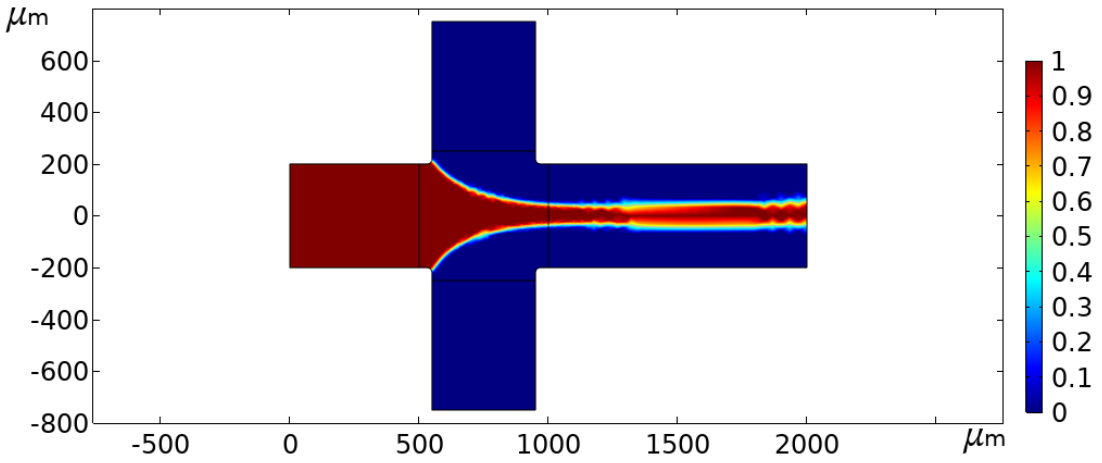

Figure 4.7. Screenshot of COMSOL. Droplet simulation with a Ca 0.2 and R_f 0.2. The scale bar indicates the level set function, where 0 represents the continuous phase and 1 the dispersed phase.

Simulations with Ca 0.2 and R_f 0.2 did not yield droplets but a jetting regime as shown in figure 4.7. The oil-phase (u_c) and dispersed-phase (u_d) were 68.017 mm/s and 13.603 mm/s respectively.

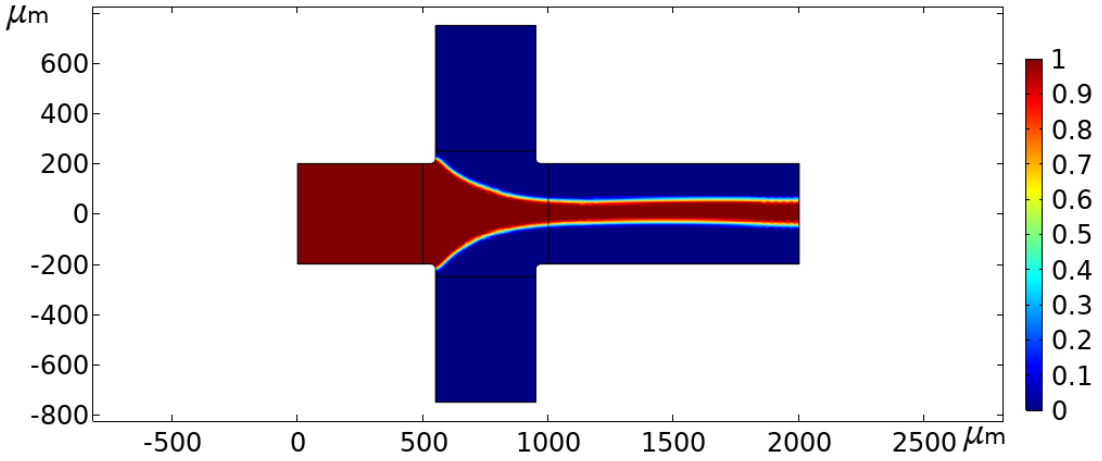

Figure 4.8. Screenshot of COMSOL. Droplet simulation with a Ca 0.1 and R_f 0.1. The scale bar indicates the level set function, where 0 represents the continuous phase and 1 the dispersed phase.

To obtain droplets both Ca and R_f were reduced to 0.1 in the simulation shown in figure 4.8. However, as can be seen, a jetting regime was achieved and no droplets were generated. In the simulation u_c was 34.009 mm/s and u_d was 3.409 mm/s.

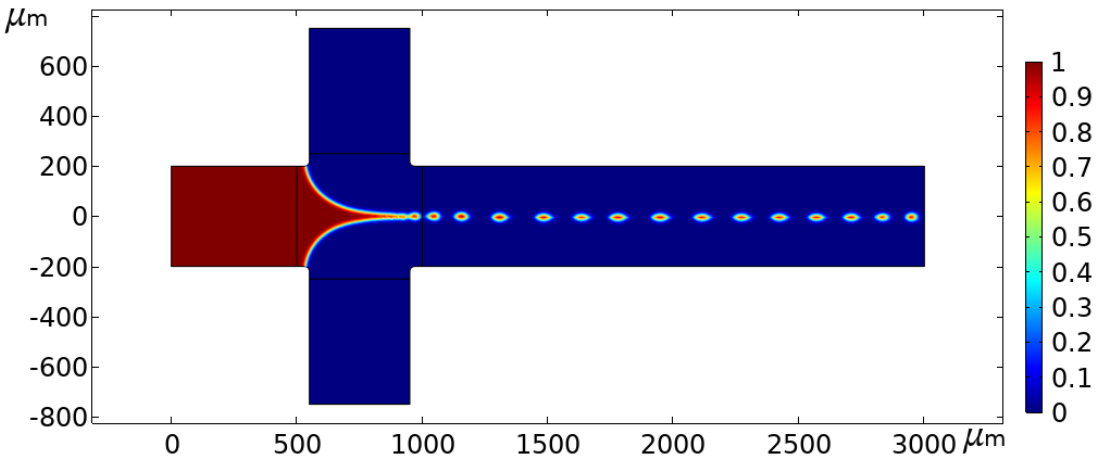

Figure 4.9. Screenshot of COMSOL. Droplet simulation with a Ca 0.1 and R_f 0.06. The scale bar indicates the level set function, where 0 represents the continuous phase and 1 the dispersed phase

The simulation shown in figure 4.9 was carried out with Ca 0.1 and reducing R_f from 0.1 to 0.06. As can be seen, u_c 34.009 mm/s and u_d 2.0405 mm/s yielded droplets.

Additional simulations were carried out to test how the Ca and R_f values, which are related to the continuous-phase and dispersed-phase velocities respectively, affected the droplet size. The time-stepping of the simulations was also reduced to 0.01 seconds to study when the steady-state was achieved.

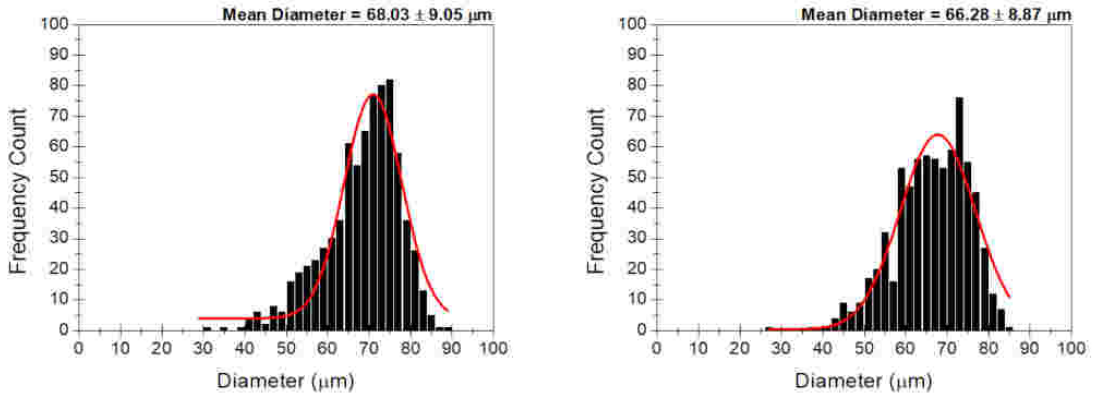

a) **b)**

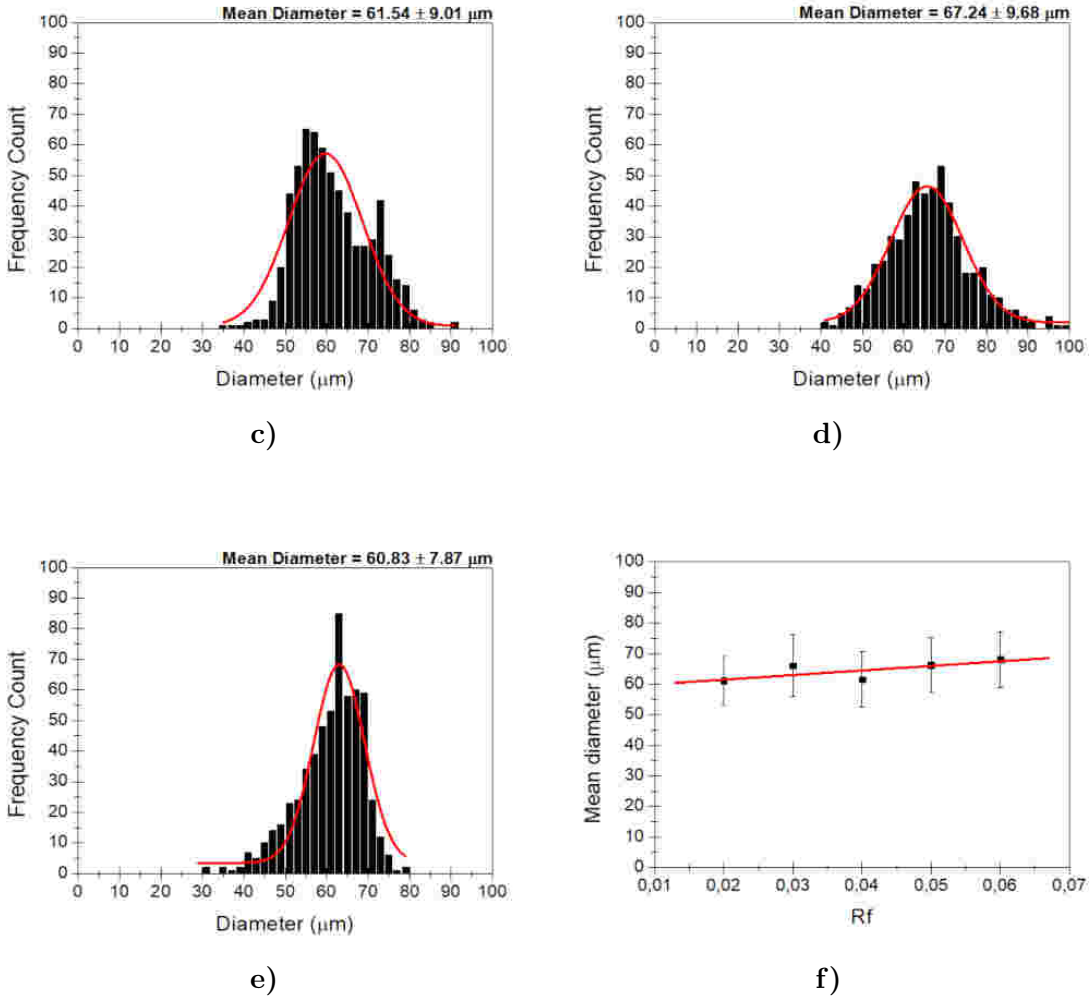

Figure 4.10. Histogram size distribution of the droplet's mean diameter generated with the 90º flow-focusing geometry with Ca 0.1 and modifying the R_f. **a)** R_f 0.06, **b)** R_f 0.05, **c)** R_f 0.04, **d)** R_f 0.03, and **e)** R_f 0.02. In black is represented the frequency count, and in red a Gaussian fit. In **f)** is represented the size trend of droplets' diameter from figures **a)** to **e)**.

In figure 4.10 are shown the size distribution of the generated droplets with a constant continuous-phase velocity of 34.009 mm/s. In figure 4.10 **d)** it can be observed that by reducing the R_f value, and therefore, the dispersed-phase velocity, the general trend is a slight decrease in the droplets' size. However, as shown in table 4.1 the decrease in the R_f entails an increase in polydispersity index (PdI), and the time required to reach the steady-state. Furthermore, for R_f values of 0.03, and 0.02 the simulations showed a discontinuity in the formation of droplets.

The simulations were carried out with higher values of Ca, and consequently higher continuous-phase velocity, did not yield droplet formation.

R_f	u_d [mm/s]	steady-state [ms]	$\overline{\varnothing}$ [μm]	Counts	PdI
0.06	2.0405	21	68.03 ± 9.05	760	∼0.102
0.05	1.7004	21	66.28 ± 8.87	721	∼0.137
0.04	1.3603	26	61.54 ± 9.01	651	∼0.145
0.03	1.0203	31	67.24 ± 9.68	545	∼0.129
0.02	0.6802	44	60.83 ± 7.87	587	∼0.101

Table 4.1. Summary of the simulations carried out with constant Ca and modifying the R_f. u_d refers to the dispersed-phase velocity, steady-state refers to the time when droplets start to be generated.

The PdI of the generated droplets has been calculated according to equation 4.1, where σ is the standard deviation of a monomodal Gaussian fit, and $\overline{\varnothing}$ is the mean diameter. The σ values were automatically generated by OriginPro for the nonlinear gaussian fit.

$$PdI = \frac{\sigma}{\overline{\varnothing}} \tag{4.1}$$

To study if the geometry of the microfluidic chips affects the formation of droplets, the first simulation of the 45º flow-focusing geometry was carried out with the parameters previously found for the 90º geometry.

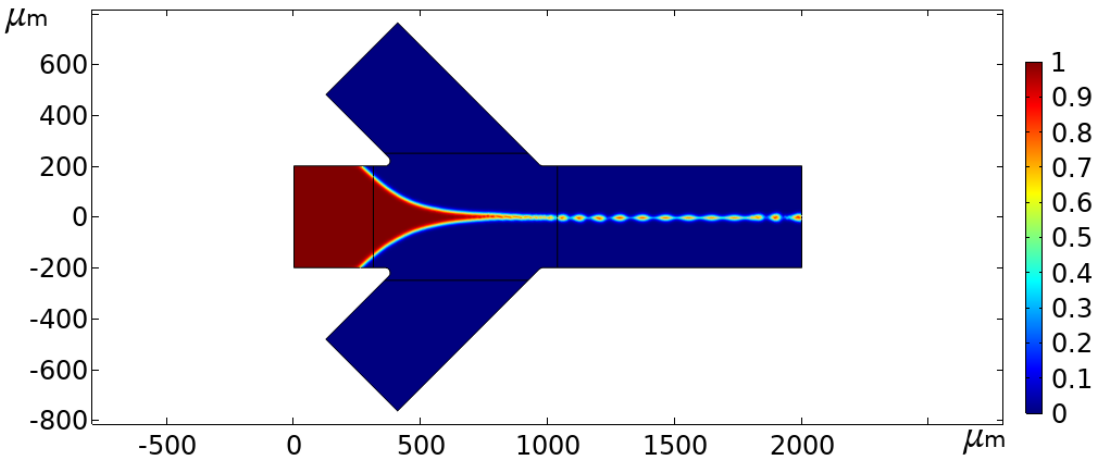

Figure 4.11. Screenshot of COMSOL. Droplet simulation with a Ca 0.1 and R_f 0.06. The scale bar indicates the level set function, where 0 represents the continuous phase and 1 the dispersed phase

The first simulation was carried out with Ca and R_f values of 0.1 and 0.06 respectively, and is shown in figure 4.11. It can be observed that even though the system reaches the formation of droplets they are still attached to each other as there is not a complete break-off.

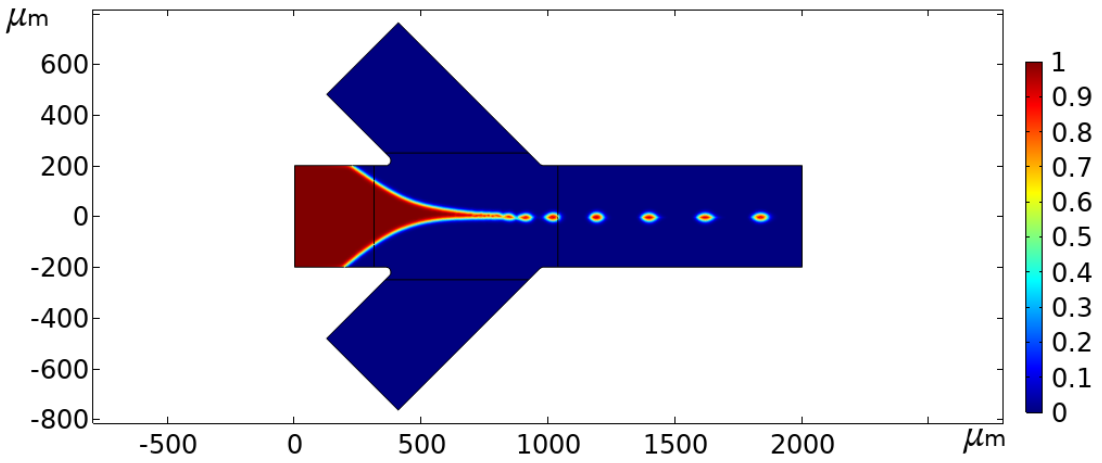

Figure 4.12. Screenshot of COMSOL. Droplet simulation with a Ca 0.1 and R_f 0.04. The scale bar indicates the level set function, where 0 represents the continuous phase and 1 the dispersed phase.

To promote the complete break-off and separation of the droplets, a simulation reducing the R_f value to 0.04 was performed. It can be observed in figure 4.12 that by reducing the flow rate ratio and therefore, the dispersed-phase velocity, the system yields a steady-state of droplets. The droplets were formed with u_c 34.009 mm/s and u_d 1.3603 mm/s.

Additional simulations were carried out to test the Ca and R_f values, which are related to the continuous-phase and dispersed-phase velocities respectively, which affected the droplet size. Furthermore, the time-stepping of the simulations was reduced to 0.01 seconds to study when the steady-state is achieved.

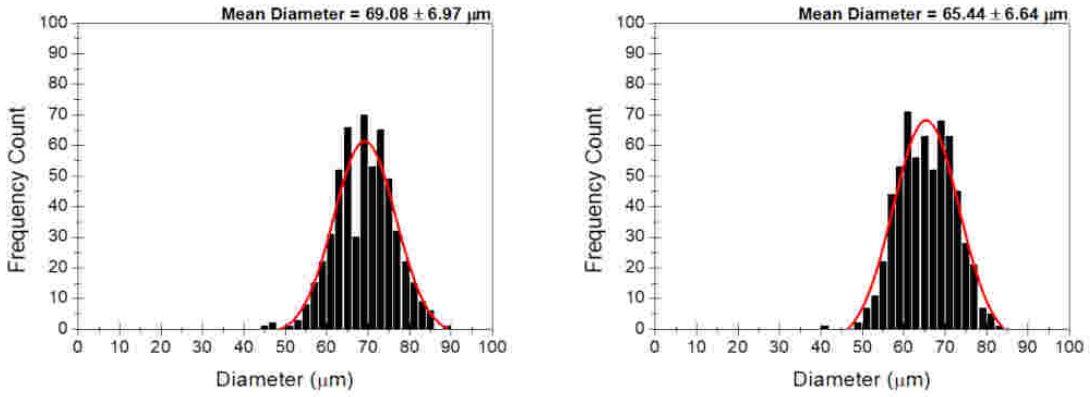

a) **b)**

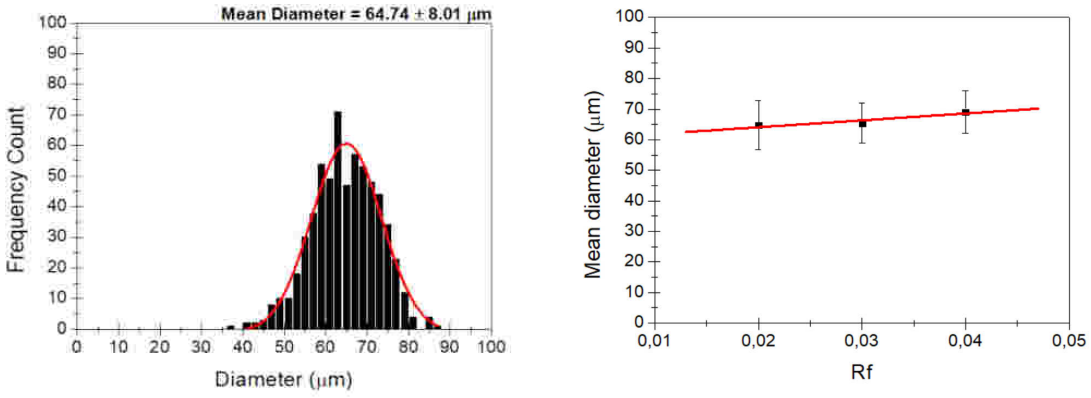

c) **d)**

Figure 4.13. Histogram size distribution of the droplet's mean diameter generated with the 45º flow-focusing geometry with Ca 0.1 and modifying the R_f. **a)** R_f 0.04, **b)** R_f 0.03, and **c)** R_f 0.02. In black is represented the frequency count, and in red a Gaussian fit. In **d)** is represented the size trend of droplets' diameter from figures **a)** to **c)**.

In figure 4.13 are shown the size distribution of the generated droplets with a constant continuous-phase velocity of 34.009 mm/s. In figure 4.13 **d)** it can be observed that by reducing the R_f value, and therefore, the dispersed-phase velocity, the general trend is a slight decrease in the droplets' size. However, as shown in table 4.2 the decrease in the R_f entails an increase in the time required to reach the steady-state. Furthermore, for R_f values smaller than 0.02 the steady-state is not achieved as there is not enough build-up pressure leading to the break-off of droplets.

R_f	u_d **[mm/s]**	**steady-state [ms]**	$\overline{\varnothing}$ **[μm]**	**Counts**	**PdI**
0.04	1.3603	31	69.08 ± 6.97	553	∼0.108
0.03	1.0203	44	65.44 ± 6.64	620	∼0.121
0.02	0.6802	61	67.74 ± 8.01	623	∼0.125

Table 4.2. Summary of the simulations carried out with constant Ca and modifying the R_f. u_d refers to the dispersed-phase velocity, steady-state refers to the time when droplets start to be generated.

Similar to the first simulation carried out in the 45º geometry, to study if the geometry of the microfluidic chips affects the formation of droplets, the first simulation of the T-junction geometry was carried out with the parameters previously found for both 90º and 45º flow-focusing geometries. However, any of the simulations yielded the formation of droplets but instead a jetting regime attached to the upper wall. To try to overcome that, the contact angle was increased to 180° yet no droplets were formed.

Soft-lithography Geometries

The first simulations were carried out by trial error, using Capillary numbers Ca 0.1 and 0.2, as according to literature it results in the dripping regime, and therefore would yield a steady-state of monodispersed droplets. [112]

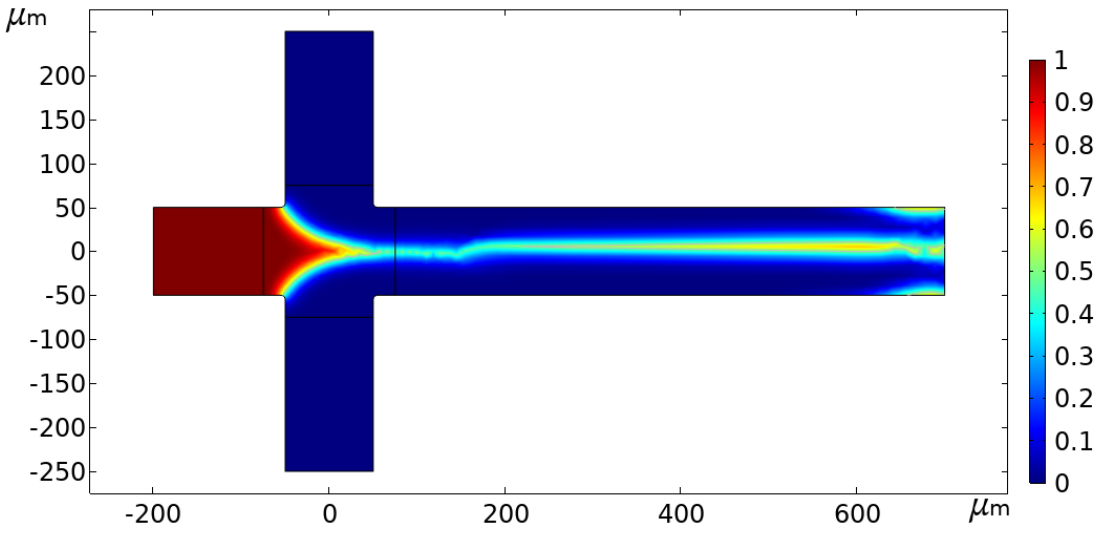

Figure 4.14. Screenshot of COMSOL. Droplet simulation with a Ca 0.1 and R_f 0.1. The scale bar indicates the level set function, where 0 represents the continuous phase and 1 the dispersed phase

As can be seen in figure 4.14 a jetting regime was achieved, but a steady-state of monodispersed droplet generation is not achieved. The parameters used in this simulation were Ca 0.1, flow ratio (R_f) 0.1, and oil-phase (u_c) and dispersed-phase velocities (u_d) of 34.009 mm/s and 3.4009 mm/s respectively.

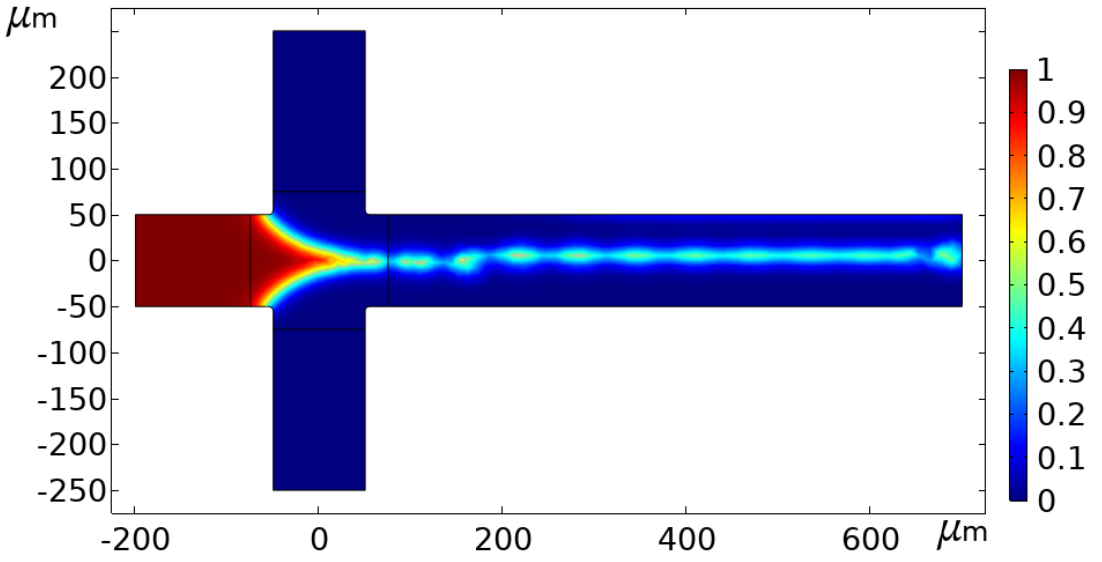

Figure 4.15. Screenshot of COMSOL. Droplet simulation with Ca 0.07 and R_f 0.25. The scale bar indicates the level set function, where 0 represents the continuous phase and 1 the dispersed phase.

With u_c 23.8069 mm/s and u_d 5.9515 mm/s in figure 4.15, it is evident that the droplets do not experience a complete breakup yielding a regime between dripping and jetting.

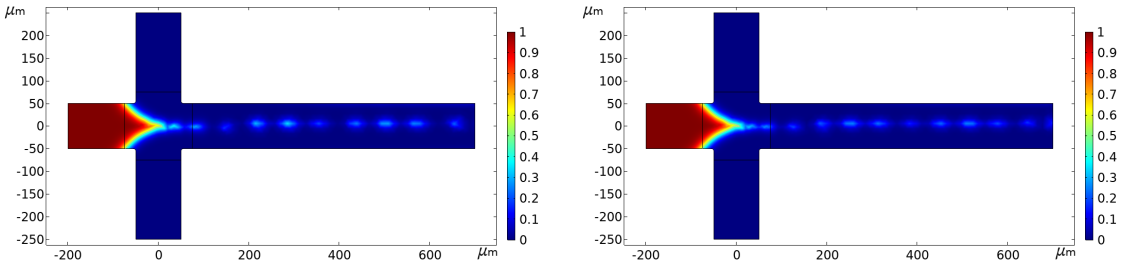

Figure 4.16. Screenshot of COMSOL. Droplet simulation with R_f 0.0625 and **a)** Ca 0.06, and **b)** Ca 0.07. The scale bar indicates the level set function, where 0 represents the continuous phase and 1 is the dispersed phase.

When the flow ratio is reduced to 0.0625, for Ca values of **a)** 0.06 and **b)** 0.07, it is evident that the droplets experience a break-up yielding a steady-state of monodispersed droplets as can be seen in figure 4.16. The continuous-phase and dispersed-phase velocities were calculated from Ca and R_f according to equation 4.2 and equation 4.3 respectively. Figure 4.16 **a)** had u_c=23.8069 mm/s and u_d=1.4879 mm/s, and figure 4.16 **b)** had u_c=20.4052 mm/s and u_d=1.2753 mm/s.

$$u_c = \frac{Ca \times \sigma}{\mu_c} \tag{4.2}$$

$$u_d = R_f \times u_c \tag{4.3}$$

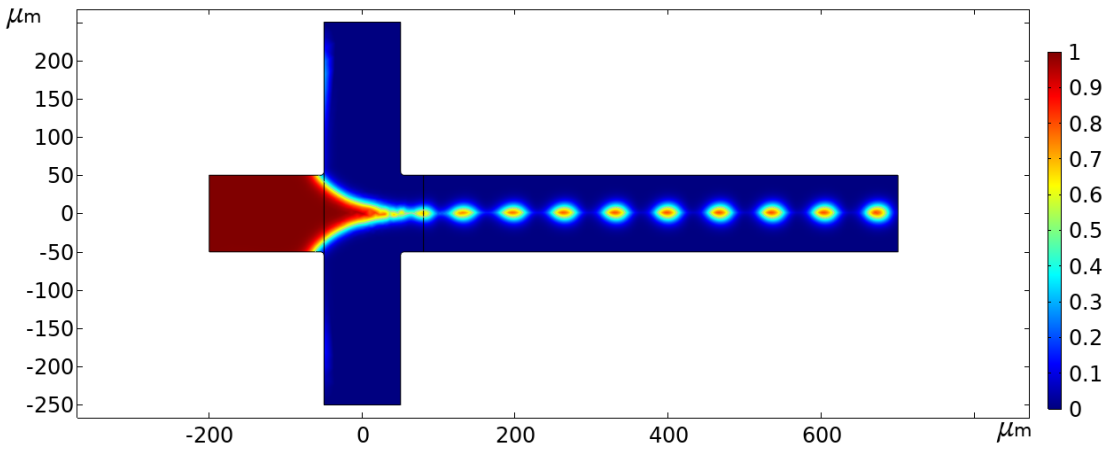

Figure 4.17. Screenshot of COMSOL. Droplet simulation with Ca 0.05, and R_f 0.2. The scale bar indicates the level set function, where 0 represents the continuous phase and 1 the dispersed phase.

A dripping regime was achieved for values of Ca 0.05 and R_f 0.2 as can be seen in figure 4.17. In this simulation the velocities for the oil-phase and dispersed-phase were 17.004 mm/s and 3.4009 mm/s respectively.

A parametric sweep was performed on the microchip to study how different values of Ca and R_f, related to the continuous-phase and dispersed-phase velocities respectively, affected the droplet size. The simulated Ca values were from 0.03 to 0.08, and the R_f values from 0.08 to 0.2. The simulations were 0.5 seconds long with a time-stepping of 0.01 seconds.

First, a parametric sweep of flow rate ratios with Ca 0.03 was carried out. In figure 4.18 is shown the evolution of the size of the droplets as a function of R_f and constant u_c of 10.203 mm/s. As can be observed in the graph above the general trend is an increase in the mean diameter with the decrease in R_f. Additionally, the standard deviation for R_f values of 0.12 to 0.18 increases drastically due to the existence of two different size populations, one between 20-50 μm, and the other above 70 μm as shown in figure 4.18

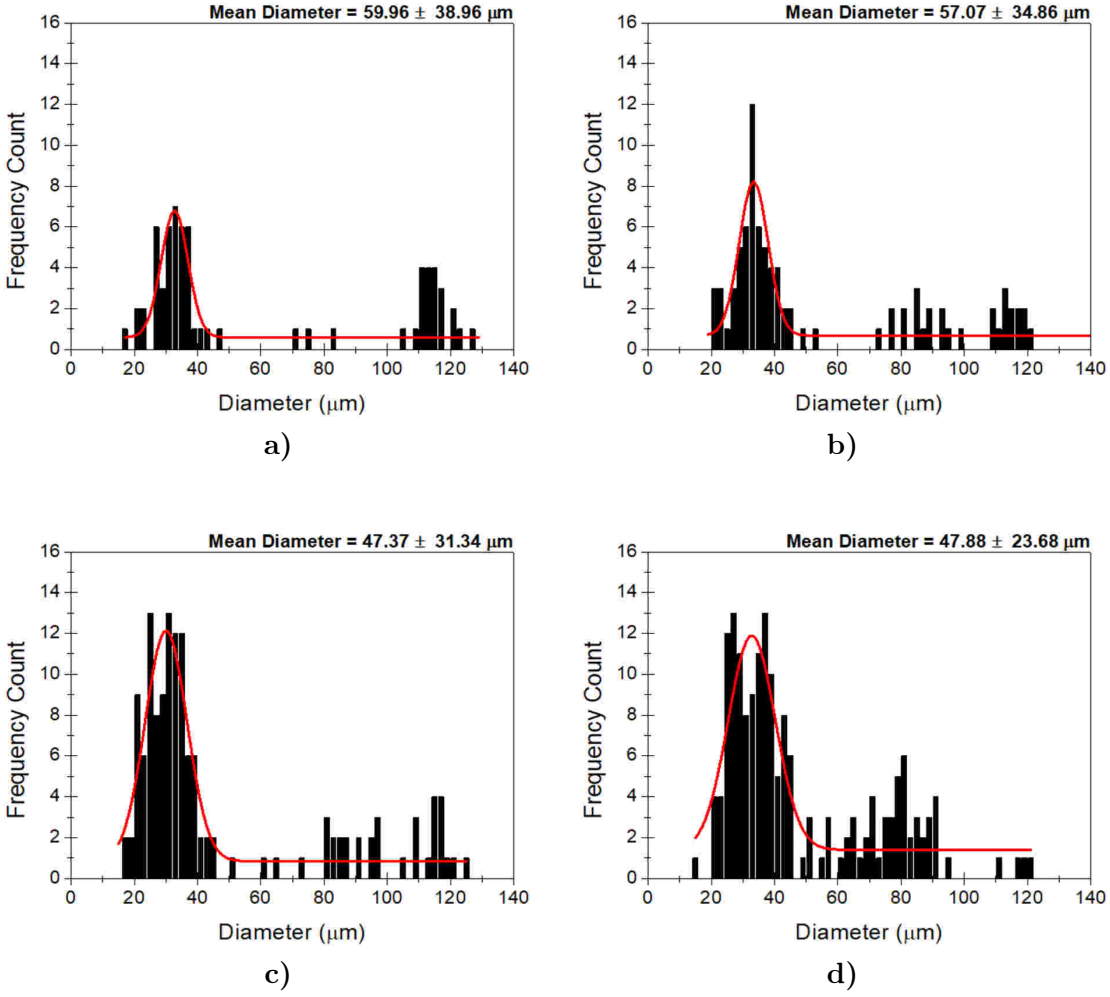

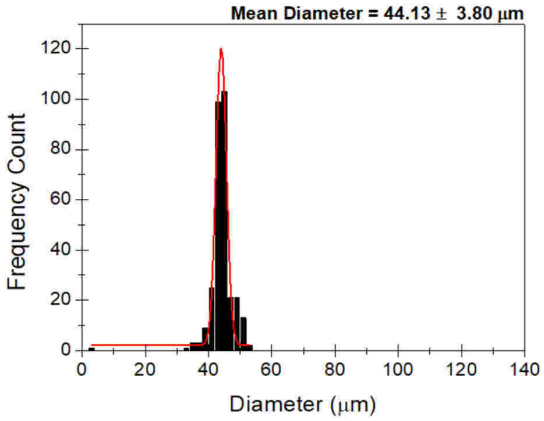

e)

Figure 4.18. Droplet size distribution for Ca 0.03 and varying R_f. **a)** R_f 0.12, **b)** R_f 0.14, **c)** R_f 0.16, **d)** R_f 0.18, and **e)** R_f 0.2.

In figure 4.18 can be seen two different size populations, one with the mean size of around 35 μm, and the other with diameters above 70 μm. It can be observed that the number of droplets and the population with a mean diameter around 35 μm increase with the R_f. In figure 4.18 **e)** it is shown that for Ca 0.2 there is only one population of droplets with a mean size of 44.13 ± 3.8 μm.

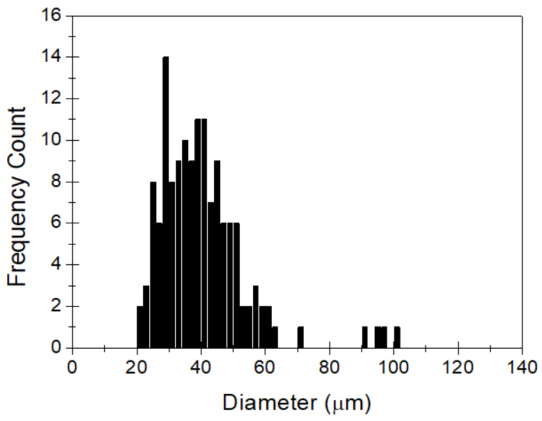

a)

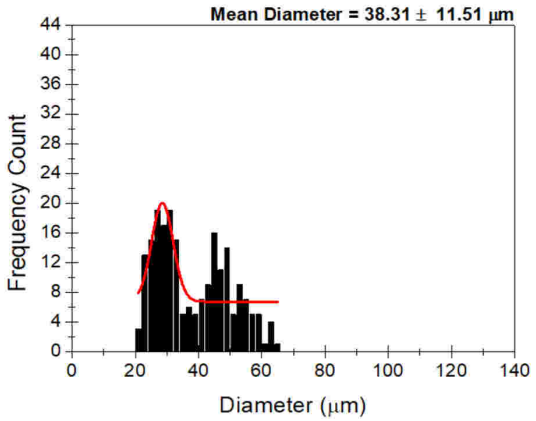

b)

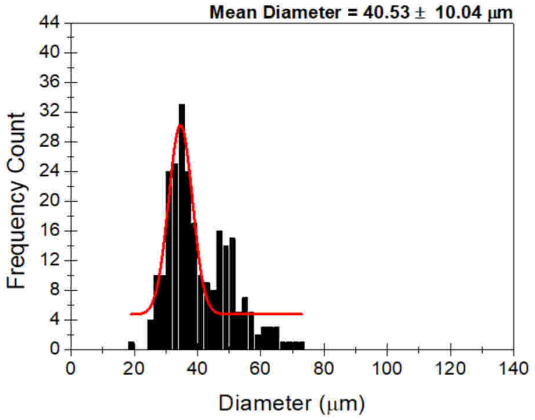

c)

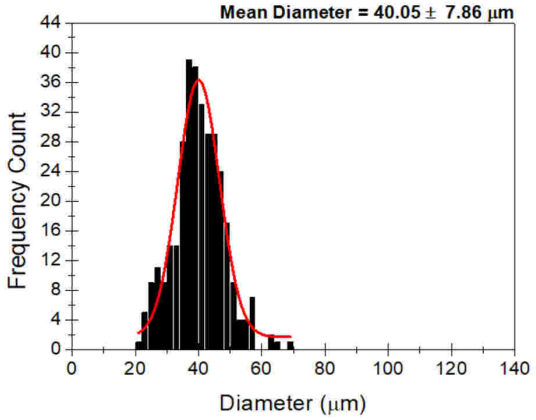

d)

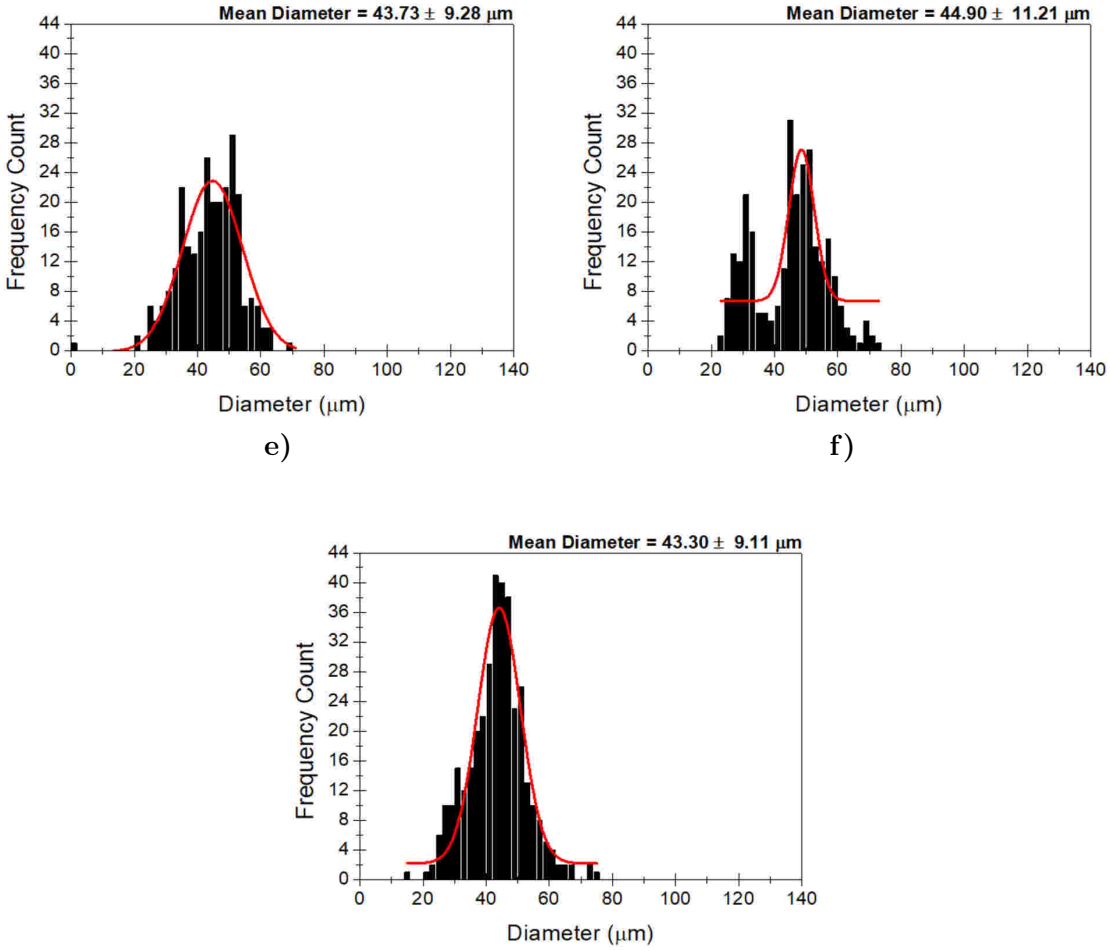

Figure 4.19. Droplet size distribution for Ca 0.04 and varying R_f. **a)** R_f 0.08, **b)** R_f 0.1, **c)** R_f 0.12, **d)** R_f 0.14, **e)** R_f 0.16, **f)** 0.18, and **g)** 0.2.

In figure 4.19 can be seen that for Ca 0.04 the droplet size distribution becomes narrower with the increase of R_f. However, for R_f values of 0.1, 0.12, and 0.18 two size populations of droplets can be distinguished. For Ca 0.04 the smallest droplets have been obtained with R_f 0.1 with a mean size of 38.31 $\pm$ 11.51 μm, with continuous and dispersed phase velocities of 13.603 and 1.3603 mm/s respectively.

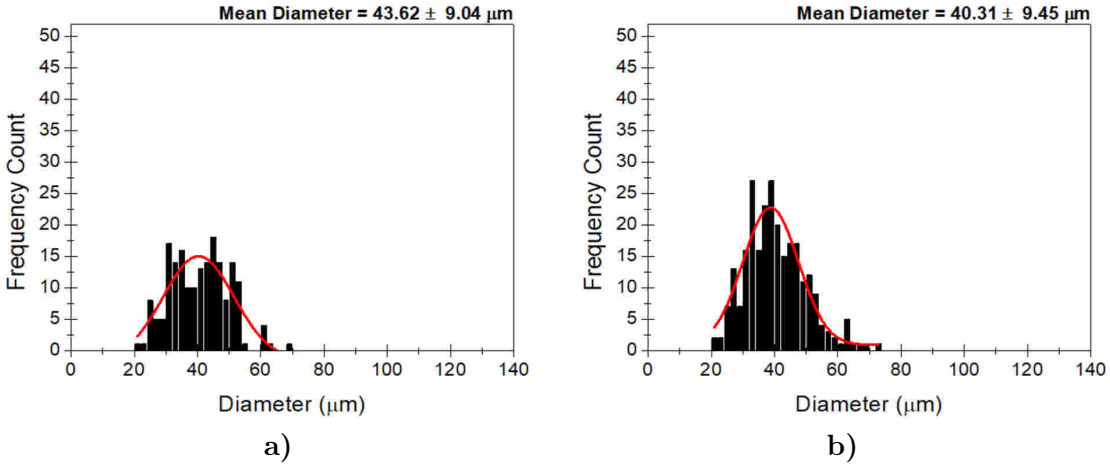

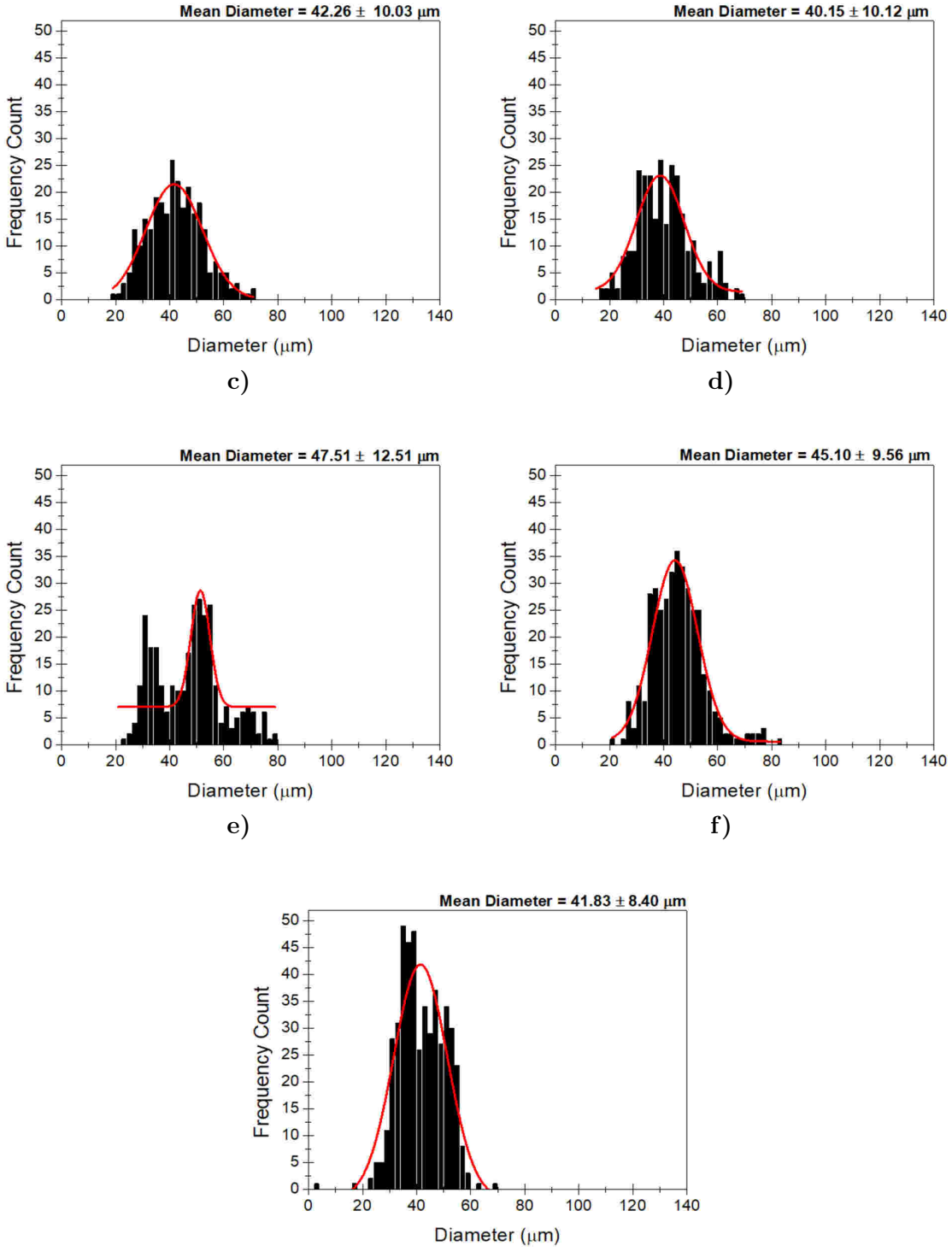

Figure 4.20. Droplet size distribution for Ca 0.05 and varying R_f. **a)** R_f 0.08, **b)** R_f 0.1, **c)** R_f 0.12, **d)** R_f 0.14, **e)** R_f 0.16, **f)** 0.18, and **g)** 0.2.

In figure 4.20 can be seen that similar to Ca 0.04, for Ca 0.05 the droplet size distribution also becomes narrower with the increase of R_f. Additionally, it can be observed that the number of droplets also increases altogether with R_f. However, for R_f 0.16 two size populations of droplets can be distinguished. For Ca 0.05 the smallest droplets have been obtained with R_f 0.1 with a mean size of 40.31 ± 9.45 μm, with continuous and dispersed phase velocities of 17.004 and 1.7004 mm/s respectively.

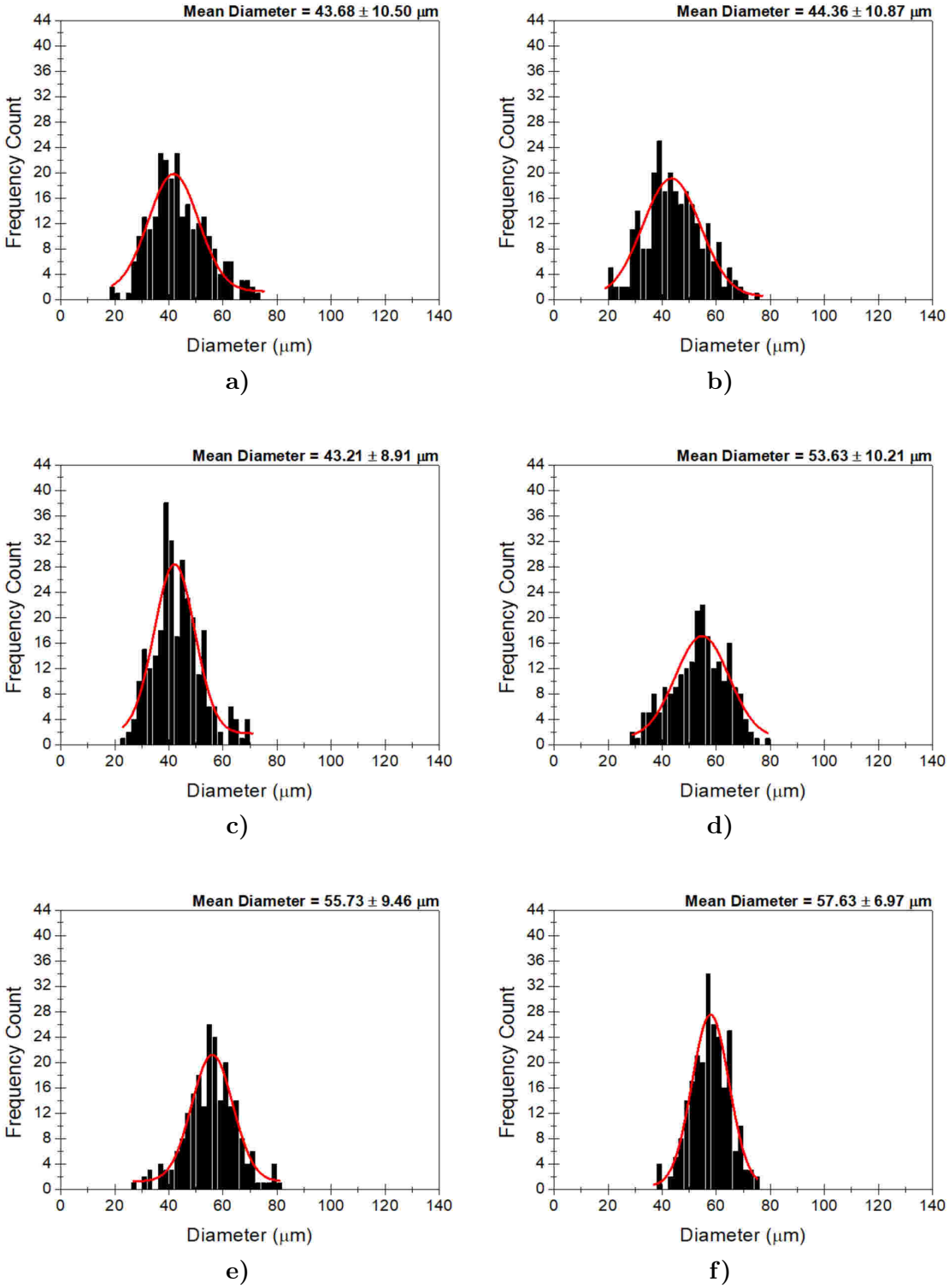

Figure 4.21. Droplet size distribution for Ca 0.06 and varying R_f. **a)** R_f 0.08, **b)** R_f 0.1, **c)** R_f 0.12, **d)** R_f 0.14, **e)** R_f 0.16, and **f)** 0.18.

A similar behaviour can be seen in figure 4.21 for Ca 0.06, where the droplet size distribution is broader for small values of R_f and becomes broader with the increase of the dispersed phase velocity. However, for Ca 0.05 the size distribution is not divided into different populations unlike for Ca 0.03 and 0.04. For Ca 0.05 the smallest droplets have been obtained with R_f 0.12 with a mean size of 43.21 $\pm$ 8.91 μm, with continuous and dispersed phase velocities of 20.405 and 2.449 mm/s respectively.

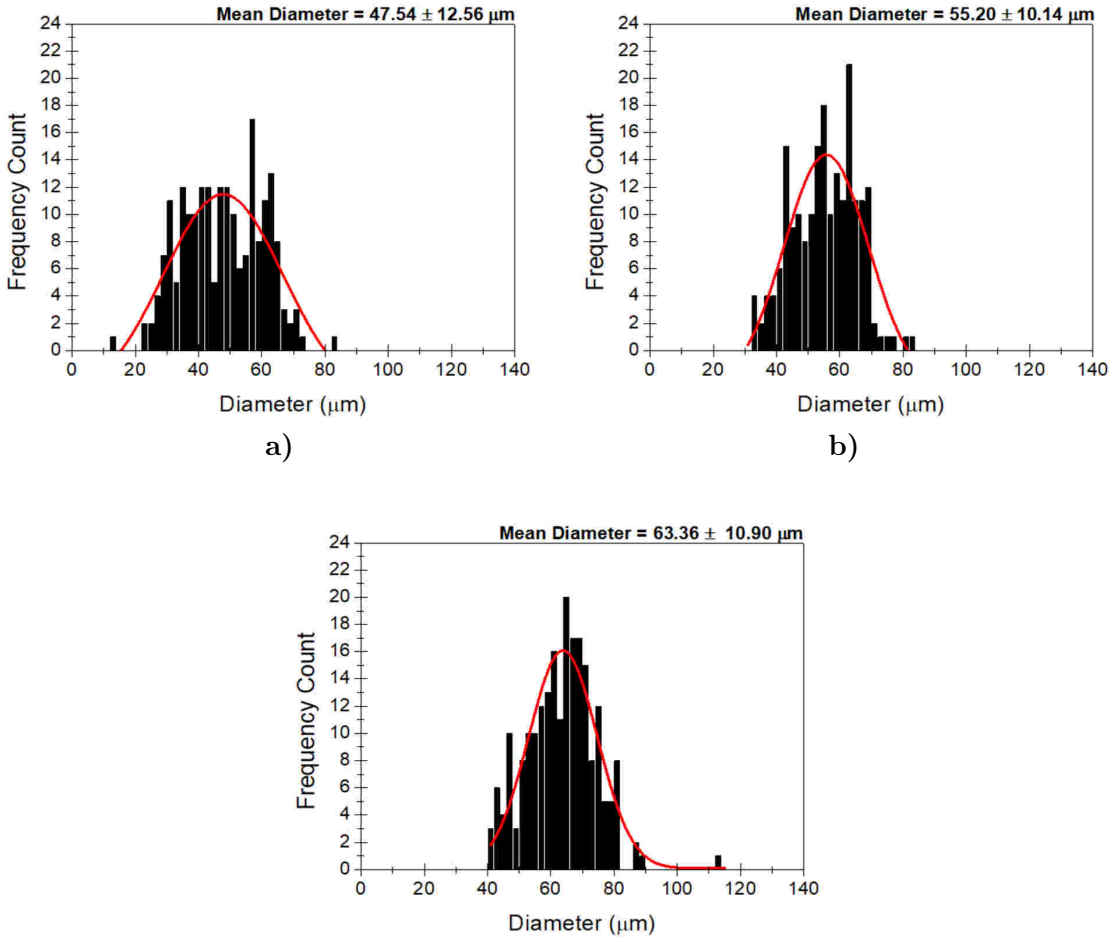

Figure 4.22. Droplet size distribution for Ca 0.07 and varying R_f. **a)** R_f 0.08, **b)** R_f 0.1, and **c)** R_f 0.12.

For Ca 0.07 droplets could only be generated with R_f values of 0.08, 0.1, and 0.12 as shown in figure 4.22. For greater R_f values a jetting regime was reached and therefore no droplets were formed. For Ca 0.07 the smallest droplets have been obtained with R_f 0.08 with a mean size of 47.54 ± 12.56 μm, with continuous and dispersed phase velocities 23.806 and 1.904 mm/s respectively.

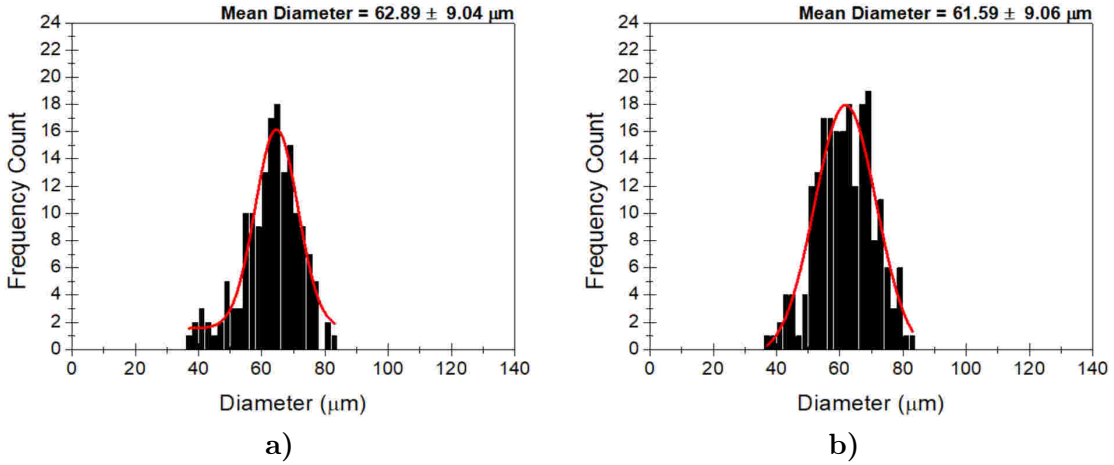

Figure 4.23. Droplet size distribution for Ca 0.08 and varying R_f. **a)** R_f 0.08, **b)** R_f 0.1, and **c)** R_f 0.12.

A similar behaviour can be observed for Ca 0.08, where droplets are only formed with R_f values of 0.08 and 0.1 as shown in figure 4.23. For Ca 0.08 the smallest droplets have been obtained with R_f 0.1 with a mean size of 61.59 $\pm$ 9.06 μm, with continuous and dispersed phase velocities of 27.207 and 2.7207 mm/s respectively.

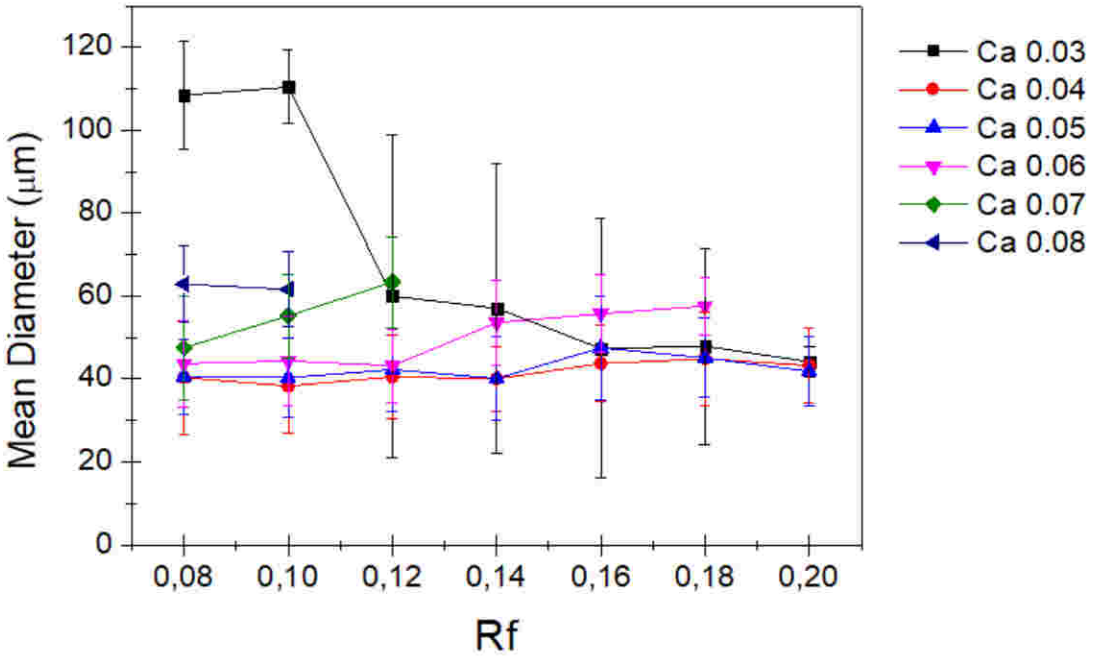

Figure 4.24. Droplet diameter size trend for a constant Ca. In black Ca 0.03, in red Ca 0.04, in blue Ca 0.05, in pink Ca 0.06, in green Ca 0.07, and dark blue Ca 0.08.

Figure 4.24 serves as a summary of the evolution of the droplets' diameter as a function of R_f for constant Ca values. For intermediate Ca values, i.e., 0.04 to 0.06, the general trend is a decrease in the droplet size along with the R_f. Yet, this trend is broken for Ca 0.03 were the droplets' size increases with the decrease in R_f. The trend can not be seen for Ca 0.07 and 0.08 due to the jetting regime achieved.

For the 45° flow-focusing geometry the parameters used for the first simulations were the ones previously found for the 90° flow-focusing simulations.

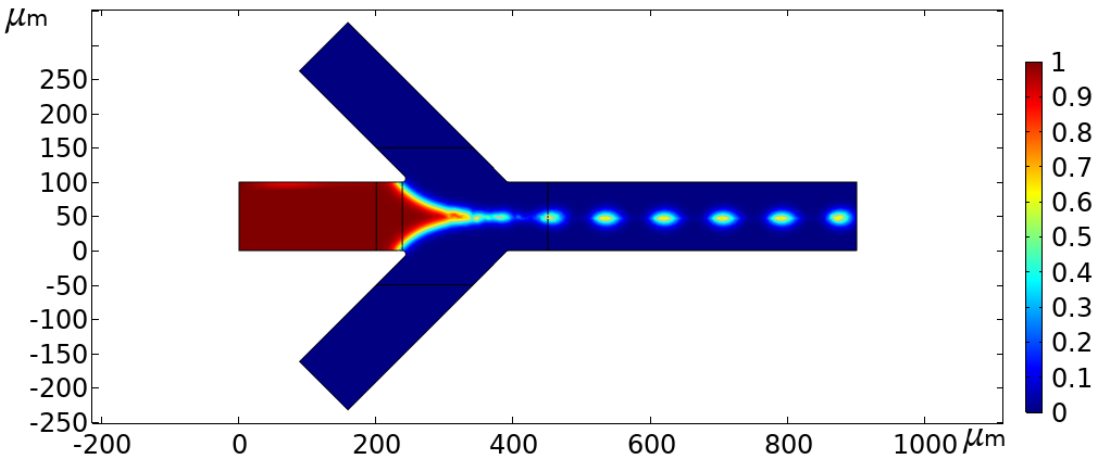

Figure 4.25. Screenshot of COMSOL. Droplet simulation with Ca 0.05, and R_f 0.2. The scale bar indicates the level set function, where 0 represents the continuous phase and 1 the dispersed phase.

The simulation was carried out with Ca 0.05, R_f 0.1, oil-phase velocity 17.004 mm/s, and dispersed-phase velocity of 1.7004 mm/s as can be seen in figure 4.25 yielded a steady-state of droplets.

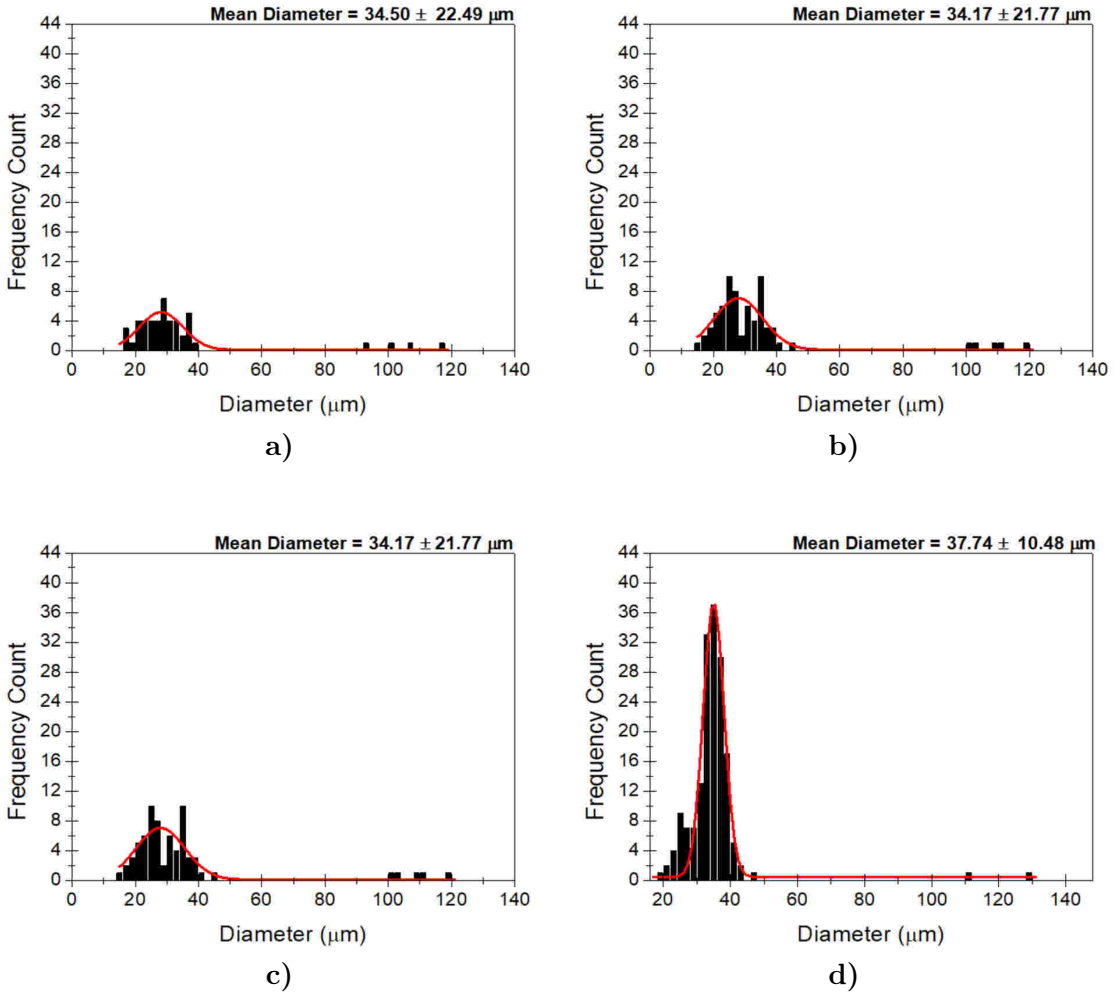

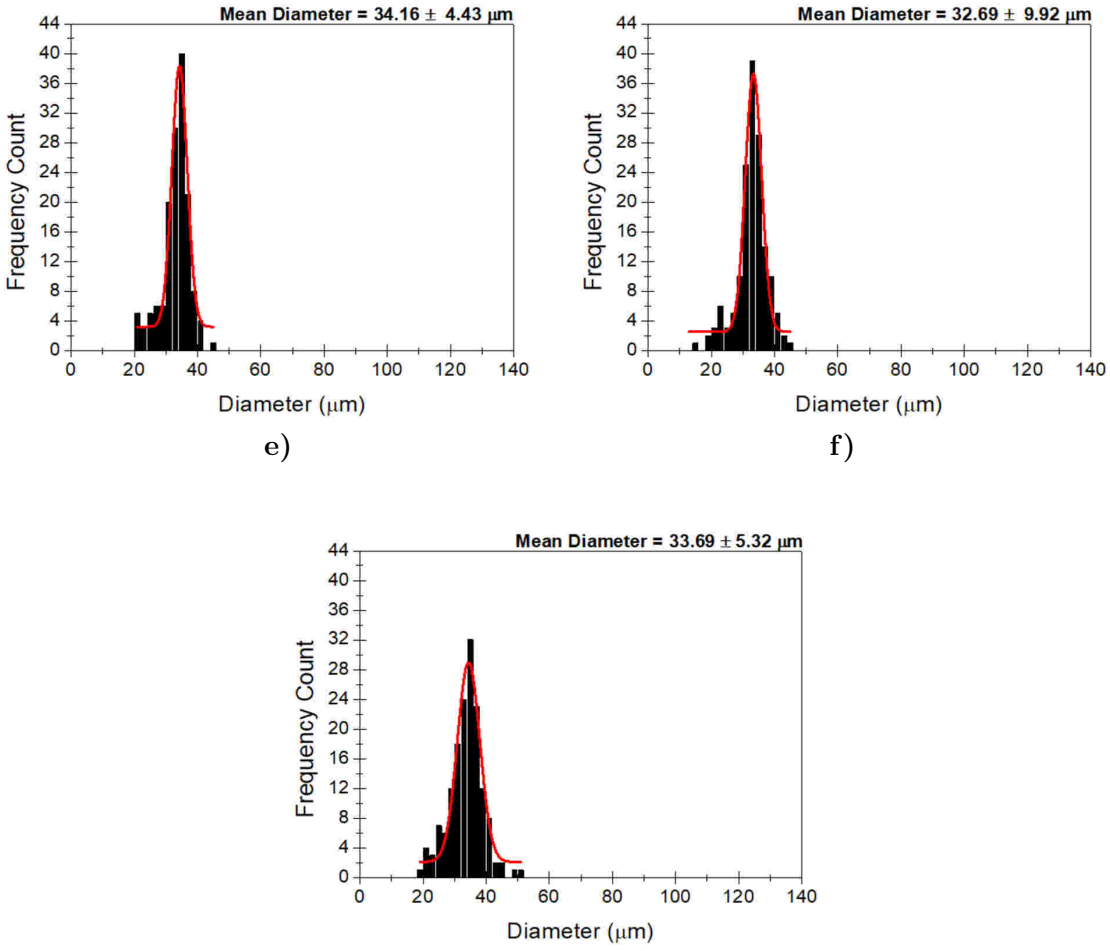

Figure 4.26. Droplet size distribution for Ca 0.03 and varying R_f. **a)** R_f 0.08, **b)** R_f 0.1, **c)** R_f 0.12, **d)** R_f 0.14, **e)** R_f 0.16, **f)** 0.18, and **g)** 0.2.

In figure 4.26 it can be observed that the size distribution of the droplets gets narrower with increasing R_f. Furthermore, it can also be observed that the number of droplets also increases having a frequency count of around 10 for R_f values of 0.08 to 0.12, and up to 30 for R_f values of 0.14 to 0.2. For Ca 0.03 the smallest droplets have been obtained with R_f 0.12 with a mean size of 32.43 $\pm$ 16.68 μm, with continuous and dispersed phase velocities 10.203 and 1.224 mm/s respectively.

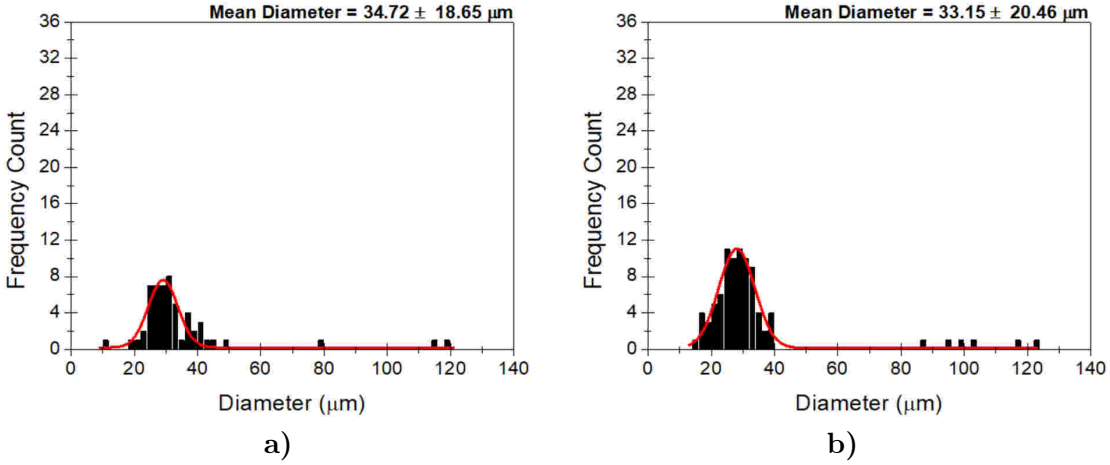

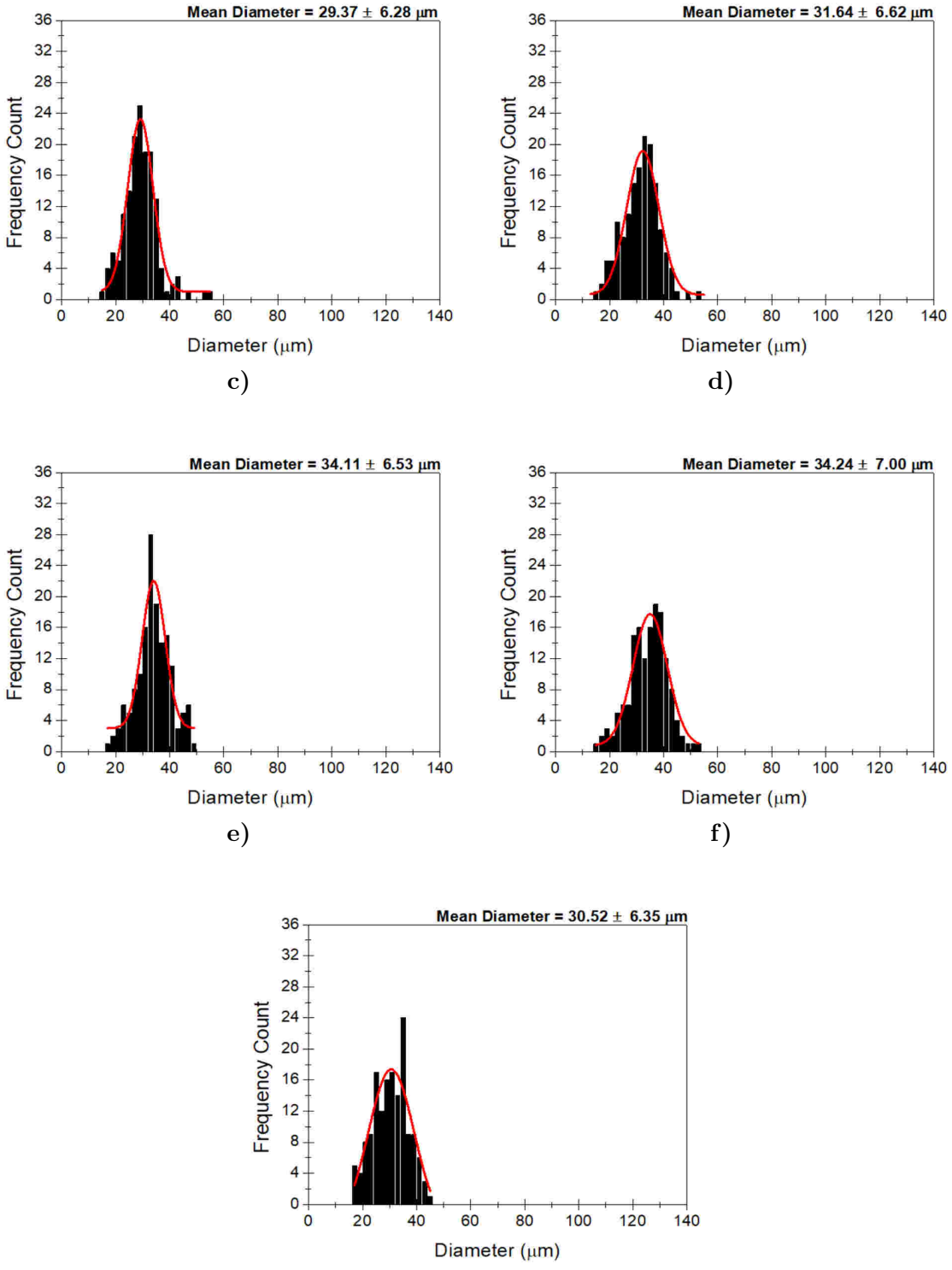

Figure 4.27. Droplet size distribution for Ca 0.04 and varying R_f. **a)** R_f 0.08, **b)** R_f 0.1, **c)** R_f 0.12, **d)** R_f 0.14, **e)** R_f 0.16, **f)** 0.18, and **g)** 0.2.

In figure 4.27 it can be observed that the size distribution of the droplets is broad and has a low frequency count for R_f 0.08 and 0.1, but increases the number of counts and gets narrower for R_f values of 0.12 to 0.2. For Ca 0.04 the smallest droplets have been obtained with R_f 0.12 with a mean size of 29.37 $\pm$ 6.28 μm, with a continuous and dispersed phase velocities of 13.603 and 1.632 mm/s respectively.

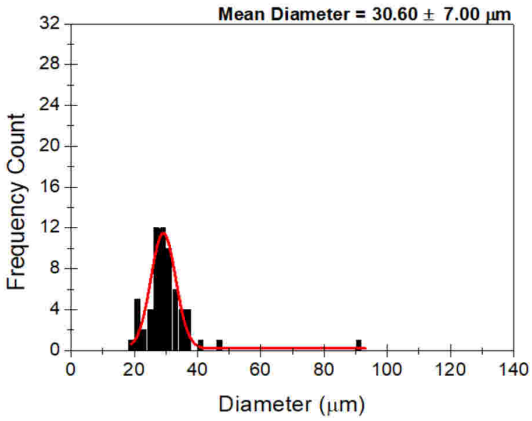
Mean Diameter = 30.60 ± 7.00 µm
Frequency Count
Diameter (µm)

a)

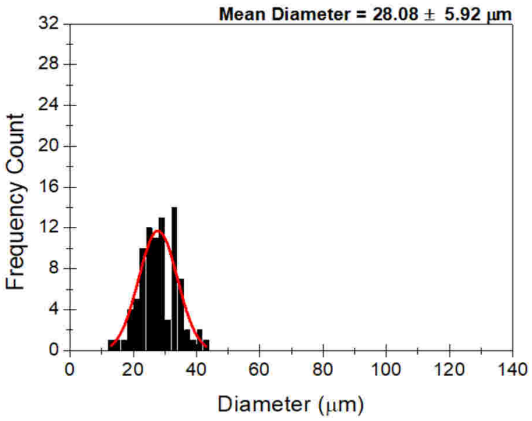
Mean Diameter = 28.08 ± 5.92 µm
Frequency Count
Diameter (µm)

b)

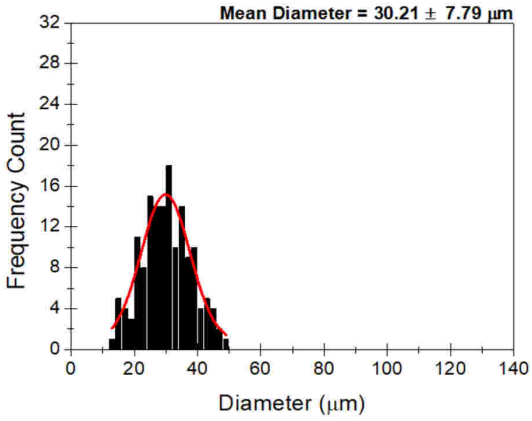
Mean Diameter = 30.21 ± 7.79 µm
Frequency Count
Diameter (µm)

c)

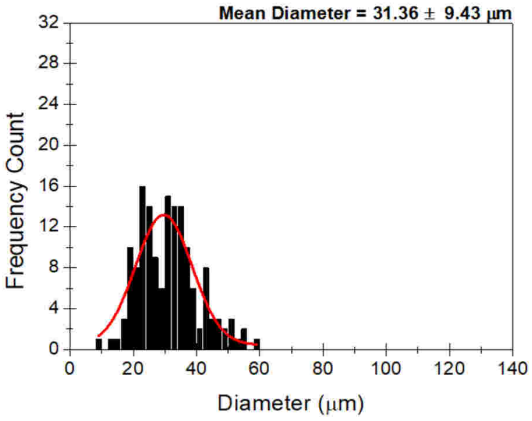
Mean Diameter = 31.36 ± 9.43 µm
Frequency Count
Diameter (µm)

d)

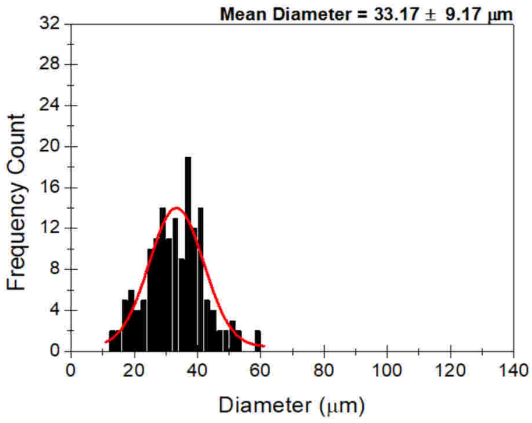
Mean Diameter = 33.17 ± 9.17 µm
Frequency Count
Diameter (µm)

e)

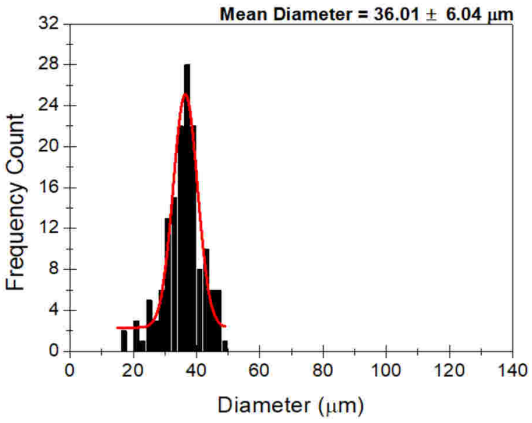
Mean Diameter = 36.01 ± 6.04 µm
Frequency Count
Diameter (µm)

f)

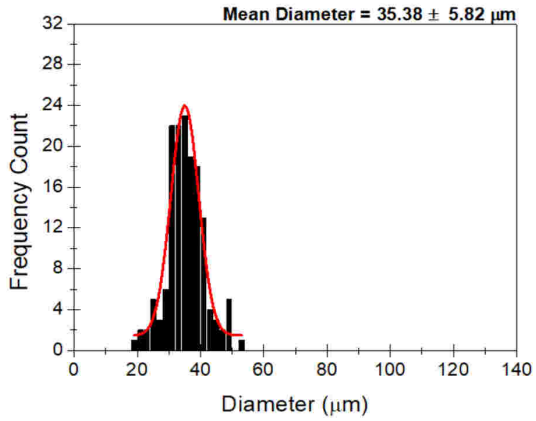

g)

Figure 4.28. Droplet size distribution for Ca 0.05 and varying R_f. **a)** R_f 0.08, **b)** R_f 0.1, **c)** R_f 0.12, **d)** R_f 0.14, **e)** R_f 0.16, **f)** 0.18, and **g)** 0.2.

In figure 4.28 it can be observed that the size distribution of the droplets increases with R_f. Yet, the size distribution decreases again for R_f 0.18 and 0.2. For Ca 0.05 the smallest droplets have been obtained with R_f 0.12 with a mean size of 28.08 ± 5.92 μm, with continuous and dispersed phase velocities of 17.004 and 1.7004 mm/s respectively.

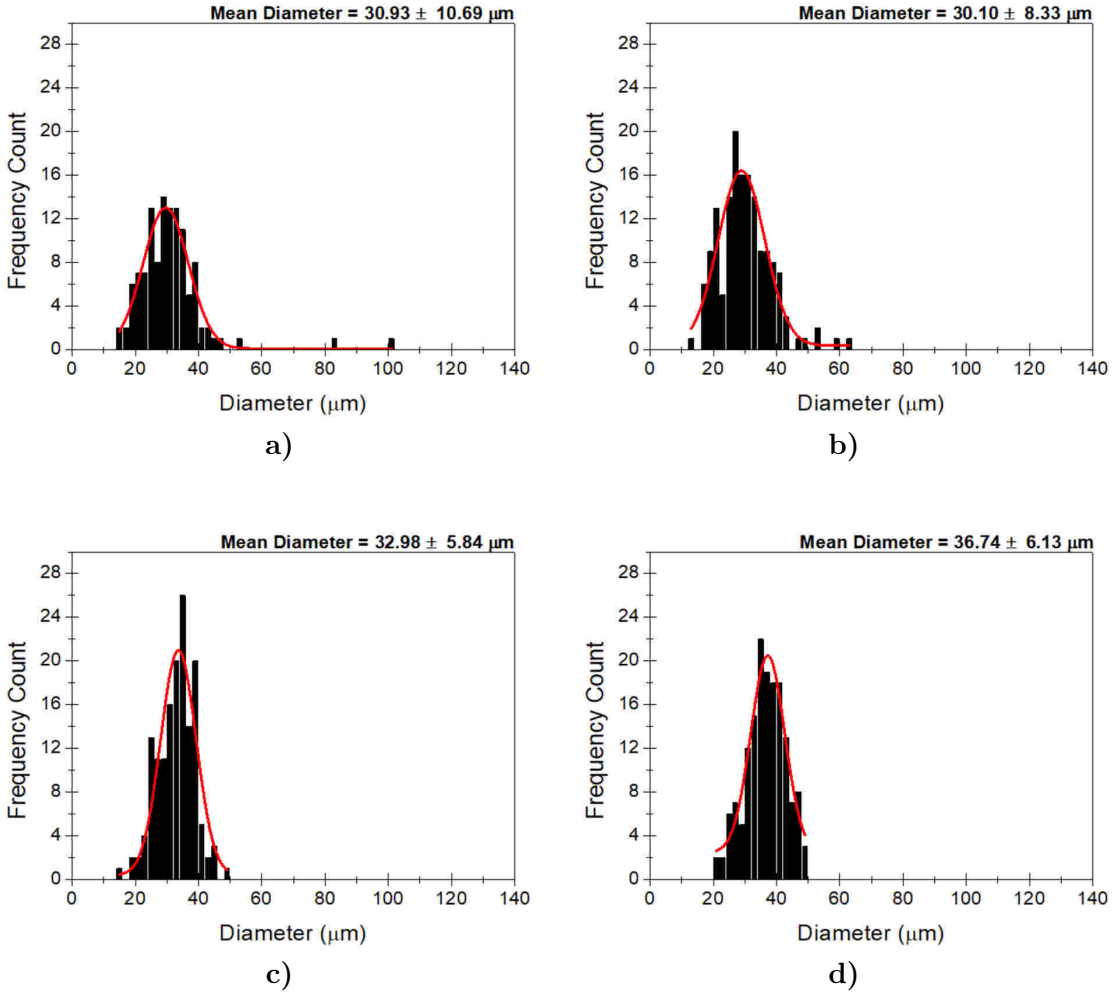

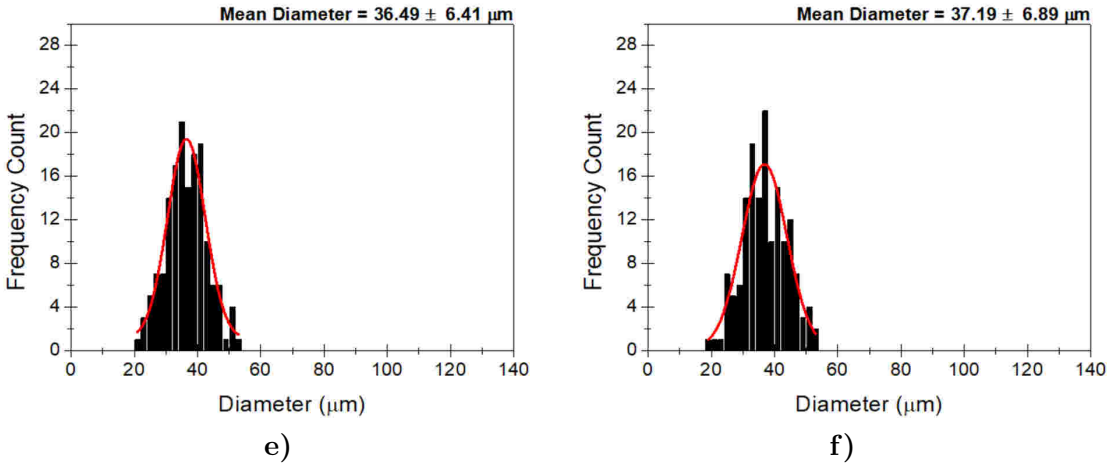

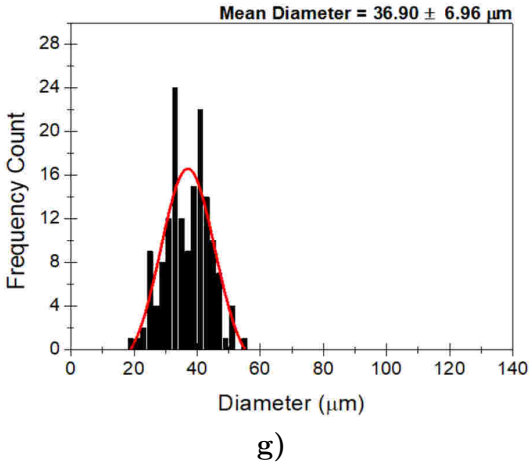

Figure 4.29. Droplet size distribution for Ca 0.06 and varying R_f. **a)** R_f 0.08, **b)** R_f 0.1, **c)** R_f 0.12, **d)** R_f 0.14, **e)** R_f 0.16, **f)** 0.18, and **g)** 0.2.

In figure 4.29 it can be observed that the size distribution of the droplets remains constant with the increase of R_f. Yet, two peaks can be distinguished for R_f 0.2 for diameters around 33 and 41 nm. For Ca 0.06 the smallest droplets have been obtained with R_f 0.1 with a mean size of 30.10 $\pm$ 8.33 μm, with continuous and dispersed phase velocities of 20.405 and 2.0405 mm/s respectively.

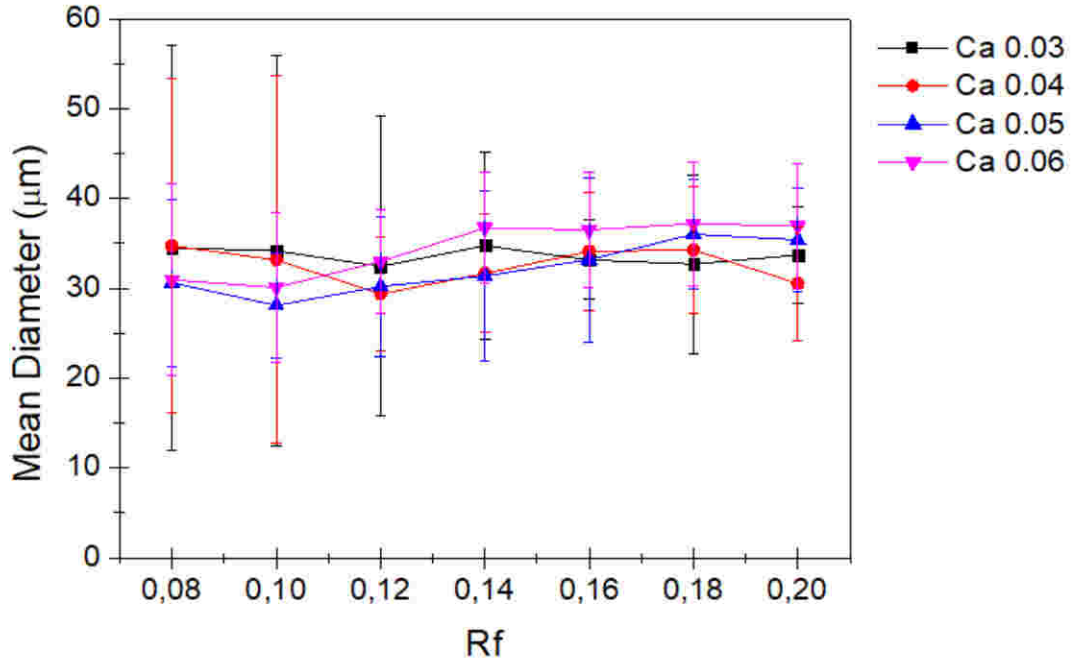

Figure 4.30. Droplet diameter size trend for a constant Ca. In black Ca 0.03, in red Ca 0.04, in blue Ca 0.05, and pink Ca 0.06.

Figure 4.30 serves as a summary of the evolution of the droplets' diameter as a function of R_f for constant Ca values. It can be observed that all Ca values follow a similar trend, which is the decrease of the droplet size along with the R_f. Yet, it can also be observed that for low Ca and R_f, 0.03-0.04, and 0.08-0.12, respectively, the standard deviation increases.

The first simulations of the T-junction geometry were carried out using the parameters previously found for both, the 90° flow-focusing geometry, and 45° flow-focusing geometry.

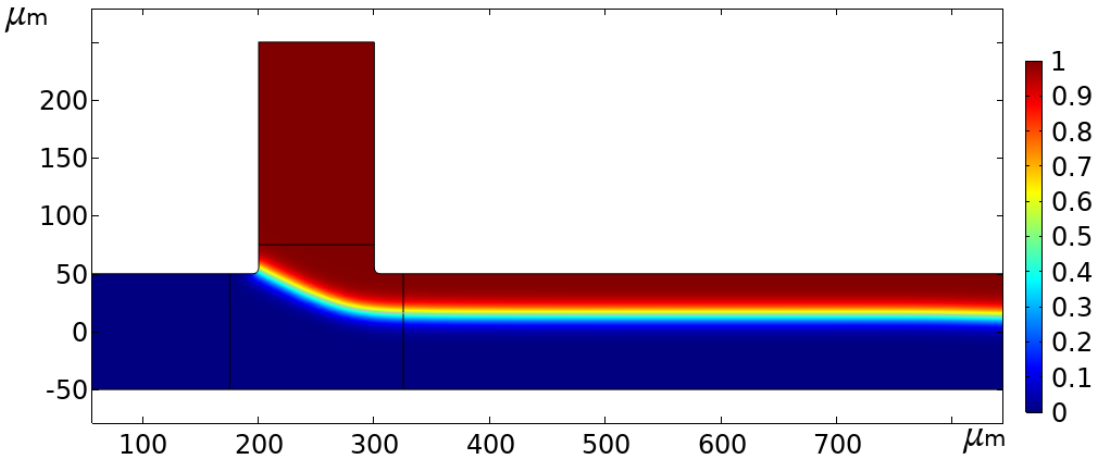

Figure 4.31. Screenshot of COMSOL. Droplet simulation with Ca 0.05 and R_f 0.2. The scale bar indicates the level set function, where 0 represents the continuous phase and 1 the dispersed phase.

The simulation of the T-junction geometry with Ca 0.05 and R_f 0.2 is shown in figure 4.31. As it can be seen for u_c of 17.004 mm/s and, u_d of 3.4009 mm/s resulted in a jetting regime.

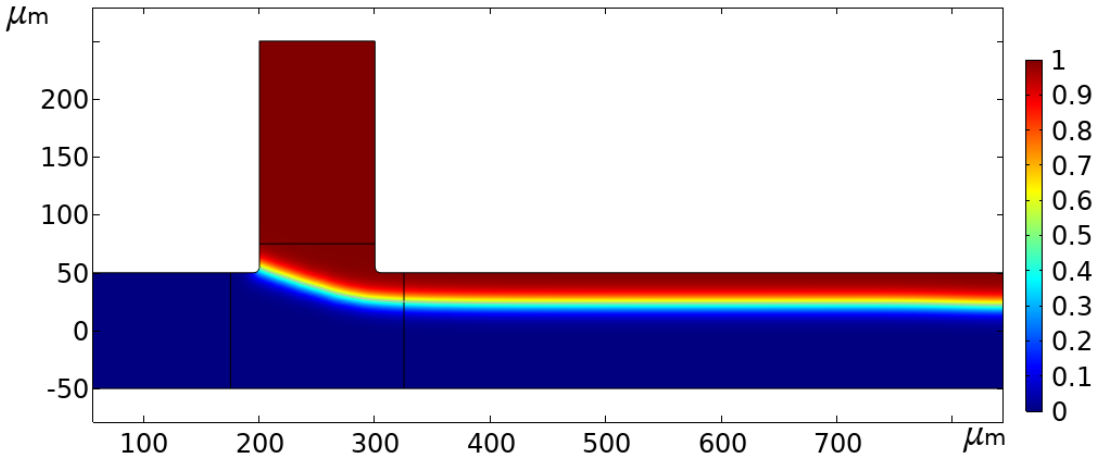

Figure 4.32. Screenshot of COMSOL. Droplet simulation with Ca 0.03 and R_f 0.1. The scale bar indicates the level set function, where 0 represents the continuous phase and 1 the dispersed phase.

To try to achieve a dripping regime another simulation was carried out by reducing Ca to 0.03 and the R_f to 0.1 shown in figure 4.32. As it can be observed for u_c of 10.203 mm/s and u_d of 1.0203 mm/s a jetting regime is achieved and therefore there is no droplet formation.

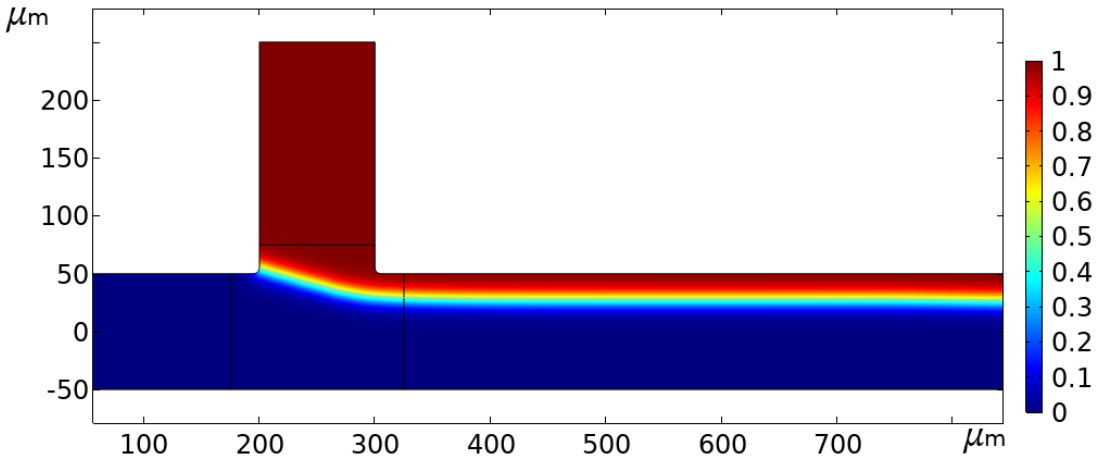

Figure 4.33. Screenshot of COMSOL. Droplet simulation with Ca 0.03 and R_f 0.07. The scale bar indicates the level set function, where 0 represents the continuous phase and 1 the dispersed phase.

In figure 4.33 is shown the simulation carried out with Ca 0.03 and R_f 0.07. As it can be seen for u_c of 10.203 mm/s and u_d of 0.714 mm/s a jetting regime is achieved and therefore there is no droplet formation. Several simulations were carried out for the T-junction geometry, yet any of the simulations yielded formation of droplets but instead a jetting regime attached to the upper wall similar to figure 4.33. To try to overcome that, the contact angle was increased to 180° nonetheless no droplets were formed.

4.4 Droplet Generation

This section serves to describe and compare the characterisation with Nanoparticle tracking analysis (NTA) and scanning electron microscope (SEM) of the droplets generated with different techniques.

4.4.1 Electrospray

Three different protocols were followed to generate droplets via electrospray (ES).

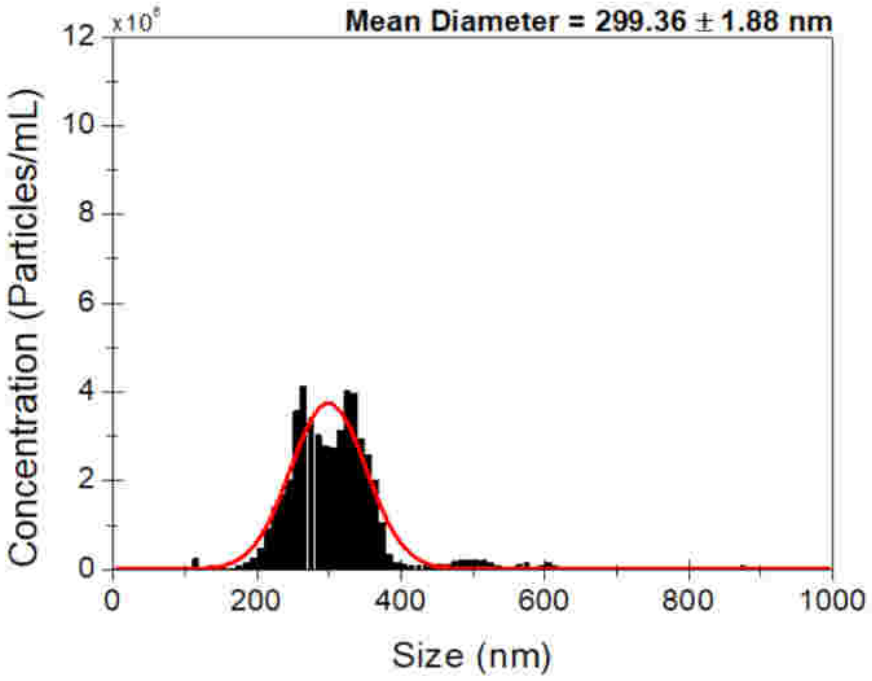

Figure 4.34. Droplet size distribution for a total injected volume of 5 mL and injection flow rate of 70 μL/min. In black is represented the concentration multiplied by a factor of 10^6, and in red a Gaussian fit.

In figure 4.34 is shown the size distribution of the droplets generated with ES with a total volume of 5 mL of a solution 1 wt% alginate 30% ethanol (EtOH) with a flow rate of injection of 70 μL/min. Even though the droplet size distribution follows a gaussian distribution, two peaks can be distinguished around 265 and 335 nm. With this protocol droplets with a mean size of 299.36 $\pm$ 1.88 nm were obtained.

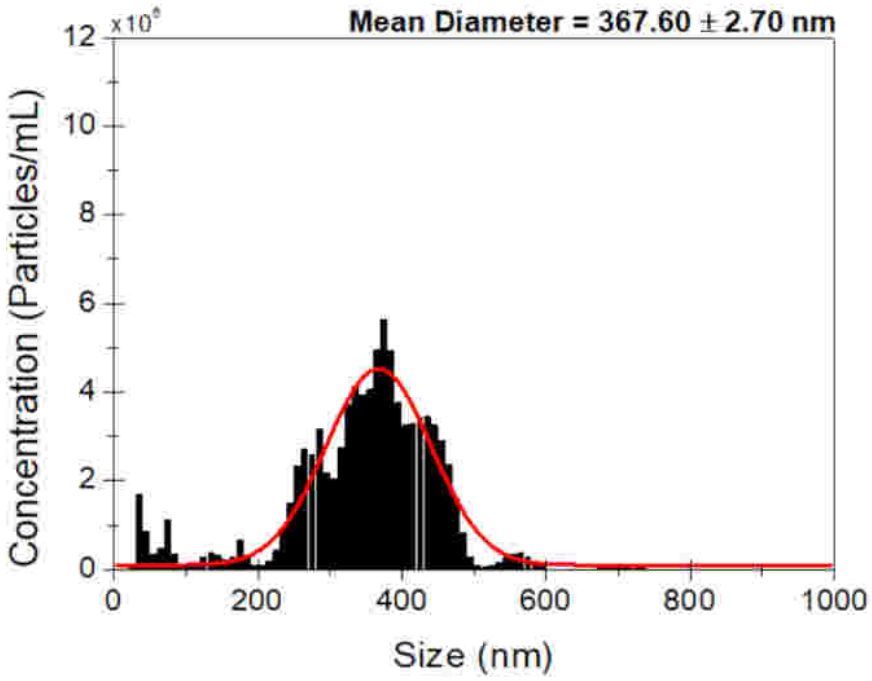

Figure 4.35. Droplet size distribution for a total injected volume of 7 mL and injection flow rate of 70 μL/min. In black is represented the concentration multiplied by a factor of 10^6, and in red a Gaussian fit.

In figure 4.35 is shown the size distribution of the droplets generated with ES with a total volume of 7 mL of a solution 1 wt% alginate 30% ethanol (EtOH) with a flow rate of injection of 70 μL/min. Different populations can be seen, one under 200 nm outside the gaussian distribution, and a second population over 200 nm. Even though, the particles over 200 nm inside follow a normal gaussian distribution, five different peaks can be observed at 285, 335, 375, 435, and 565 nm. With this protocol droplets with a mean size of 367.60 ± 2.70 nm were obtained.

The emulsions E7+3_7 were also characterised with SEM, were three different preparation procedures were tested.

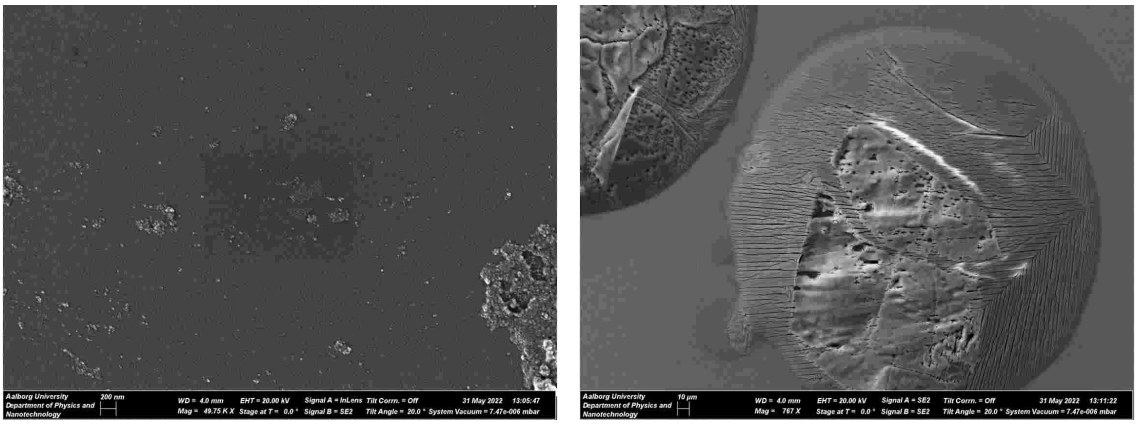

a) **b)**

Figure 4.36. SEM images of dried out wafer. **a)** shows some debris on the silicon wafer, **b)** shows dried out droplet. Scale bars are 1 μm and 10 μm respectively.

In figure 4.36 it is shown the wafer with the sample left to dry. In **a)** some debris can be seen on the surface of the wafer. In **b)** a dried out droplet can be observed.

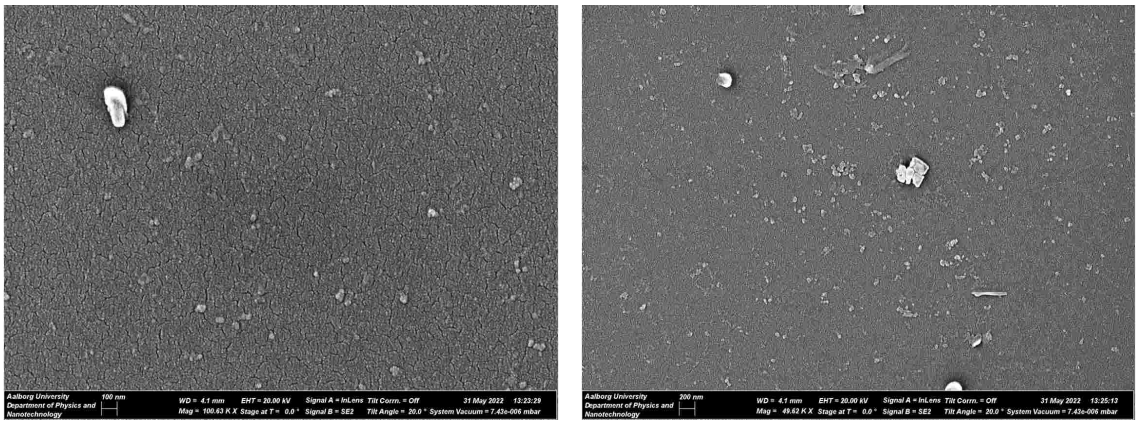

a) **b)**

Figure 4.37. SEM images of a wafer incubated for 10 minutes with the sample. **a)** shows some debris on the silicon wafer, **b)** shows a crystal salt. Scale bars are 100 m and 200 nm respectively.

Similar to the dried-out sample, in the wafer incubated for 10 minutes with the sample shown in figure 4.37 no droplets could be observed. However, what was present in the wafer were debris (**a)**), and salt crystals (**b)**).

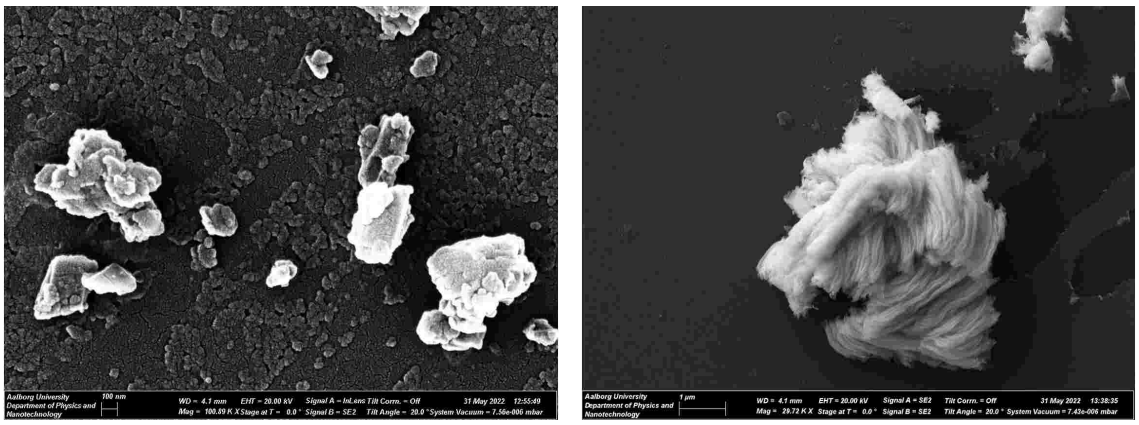

a) **b)**

Figure 4.38. SEM images of a wafer incubated for 5 minutes with the sample. Both **a)** and **b)** show structures deposited on top of the silicon wafer. Scale bars are 200 m and 100 nm respectively.

Similar to the other two protocols deposited on top of the wafer could be observed some debris and salt crystals, however, bigger structures fibrous-like were also present as shown in figure 4.38 could also be observed. In **a)** gold islands ($\sim$ 20 nm) can also be observed.

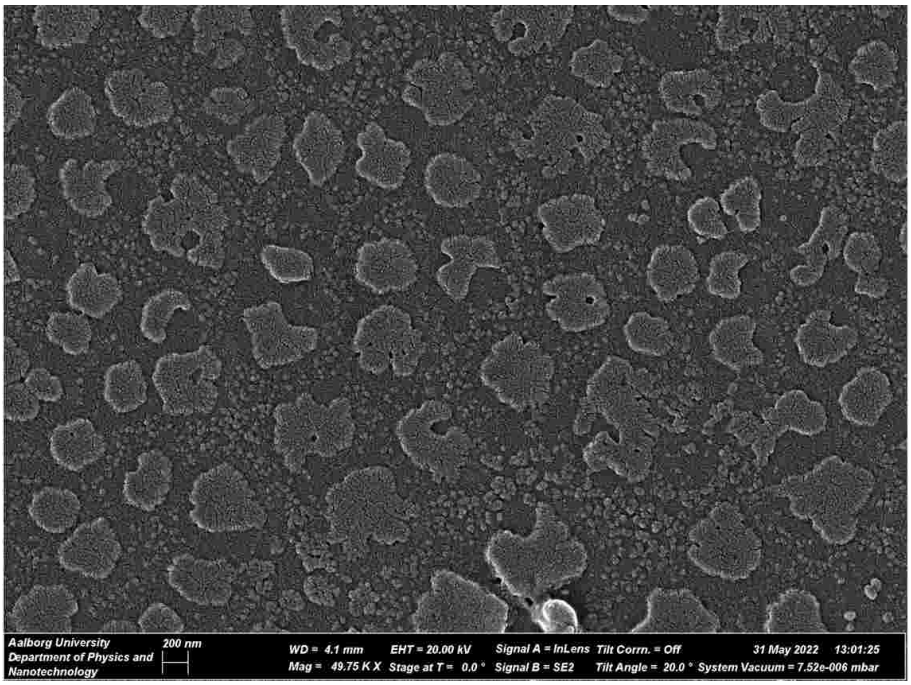

Figure 4.39. SEM image of ES sample incubated for 5 minutes in the wafer. Scale bar is 200 nm,

In figure 4.39 can be observed deposited particles on the silicon wafer. The particles are round-like even though irregularly shaped.

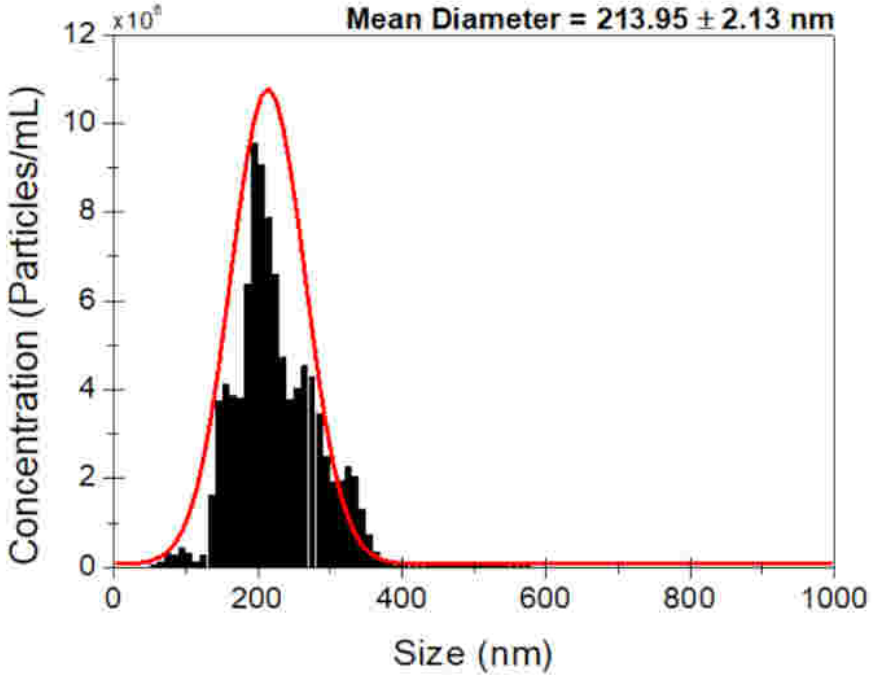

Figure 4.40. Droplet size distribution for a total injected volume of 7 mL and injection flow rate of 50 μL/min. In black is represented the concentration multiplied by a factor of 10^6, and in red a Gaussian fit.

In figure 4.40 is shown the size distribution of the droplets generated with ES with a total volume of 7 mL of a solution 1 wt% alginate 30% ethanol (EtOH) with a flow rate of

injection of 50 μL/min. Different populations can be seen, one around 100 nm, and the other over 100 nm. However, for the population of droplets over 100 nm four peaks can be observed at 155, 195, 265, and 325 nm. With this protocol droplets with a mean size of 213.95 ± 2.13 nm were obtained.

Sample	Size [nm]	Concentration [particles/mL] $\cdot 10^7$
ES5+10$_7$	299.36 ± 1.88	7 ± 0.72
ES7+3$_7$	367.60 ± 2.70	12.2 ± 1.3
ES7+3$_5$	213.95 ± 2.13	6.1 ± 0.5

Table 4.3. Summary of the droplet size and concentration obtained with different protocols of electrospray.

In table 4.3 is shown a summary of the different ES protocols followed showing the average size and average concentration of the droplets generated.

4.4.2 High-Speed Stirring

Two different protocols and two different velocities were tested to generate droplets via high-speed stirring (HHS).

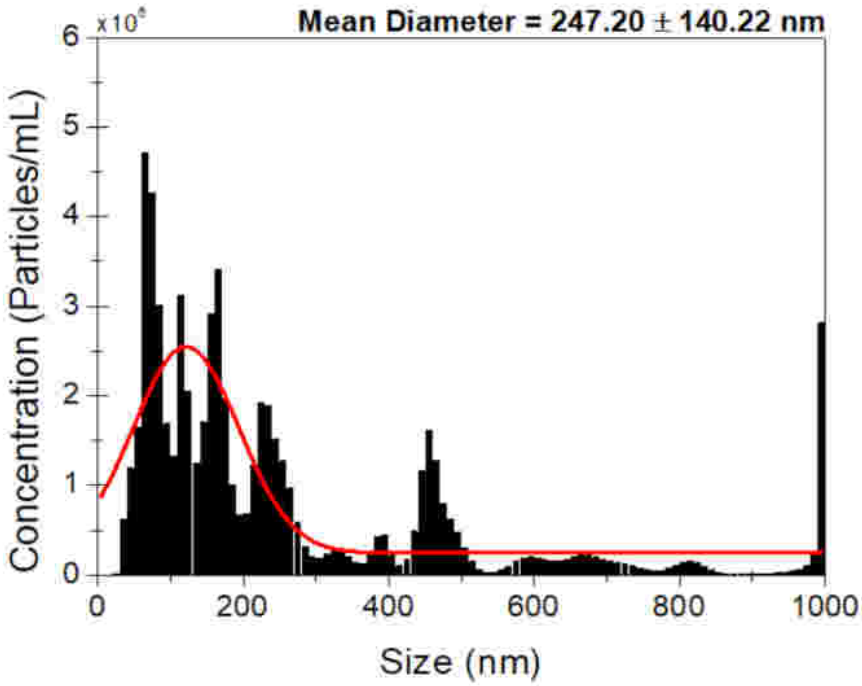

Figure 4.41. Droplet size distribution for HSS at 15,000 rpm after adding alginate solution. In black is represented the concentration multiplied by a factor of 10^6, and in red a Gaussian fit.

In figure 4.41 is shown the size distribution of the droplets generated with HHS after the addition of 1 mL of a solution 1 wt% alginate 5 wt% SDS with a rotor velocity of 15,000 rpm. Several peaks can be observed associated to a high polydispersity in the droplet size. With this protocol droplets with a mean size of 247.20 ± 140.22 nm were obtained.

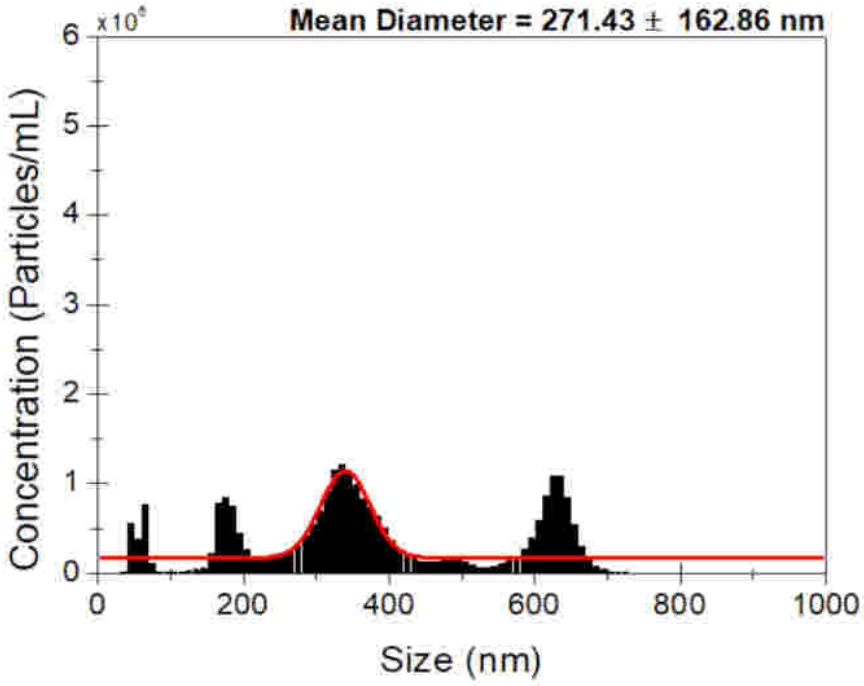

Figure 4.42. Droplet size distribution for HSS at 20,000 rpm after adding alginate solution. In black is represented the concentration multiplied by a factor of 10^6, and in red a Gaussian fit.

In figure 4.42 is shown the size distribution of the droplets generated with HHS after the addition of 1 mL of a solution 1 wt% alginate 5 wt% SDS with a rotor velocity of 20,000 rpm. Four peaks can be distinguished around 65, 175, 335, and 625 nm. With this protocol droplets with a mean size of 271.43 ± 162.86 nm were obtained.

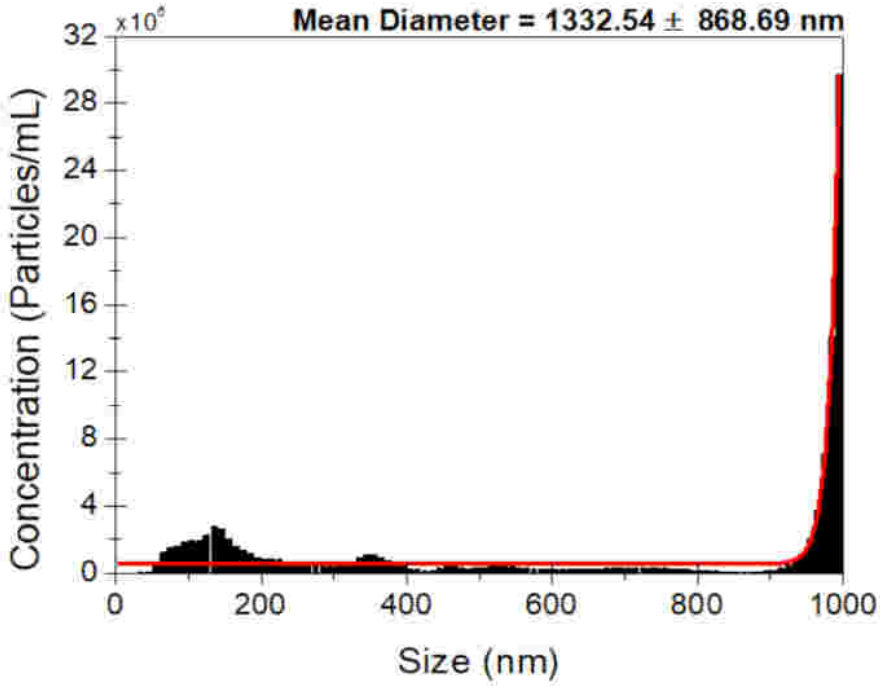

Figure 4.43. Droplet size distribution for HSS at 15,000 rpm while adding alginate solution. In black is represented the concentration multiplied by a factor of 10^6, and in red a Gaussian fit.

In figure 4.43 is shown the size distribution of the droplets generated with HHS at 15,000 rpm while adding drop-wise 1 mL of a solution 1 wt% alginate 5 wt% SDS. Even though several peaks can be observed the predominant one is for 1000 nm particles. With this protocol droplets with a mean size of 1332.54 ± 868.69 nm were obtained.

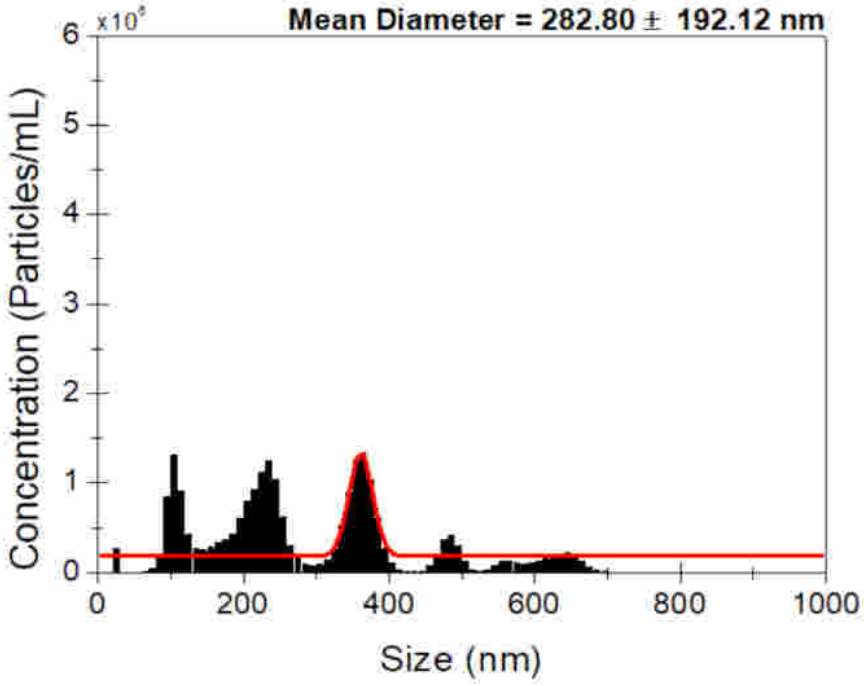

Figure 4.44. Droplet size distribution for HSS at 20,000 rpm while adding alginate solution. In black is represented the concentration multiplied by a factor of 10^6, and in red a Gaussian fit.

In figure 4.44 is shown the size distribution of the droplets generated with HHS at 20,000 rpm while adding drop-wise 1 mL of a solution 1 wt% alginate 5 wt% SDS. Different size populations can be observed with peaks at 105, 235, 365, 485, 565, and 645 nm. With this protocol droplets with a mean size of 282.80 ± 192.12 nm were obtained.

Sample	Size [nm]	Concentration [particles/mL] $\cdot 10^7$
HSS15,000A	247.20 ± 140.22	12.7 ± 0.55
HSS15,000DDW	1332.54 ± 868.69	17.2 ± 10.1
HSS20,000A	271.43 ± 162.86	2.88 ± 1.98
HSS20,000DDW	282.80 ± 192.12	2.47 ± 1.2

Table 4.4. Summary of the droplet size and concentration obtained with different protocols of high-speed stirring.

In table 4.4 is shown a summary of the different HSS protocols followed showing the average size and average concentration of the droplets generated.

Technique	Size [nm]	PdI
Electrospray	213.95 ± 2.13	∼0.241
High-Speed Stirring	247.20 ± 140.22	∼0.293
Microfluidics	28.08 ± 5.92	0.218

Table 4.5. Summary of the smallest droplets obtained with the different techniques used to generate emulsions.

In table 4.5 it is shown the smaller droplet size achieved for each technique altogether with the polydisperisty index.

4.5 DNA Isolation

In order to check the presence of the desired plasmid DNA an agarose gel electrophoresis was performed. The agarose gel can be seen in figure 4.45 below.

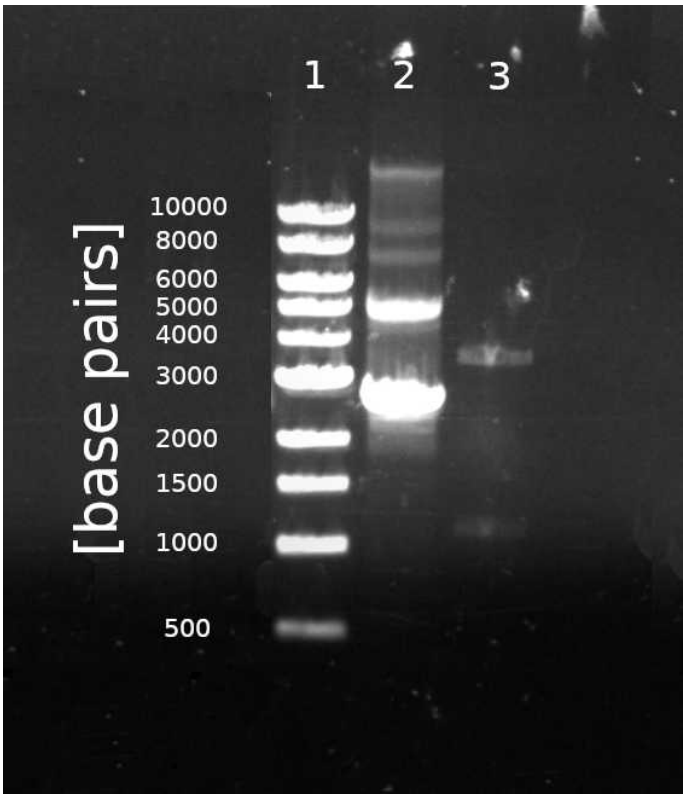

Figure 4.45. Agarose gel exposed to UV light. The loaded samples are: well 1 1kb DNA Ladder, well 2 non-digested pTagRFP-C, and well 3 digested pTagRFP-C with *EcoRI-HF* and *NdeI*.

In Well 2 contains several bands which correspond to different conformations of the undigested DNA. On the other hand, two vague bands can be seen in Well 3, one just above the 1,000 basepair (bp) indicator, and the second in between the 3,000 and 4,000 bp indicators.

4.6 Transfection

The transfection efficiency of the HeLa cells was characterised 24 and 48 hours after incubation with TagRFP.

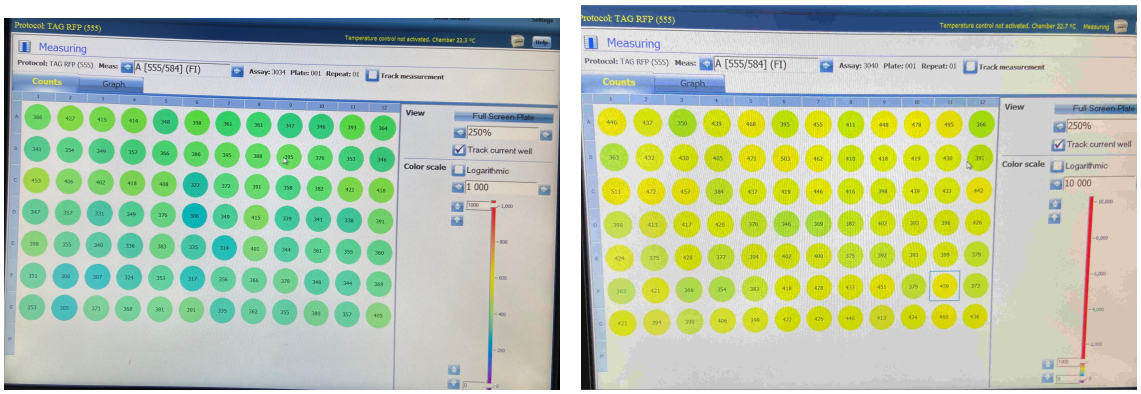

a) **b)**

Figure 4.46. Screenshot of EnSpire fluorescence intensity measurement. **a)** 24 hours after incubation, and **b)** 48 hours after incubation. Fluorescence intensity scale goes from 0 (purple) to 1,000 (red).

The characterisation of the TagRFP transfection into HeLa cells with a fluorometer is shown in figure 4.46 **a)** after 24 hours and **b)** after 48 hours. In both cases it can be observed that there is not a great variability in the fluorescence intensity of the different samples. In both incubation times, some wells of the negative control show more intensity than the cells incubated with plasmid DNA either free or with a carrier. However, it can be seen that the fluorescence intensity after incubating for 48 hours has increased compared to the intensity after 24 hours.

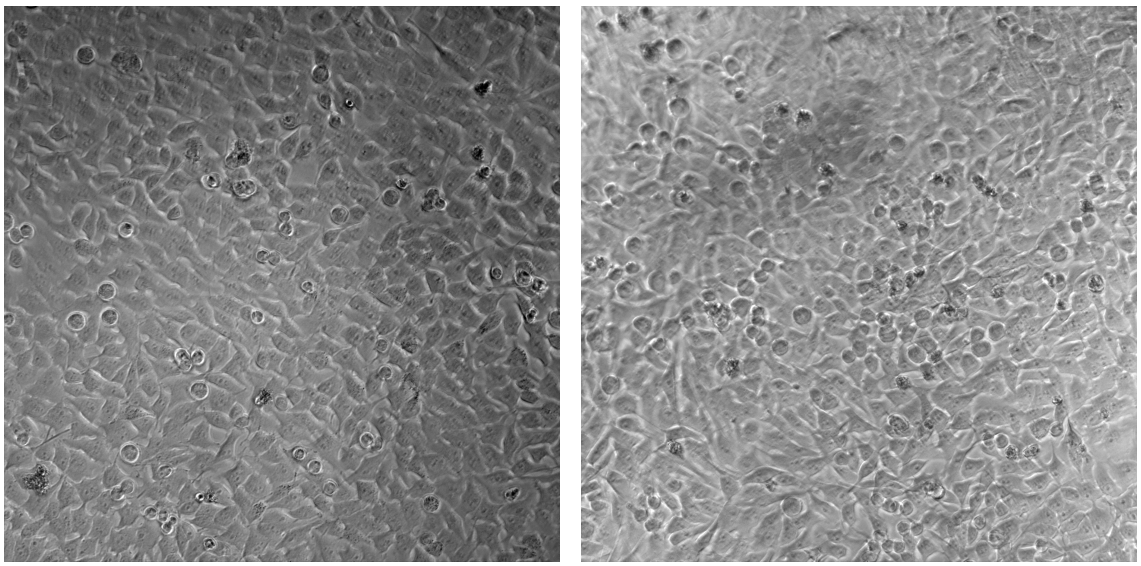

a) **b)**

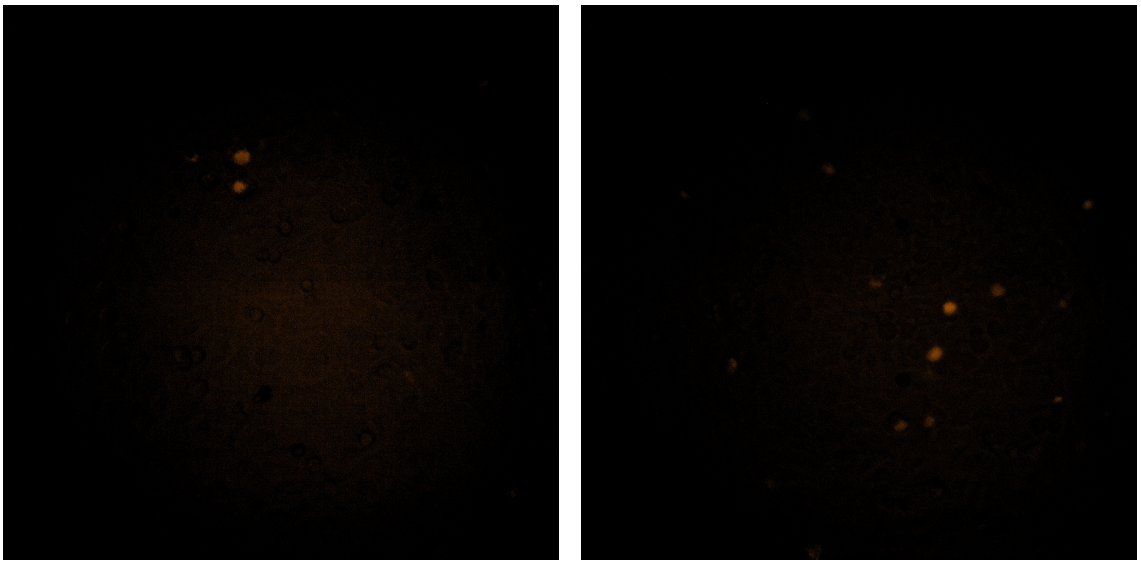

c) **d)**

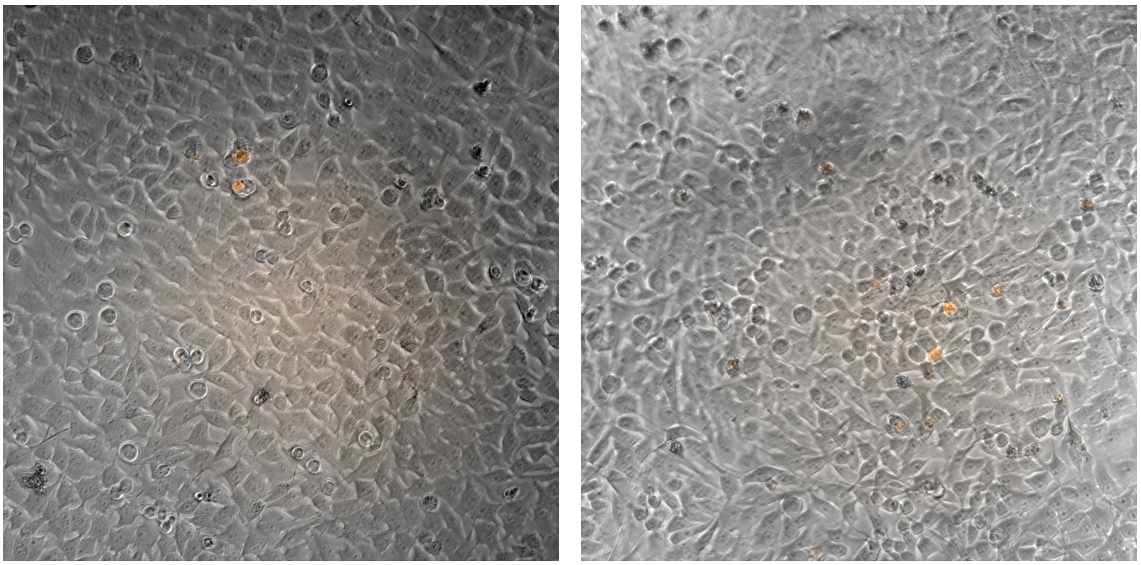

e) **f)**

Figure 4.47. Negative control for the transfection of TagRFP. On the left, HeLa cells were incubated for 24 hours, on the right the cells were incubated for 48 hours. **a)** and **b)** show the phase channel; **c)** and **d)** show the fluorescence channel; and **e)** and **f)** are an overlay of both channels.

In figure 4.47 is shown negative control for the transfection of TagRFP. HeLa cells were incubated for **a)** 24 hours and **b)** 48 hours with 200 μL of DMEM buffer. Some fluorescence (orange) can be observed in some of the rounder cells.

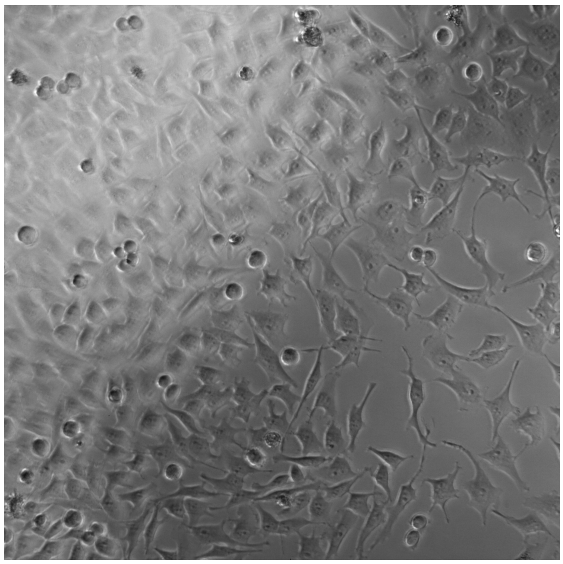

a)

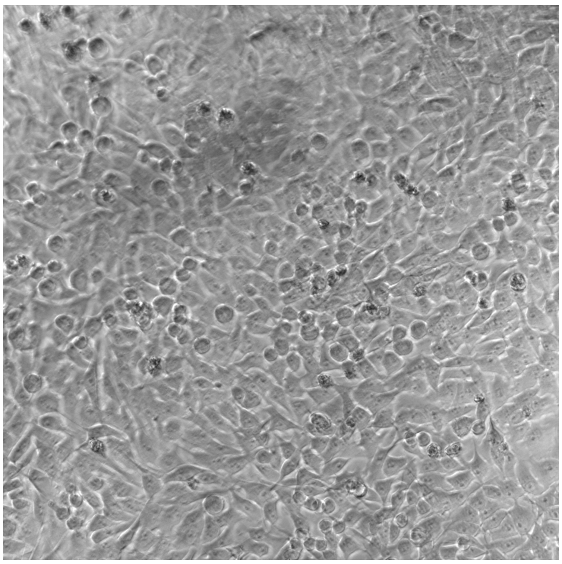

b)

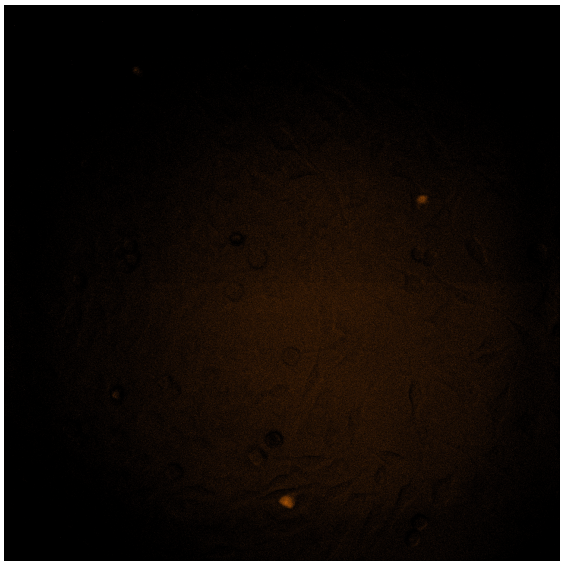

c)

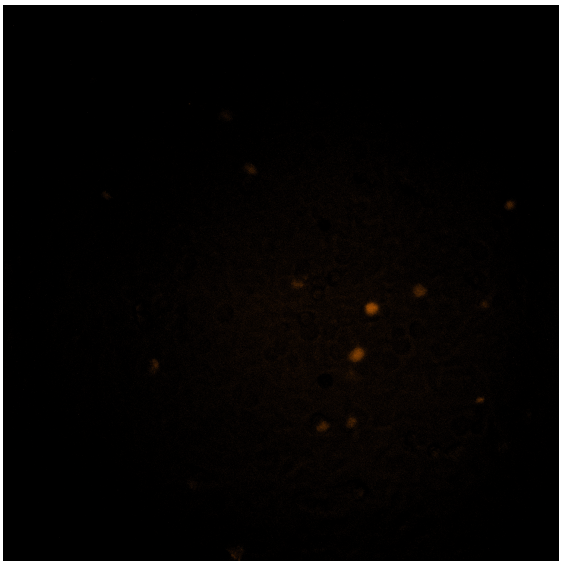

d)

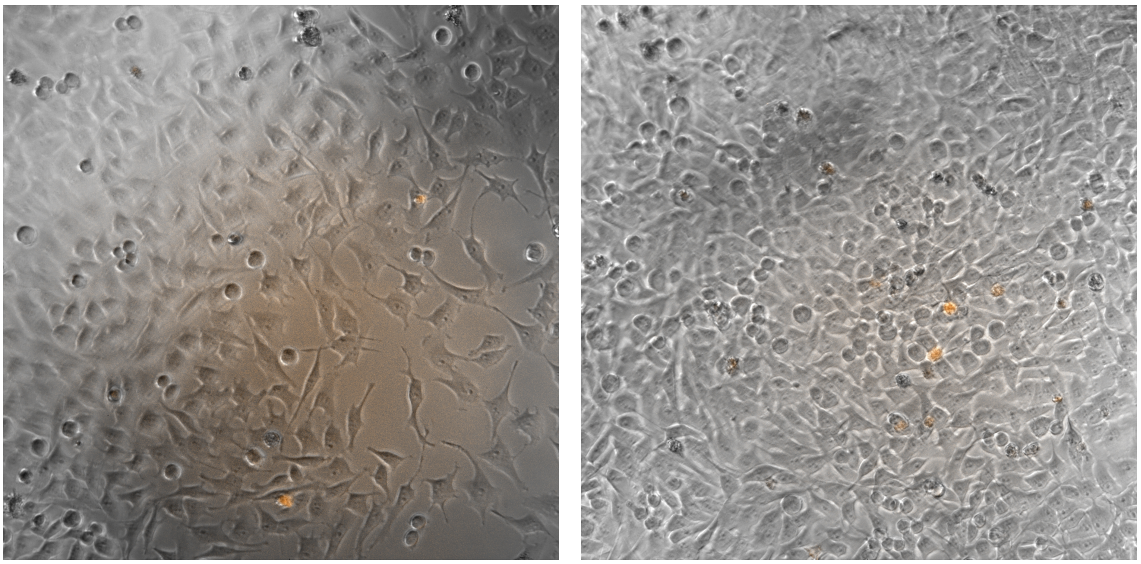

e) **f)**

Figure 4.48. Incubation of HeLa cells with free pTagRFP-C plasmid. On the left, HeLa cells were incubated for 24 hours, on the right the cells were incubated for 48 hours. **a)** and **b)** show the phase channel; **c)** and **d)** show the fluorescence channel; and **e)** and **f)** are an overlay of both channels.

In figure 4.48 is shown the fluorescence of HeLa cells after incubating them with free pTagRFP-C plasmid. HeLa cells were incubated for **a)** 24 hours and **b)** 48 hours with 198 μL of DMEM buffer mixed with 2 μL of free plasmid. Similar to the negative control, some fluorescence (orange) can be observed in some of the rounder cells.

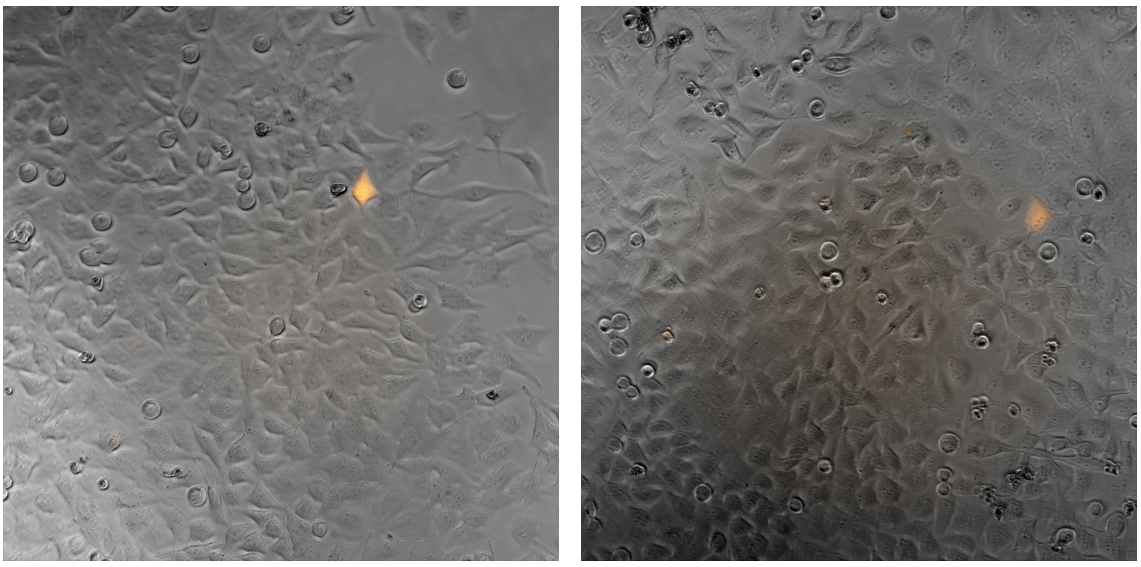

a) **b)**

Figure 4.49. HeLa cells incubated for 24 hours with plasmid pTagRFP-C mixed with poly-L-lysine. **a)** and **b)** are snapshots of different cells belonging to the same well (B11).

In figure figure 4.49 it is shown the fluorescence of HeLa cells after 24 hours of incubation with pTagRFP-C mixed with poly-L-lysine. Opposed to the negative control and the free pTagRFP, it can be observed that the fluorescent cells are attached to well as they are not round.

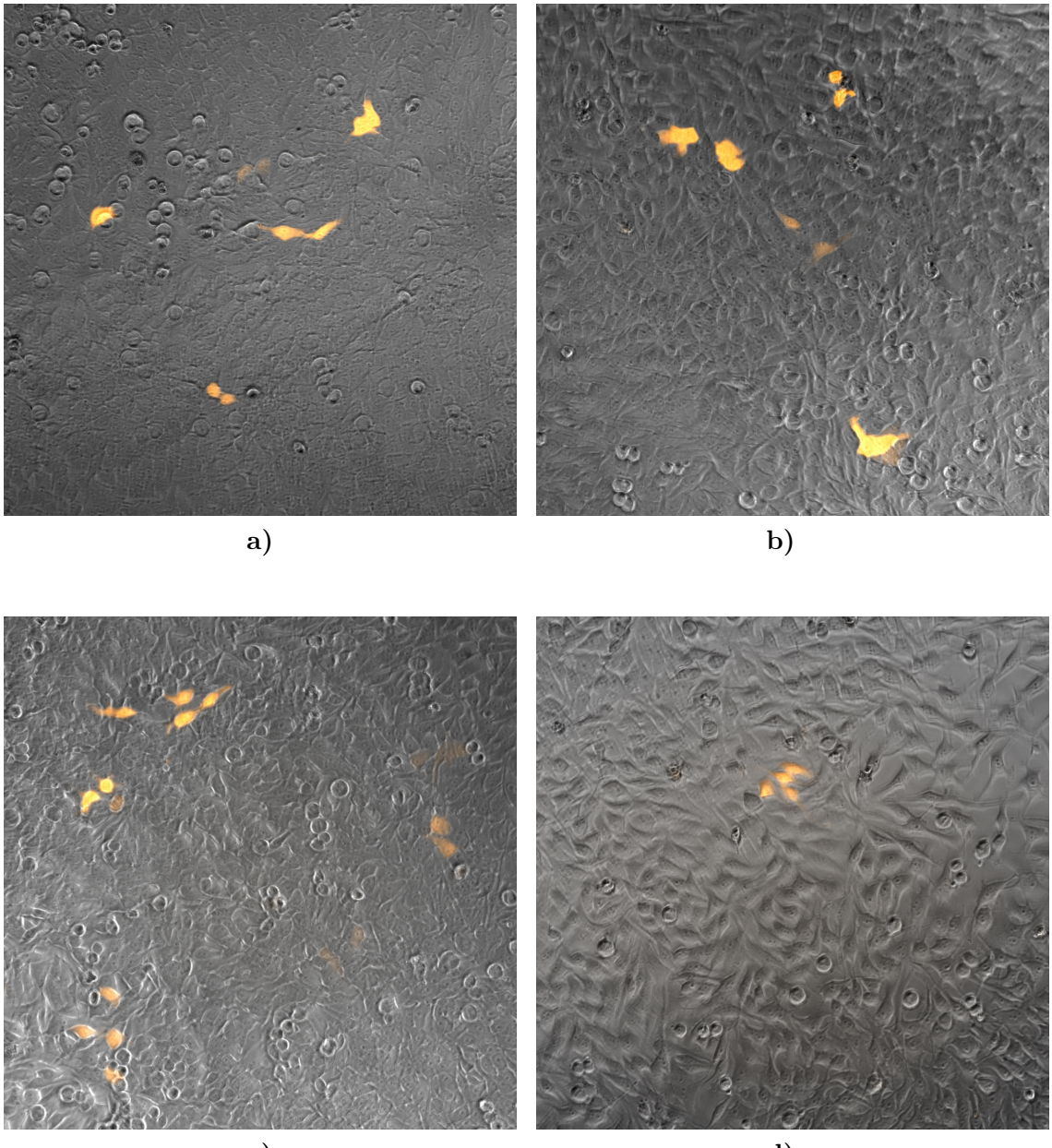

a) **b)**

c) **d)**

Figure 4.50. HeLa cells incubated for 48 hours with plasmid pTagRFP-C mixed with poly-L-lysine. **a)** and **b)** are snapshots of different cells belonging to the same well (B11).

in figure 4.50 it is shown the fluorescence of HeLa cells after 48 hours of incubation with pTagRFP-C mixed with poly-L-lysine. It can be observed that more cells show fluorescence creating small colonies.

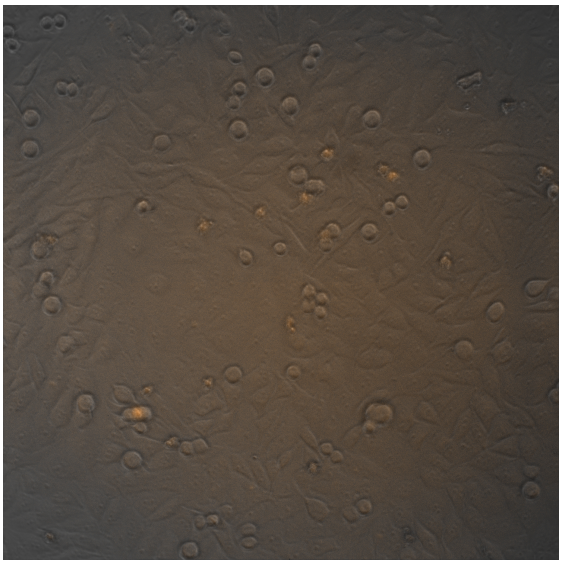

a)

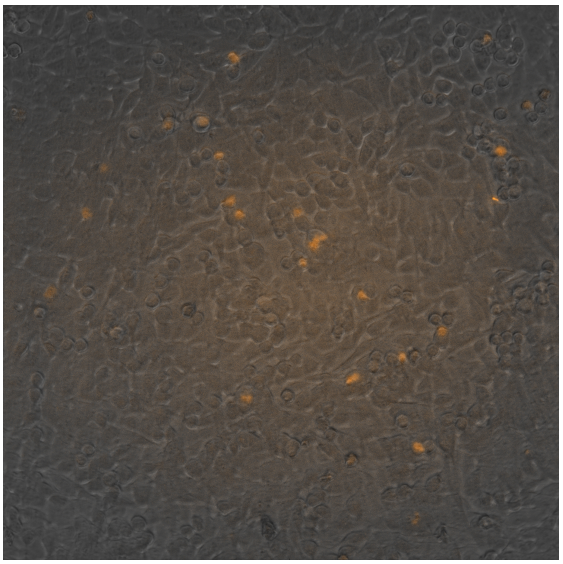

b)

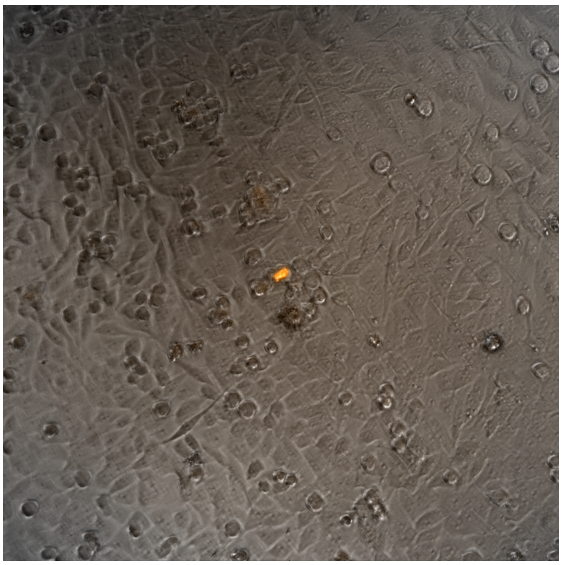

c)

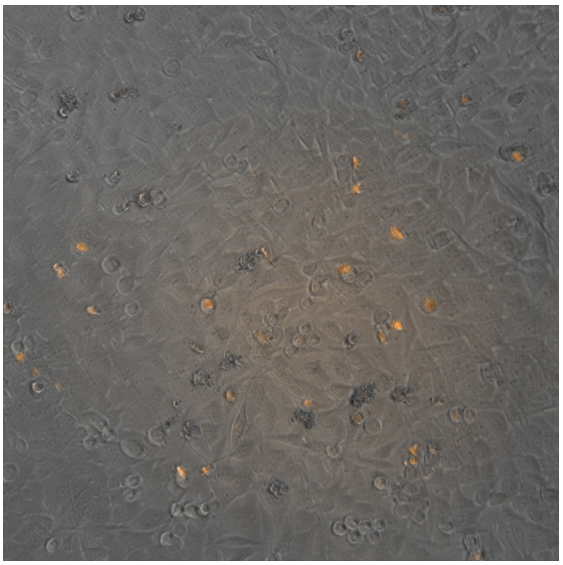

d)

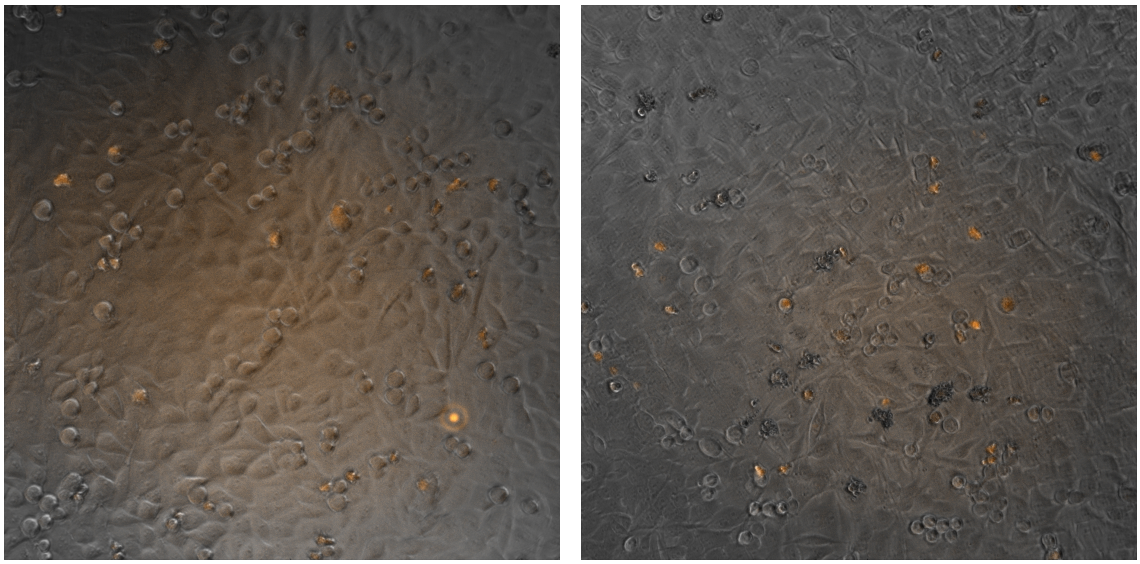

e) **f)**

Figure 4.51. HeLa cells incubated for 24 hours (left) and 48 hours (right) with droplets encapsulating plasmid pTagRFP-C.

In figure 4.51 it is shown the fluorescence of HeLa cells incubated with the emulsions containing the pTagRFP-C. It can be observed that both incubation times present some fluorescence. However, the number of fluorescent cells is increased after incubating for 48 hours.

Chapter 5

Discussion

This chapter serves to discuss the results presented earlier and follows the same structure regarding the setup.

5.1 Droplet Generation

The first part of the droplet generation consisted of the simulation of a two-phase laminar flow in all the different geometries.

5.1.1 Simulations

The simulations were carried out for 3D printed geometries with a channel height of 400 μm showed that both, the time to reach a steady-state of droplet generation, and the size of the droplets are geometry-dependent. As shown in table 4.1 and 4.1 the steady-state of droplet generation is faster for the 90° flow-focusing geometry, than the 45° with times of 0.21 and 0.31 seconds respectively.

As a general trend for the 90° flow-focusing geometry, the mean size of the droplets decreases with the R_f, however, as shown in figure 4.24 for R_f values of 0.08 and 0.1 the droplet size is increased. This increase in the droplet size could be a consequence of the low continuous-phase velocity, which does not generate enough shear stress, leading to the break-off of the droplet due to build up pressure.

It was also found that the steady-state for droplet formation depends on both, the channel height, and geometry. Channels with a height of 100 μm reached a steady state of droplet formation faster than the 400 μm channels, 0.05 seconds compared to 0.16 seconds respectively (90° geometry). For the 400 μm channels the effect of the geometry in the time to reach a steady state was as more evident than in the 100 μm channels, the steady state being reached at 0.16 seconds for the 90°, and 0.36 seconds for the 45°. The results are in accordance with the literature found as the smaller channel height results in a faster flow of the continuous-phase surrounding the dispersed-phase which leads to an increase in the viscous shear forces. This results in a faster droplet break-off and therefore in more monodispersed droplets. [175]

Even though no results could be obtained for either of the T-junctions, it has been found in some literature that as the T-junctions do not use hydrodynamic focusing the droplet formation regime is squeezing instead of the dripping regime of the flow focusing geometries. A squeezing regime entails a droplet break-off due to the build-up pressure

in the channel which will be filled up by the droplet. Therefore, for the T-junctions, the droplet size would be similar to the channel height. [108], [112]–[114], [176]

5.1.2 Experimental Droplet Generation

The size distribution of the different protocols used to generate droplets via electrospray (ES) (figure 4.34 to 4.40) show that the flow rate of injection of the alginate solution plays a key role in the size of the droplets. From table 4.3 it can be observed that using the same protocol but increasing the injection flow ratio 20 μL there is an increase in the droplet size of 71.82%. The results

The results obtained with the different high-speed stirring protocols are shown in table 4.4 indicate that homogenising after the addition of the alginate solution yields smaller droplets compared to the results of homogenising while adding the alginate solution drop-wise. The difference in the droplet size is more evident when homogenising at 15,000 rpm.

It must be noted that NTA can represent noise signals as particles typically around 100 nm with a narrow size distribution. Furthermore, the high variability in the concentration of droplets estimated by could be due to the low concentration of particles during the analysis.

5.2 Plasmid DNA isolation

To confirm the presence of the plasmid DNA encoding the Tag RFP, the plasmid pTagRFP-C was digested with *NdeI*, and *EcoRI-HF*. As shown in figure 4.45, where Well 2 had a clear band in between the 4,000 and 5,000 basepairs (bp) indicators which correspond to the undigested plasmid with 4,725 bp. Well 3 contained the plasmid digested both with *NdeI* and *EcoRI-HF*, and showed two vague bands above the 1,000 and 3,000 bp corresponding to the two fragments obtained after the digestion of digesting the pTagFPF-C with sizes of 1,120 and 3.605 bp respectively.

5.3 Transfection

From the fluorescence intensity results obtained with the fluorometer measurements it can not be determined if the transfection of the TagRFP into HeLa cells was successful or not as all wells (i.e., negative control, free plasmid DNA, and samples) show similar levels of fluorescence. Furthermore, the increase in fluorescence between the 24 and 48 hours of incubation (figure 4.46 could also be due to a change in the medium composition due to its consumption by the cells, as the colour of the medium changed from red to yellowish.

The measurements carried out with the fluorescence microscope (FM) showed that HeLa cells belonging to the negative control showed some fluorescence as shown in figure 4.47. Yet, several images taken of the negative control indicate that the fluorescence is associated to cells in suspension with rounder shape and higher membrane density, which associated to cells undergoing division or dead cells.

A similar behaviour could be observed for the cells incubated with free plasmid figure 4.48. It could be observed that the fluorescent cells were round and thus in suspension and not to the transfection of the pTagRFP-C. However, when the free plasmid was

incubated for 30 minutes with poly-L-lysine some transfection could be observed after incubating the HeLa cells for 24 hours as shown in figure 4.49. The transfection of the pTagRFP-C was more evident after 48 hours as shown in figure 4.50, however, the formation of fluorescent colonies suggest that the fluorescent cells were generations of cells.

Fluorescent HeLa cells were visible after incubation with alginate droplets encapsulating pTagRFP. Yet, it could be observed that the fluorescence proceeded from cells in suspension, with rounder shape, and not due to transfection. Nonetheless, it could also be observed that after incubating for 48 hours more cells were not attached t o the bottom of the well, and presenting fluorescence as shown in figure 4.51.

Chapter 6

Conclusion

Casting of Microfluidic Chips

The results obtained from the 3D printing suggest that while it was possible to print negative geometries with a minimum element size of 400 μm, it is not possible, with the equipment in the lab, to print hollow geometries, i.e., channels, of that size as the resin can not get out during the printing process and polymerises blocking the channel.

Nanoemulsions

Simulations carried out in COMSOL show that the droplets' sizes were in the micrometre range with the smallest diameters around 30 μm. The simulations also suggest that while the dimensions of the channel play a key role in the size of the generated droplets, the geometry is also important. It was found that the flow-focusing geometries generated droplets with size in the order of the HeLa cells, and therefore, it could be concluded that to use microfluidics to generate nanoemulsions, techniques with resolution around 500-1000 nm obtaining smaller droplets, which diameters could range from 0.5-1 μm. Droplets of this size are speculated to be internalised by the cells via macropinocytosis. [68], [70], [72], [73] From the results shown in table 4.5 it can be concluded that the best procedure is electrospraying using a flow rate of 50 μm/min. However, microfluidic systems offer the emulsions with less polydispersity.

Transfection

From the results from the transfection into HeLa cells it can be seen that transfection occurred when the plasmid was incubated with poly-L-lysine figure 4.49, however, the wells containing free plasmid DNA or the droplets encapsulating the plasmid no transfection could be observed (figure 4.48. The transfection of poly-L-lysine, which is positively charged, was enhanced due to electrostatic interactions with the negatively charged membrane as reported by different studies. [53], [59]–[61] The lack of transfection for the free plasmid DNA and the droplets could also be associated with their low concentration but could also with their surface charge, negative for the DNA. It is also speculated that the plasmid DNA encapsulated in alginate droplets requires more time for the transfection to occur. Furthermore, the incubation of HeLa cells with droplets shows that after 48 hours of incubation the number of cells emitting fluorescence due to a change in their membrane density increased. This change in the membrane composition is speculated to be associated

with the high concentration of Ca^{2+} present in the droplets diluent, an aqueous solution containing $CaCl_2$ (25 g/L). Two different reasons are speculated to cause this increase in membrane density. One is that the high concentration of Ca^{2+} in the medium is cytotoxic to the cell leading to cell death due to the disruption of the cell homeostasis, as calcium ions regulated many physiological processes as proposed by Orrenius and Nicotera and other studies. [177]–[180] Another possibility is that the high concentration of Ca^{2+} ions triggers cell division as proposed by Rosendo-Pineda *et al.*.[181]

Chapter 7

Further Studies

To be able to experimentally determine which of the different techniques used in this project to generate nanoemulsions is better the casting of the microfluidic chips with 100 and 400 μm channels should be cast, and to experimentally generate droplets using the parameters found in the COMSOL simulations. The protocol to cast the photomasks is the following:

A silica wafer is placed in acetone and is cleaned by unltrasonication for five minutes.The wafer is then treated in an STS RIE 320PC, where it was etched for five min at 300 W. Then, a thin layer of hexamethyldisilazane is spin coated on top of it. The dispersion time of the spin coating was 15 seconds, the maximum speed was 4000 rpm, and the acceleration was 500 rpm/s. The wafer is then placed on a 150°C hotplate for 3 minutes. The SU-8 3050 photoresist is then spin coated onto the wafer at 3,000 rpm to obtain a 50 μm thick layer. After spin coating, the wafer is placed in a 65°C hotplate for five minutes and then on a 95°C hotplate for another 30 minutes. The glass is then let to cool down to room temperature.

The wafer is then placed under a UV-light source with the photomask on top and is exposed for 450 seconds. After exposure, it is placed on a 65°C hotplate for five minutes followed by 10 minutes in a 95°C hotplate. Then, the wafer is placed in the developer (mr-Dev 600) for seven minutes, followed by a two-minute sonification in the developer. After sonification, the wafer is rinsed with isopropanol and blow-dried with a nitrogen gun.

The surface charge of the nanoemulsions should be determined to study whether or not it affects their internalisation by HeLa cells and therefore, the transfection efficiency.

Also, different purification protocols should be achieved to have higher droplet concentration and to flush any chemical or unbounded salt such as Ca^{2+} that could in any matter alter the medium composition or trigger any signalling in the cell that could affect the transfection.

Bibliography

[1] R. M. Mainardes and L. P. Silva, "Drug delivery systems: Past, present, and future," *Current drug targets*, vol. 5, no. 5, pp. 449–455, 2004.

[2] K. J. Gandhi, S. V. Deshmane, and K. R. Biyani, "Polymers in pharmaceutical drug delivery system: A review," *International journal of pharmaceutical sciences review and research*, vol. 14, no. 2, pp. 57–66, 2012.

[3] J. D. Kingsley, H. Dou, J. Morehead, B. Rabinow, H. E. Gendelman, and C. J. Destache, "Nanotechnology: A focus on nanoparticles as a drug delivery system," *Journal of Neuroimmune Pharmacology*, vol. 1, no. 3, pp. 340–350, 2006.

[4] A. Gupta, "Nanoemulsions," in *Nanoparticles for Biomedical Applications*, Elsevier, 2020, pp. 371–384.

[5] D. F. Emerich and C. G. Thanos, "Nanotechnology and medicine," *Expert opinion on biological therapy*, vol. 3, no. 4, pp. 655–663, 2003.

[6] M. Jaiswal, R. Dudhe, and P. Sharma, "Nanoemulsion: An advanced mode of drug delivery system," *3 Biotech*, vol. 5, no. 2, pp. 123–127, 2015.

[7] M. T. Guo, A. Rotem, J. A. Heyman, and D. A. Weitz, "Droplet microfluidics for high-throughput biological assays," *Lab on a Chip*, vol. 12, no. 12, pp. 2146–2155, 2012.

[8] T. P. Lagus and J. F. Edd, "A review of the theory, methods and recent applications of high-throughput single-cell droplet microfluidics," *Journal of Physics D: Applied Physics*, vol. 46, no. 11, p. 114 005, 2013.

[9] P. Kumari, B. Ghosh, and S. Biswas, "Nanocarriers for cancer-targeted drug delivery," *Journal of drug targeting*, vol. 24, no. 3, pp. 179–191, 2016.

[10] G. S. Kwon, "Polymeric micelles for delivery of poorly water-soluble compounds," *Critical Reviews™ in Therapeutic Drug Carrier Systems*, vol. 20, no. 5, 2003.

[11] Y. Luo and G. Prestwich, "Cancer-targeted polymeric drugs," *Current Cancer Drug Targets*, vol. 2, no. 3, pp. 209–226, 2002.

[12] H. Nehoff, N. N. Parayath, L. Domanovitch, S. Taurin, and K. Greish, "Nanomedicine for drug targeting: Strategies beyond the enhanced permeability and retention effect," *International journal of nanomedicine*, vol. 9, p. 2539, 2014.

[13] S. Baboota, F. Shakeel, A. Ahuja, J. Ali, and S. Shafiq, "Design, development and evaluation of novel nanoemulsion formulations for transdermal potential of celecoxib," *Acta pharmaceutica*, vol. 57, no. 3, p. 315, 2007.

[14] F. Shakeel, S. Baboota, A. Ahuja, J. Ali, M. Aqil, and S. Shafiq, "Nanoemulsions as vehicles for transdermal delivery of aceclofenac," *Aaps Pharmscitech*, vol. 8, no. 4, pp. 191–199, 2007.

[15] S. Shafiq, F. Shakeel, S. Talegaonkar, F. J. Ahmad, R. K. Khar, and M. Ali, "Development and bioavailability assessment of ramipril nanoemulsion formulation," *European journal of pharmaceutics and biopharmaceutics*, vol. 66, no. 2, pp. 227–243, 2007.

[16] A. C. Anselmo, M. Zhang, S. Kumar, *et al.*, "Elasticity of nanoparticles influences their blood circulation, phagocytosis, endocytosis, and targeting," *ACS nano*, vol. 9, no. 3, pp. 3169–3177, 2015.

[17] Y. Singh, J. G. Meher, K. Raval, *et al.*, "Nanoemulsion: Concepts, development and applications in drug delivery," *Journal of controlled release*, vol. 252, pp. 28–49, 2017.

[18] M. Yukuyama, D. Ghisleni, T. Pinto, and N. Bou-Chacra, "Nanoemulsion: Process selection and application in cosmetics–a review," *International journal of cosmetic science*, vol. 38, no. 1, pp. 13–24, 2016.

[19] L. Wang, X. Li, G. Zhang, J. Dong, and J. Eastoe, "Oil-in-water nanoemulsions for pesticide formulations," *Journal of colloid and interface science*, vol. 314, no. 1, pp. 230–235, 2007.

[20] T. Wirth, N. Parker, and S. Ylä-Herttuala, "History of gene therapy," *Gene*, vol. 525, no. 2, pp. 162–169, 2013.

[21] E. Tatum and J. Lederberg, "Gene recombination in the bacterium *Escherichia coli*," *Journal of bacteriology*, vol. 53, no. 6, pp. 673–684, 1947.

[22] N. D. Zinder and J. Lederberg, "Genetic exchange in *Salmonella*," *Journal of bacteriology*, vol. 64, no. 5, pp. 679–699, 1952.

[23] H. M. Temin, "Mixed infection with two types of Rous sarcoma virus," *Virology*, vol. 13, no. 2, pp. 158–163, 1961.

[24] E. H. Kaji and J. M. Leiden, "Gene and stem cell therapies," *Jama*, vol. 285, no. 5, pp. 545–550, 2001.

[25] G. Ermak, *Emerging medical technologies*. World scientific publishing company, 2015.

[26] N. Nayerossadat, T. Maedeh, and P. A. Ali, "Viral and nonviral delivery systems for gene delivery," *Advanced biomedical research*, vol. 1, 2012.

[27] K. K. Jain, "An overview of drug delivery systems," *Drug Delivery Systems*, pp. 1–54, 2020.

[28] S. L. Ginn, A. K. Amaya, I. E. Alexander, M. Edelstein, and M. R. Abedi, "Gene therapy clinical trials worldwide to 2017: An update," *The journal of gene medicine*, vol. 20, no. 5, e3015, 2018.

[29] C.-C. Ma, Z.-L. Wang, T. Xu, Z.-Y. He, and Y.-Q. Wei, "The approved gene therapy drugs worldwide: From 1998 to 2019," *Biotechnology advances*, vol. 40, p. 107 502, 2020.

[30] B. Shi, M. Zheng, W. Tao, *et al.*, "Challenges in DNA delivery and recent advances in multifunctional polymeric DNA delivery systems," *Biomacromolecules*, vol. 18, no. 8, pp. 2231–2246, 2017.

[31] S. Mali, "Delivery systems for gene therapy," *Indian journal of human genetics*, vol. 19, no. 1, p. 3, 2013.

[32] H. Xu, Z. Li, and J. Si, "Nanocarriers in gene therapy: A review," *Journal of biomedical nanotechnology*, vol. 10, no. 12, pp. 3483–3507, 2014.

[33] T. Xiong, Y. Li, F. Ni, and F. Zhang, "Monitoring of bystander effect of herpes simplex virus thymidine kinase/acyclovir system using fluorescence resonance energy transfer technique," *Journal of biomedical nanotechnology*, vol. 8, no. 1, pp. 74–79, 2012.

[34] R. Goyal, S. Tripathi, S. Tyagi, *et al.*, "Gellan gum-PEI nanocomposites as efficient gene delivery agents," *Journal of biomedical nanotechnology*, vol. 7, no. 1, pp. 38–39, 2011.

[35] B. J. Bevis and B. S. Glick, "Rapidly maturing variants of the *Discosoma* red fluorescent protein (DsRed)," *Nature biotechnology*, vol. 20, no. 1, pp. 83–87, 2002.

[36] M. V. Matz, A. F. Fradkov, Y. A. Labas, *et al.*, "Fluorescent proteins from nonbioluminescent *Anthozoa* species," *Nature biotechnology*, vol. 17, no. 10, pp. 969–973, 1999.

[37] A. Miyawaki, D. M. Shcherbakova, and V. V. Verkhusha, "Red fluorescent proteins: Chromophore formation and cellular applications," *Current opinion in structural biology*, vol. 22, no. 5, pp. 679–688, 2012.

[38] E. M. Merzlyak, J. Goedhart, D. Shcherbo, *et al.*, "Bright monomeric red fluorescent protein with an extended fluorescence lifetime," *Nature methods*, vol. 4, no. 7, pp. 555–557, 2007.

[39] S. Jakobs, V. Subramaniam, A. Schönle, T. M. Jovin, and S. W. Hell, "EGFP and DsRed expressing cultures of *Escherichia coli* imaged by confocal, two-photon and fluorescence lifetime microscopy," *FEBS letters*, vol. 479, no. 3, pp. 131–135, 2000.

[40] U. Lauf, P. Lopez, and M. M. Falk, "Expression of fluorescently tagged connexins: A novel approach to rescue function of oligomeric DsRed-tagged proteins1," *FEBS letters*, vol. 498, no. 1, pp. 11–15, 2001.

[41] G. S. Baird, D. A. Zacharias, and R. Y. Tsien, "Biochemistry, mutagenesis, and oligomerization of DsRed, a red fluorescent protein from coral," *Proceedings of the National Academy of Sciences*, vol. 97, no. 22, pp. 11 984–11 989, 2000.

[42] J. Wiehler, J. von Hummel, and B. Steipe, "Mutants of discosoma red fluorescent protein with a GFP-like chromophore," *FEBS letters*, vol. 487, no. 3, pp. 384–389, 2001.

[43] N. C. Shaner, R. E. Campbell, P. A. Steinbach, B. N. Giepmans, A. E. Palmer, and R. Y. Tsien, "Improved monomeric red, orange and yellow fluorescent proteins derived from *Discosoma sp.* red fluorescent protein," *Nature biotechnology*, vol. 22, no. 12, pp. 1567–1572, 2004.

[44] L. Wang, W. C. Jackson, P. A. Steinbach, and R. Y. Tsien, "Evolution of new nonantibody proteins via iterative somatic hypermutation," *Proceedings of the National Academy of Sciences*, vol. 101, no. 48, pp. 16 745–16 749, 2004.

[45] J. Petersen, P. G. Wilmann, T. Beddoe, *et al.*, "The 2.0-Å crystal structure of eqfp611, a far red fluorescent protein from the sea anemone entacmaea quadricolor," *Journal of biological chemistry*, vol. 278, no. 45, pp. 44 626–44 631, 2003.

[46] J. Wiedenmann, A. Schenk, C. Röcker, A. Girod, K.-D. Spindler, and G. U. Nienhaus, "A far-red fluorescent protein with fast maturation and reduced oligomerization tendency from entacmaea quadricolor (anthozoa, actinaria)," *Proceedings of the National Academy of Sciences*, vol. 99, no. 18, pp. 11 646–11 651, 2002.

[47] J. Wiedenmann, B. Vallone, F. Renzi, *et al.*, "Red fluorescent protein eqfp611 and its genetically engineered dimeric variants," *Journal of biomedical optics*, vol. 10, no. 1, p. 014 003, 2005.

[48] Research Collaboratory for Structural Bioinformatics Protein Data Bank. "TagRFP Structure." (2010), [Online]. Available: `https://www.rcsb.org/3d-view/3M22`. Accessed 22.04.2022.

[49] Evrogen. "Red Fluorescent Protein TagRFP." (), [Online]. Available: `https://evrogen.com/products/TagRFP/TagRFP_Detailed_description.shtml`. Accessed 25.04.2022.

[50] SnapGene. "pTagRFP-C Sequence." (), [Online]. Available: `https://www.snapgene.com/resources/plasmid-files/?set=fluorescent_protein_genes_and_plasmids&plasmid=pTagRFP-C`. Accessed 25.04.2022.

[51] Evrogen. "pTaRFP-C vector." (), [Online]. Available: `https://evrogen.com/products/vectors/pTagRFP-C/pTagRFP-C.shtml`. Accessed 25.04.2022.

[52] S. Chackalamannil, D. Rotella, and S. Ward, *Comprehensive medicinal chemistry III*. Elsevier, 2017.

[53] Y.-C. Kuo and C.-C. Wang, "Colloidal drug delivery system for brain-targeting therapy," *Colloid and Interface Science in Pharmaceutical Research and Development*, pp. 389–410, 2014.

[54] S. D. Conner and S. L. Schmid, "Regulated portals of entry into the cell," *Nature*, vol. 422, no. 6927, pp. 37–44, 2003.

[55] S. E. Gratton, P. A. Ropp, P. D. Pohlhaus, *et al.*, "The effect of particle design on cellular internalization pathways," *Proceedings of the National Academy of Sciences*, vol. 105, no. 33, pp. 11 613–11 618, 2008.

[56] Y. Zhao, Y. Zhang, F. Ning, D. Guo, and Z. Xu, "Synthesis and cellular biocompatibility of two kinds of hap with different nanocrystal morphology," *Journal of Biomedical Materials Research Part B: Applied Biomaterials: An Official Journal of The Society for Biomaterials, The Japanese Society for Biomaterials, and The Australian Society for Biomaterials and the Korean Society for Biomaterials*, vol. 83, no. 1, pp. 121–126, 2007.

[57] B. D. Chithrani, A. A. Ghazani, and W. C. Chan, "Determining the size and shape dependence of gold nanoparticle uptake into mammalian cells," *Nano letters*, vol. 6, no. 4, pp. 662–668, 2006.

[58] K. Xiao, Y. Li, J. Luo, *et al.*, "The effect of surface charge on in vivo biodistribution of peg-oligocholic acid based micellar nanoparticles," *Biomaterials*, vol. 32, no. 13, pp. 3435–3446, 2011.

[59] J.-L. Dewez, A. Doren, Y.-J. Schneider, and P. G. Rouxhet, "Competitive adsorption of proteins: Key of the relationship between substratum surface properties and adhesion of epithelial cells," *Biomaterials*, vol. 20, no. 6, pp. 547–559, 1999.

[60] A. Fasbender, J. Marshall, T. Moninger, T. Grunst, S. Cheng, and M. Welsh, "Effect of co-lipids in enhancing cationic lipid-mediated gene transfer in vitro and in vivo," *Gene therapy*, vol. 4, no. 7, pp. 716–725, 1997.

[61] C. Erni, C. Suard, S. Freitas, D. Dreher, H. P. Merkle, and E. Walter, "Evaluation of cationic solid lipid microparticles as synthetic carriers for the targeted delivery of macromolecules to phagocytic antigen-presenting cells," *Biomaterials*, vol. 23, no. 23, pp. 4667–4676, 2002.

[62] C. Wischke, H.-H. Borchert, J. Zimmermann, I. Siebenbrodt, and D. R. Lorenzen, "Stable cationic microparticles for enhanced model antigen delivery to dendritic cells," *Journal of Controlled Release*, vol. 114, no. 3, pp. 359–368, 2006.

[63] C. Thomas, V. Gupta, and F. Ahsan, "Influence of surface charge of plga particles of recombinant hepatitis b surface antigen in enhancing systemic and mucosal immune responses," *International journal of pharmaceutics*, vol. 379, no. 1, pp. 41–50, 2009.

[64] T.-H. Chung, S.-H. Wu, M. Yao, *et al.*, "The effect of surface charge on the uptake and biological function of mesoporous silica nanoparticles in 3t3-l1 cells and human mesenchymal stem cells," *Biomaterials*, vol. 28, no. 19, pp. 2959–2966, 2007.

[65] J. Rejman, V. Oberle, I. S. Zuhorn, and D. Hoekstra, "Size-dependent internalization of particles via the pathways of clathrin-and caveolae-mediated endocytosis," *Biochemical journal*, vol. 377, no. 1, pp. 159–169, 2004.

[66] M. P. Desai, V. Labhasetwar, E. Walter, R. J. Levy, and G. L. Amidon, "The mechanism of uptake of biodegradable microparticles in caco-2 cells is size dependent," *Pharmaceutical research*, vol. 14, no. 11, pp. 1568–1573, 1997.

[67] Y. Cai, Y. Liu, W. Yan, *et al.*, "Role of hydroxyapatite nanoparticle size in bone cell proliferation," *Journal of Materials Chemistry*, vol. 17, no. 36, pp. 3780–3787, 2007.

[68] I. Canton and G. Battaglia, "Endocytosis at the nanoscale," *Chemical Society Reviews*, vol. 41, no. 7, pp. 2718–2739, 2012.

[69] G. J. Doherty and H. T. McMahon, "Mechanisms of endocytosis," *Annual review of biochemistry*, vol. 78, pp. 857–902, 2009.

[70] G. Sahay, D. Y. Alakhova, and A. V. Kabanov, "Endocytosis of nanomedicines," *Journal of controlled release*, vol. 145, no. 3, pp. 182–195, 2010.

[71] H. T. McMahon and E. Boucrot, "Molecular mechanism and physiological functions of clathrin-mediated endocytosis," *Nature reviews Molecular cell biology*, vol. 12, no. 8, pp. 517–533, 2011.

[72] Q. Gong, C. Huntsman, and D. Ma, "Clathrin-independent internalization and recycling," *Journal of cellular and molecular medicine*, vol. 12, no. 1, pp. 126–144, 2008.

[73] S. Kumari, M. Swetha, and S. Mayor, "Endocytosis unplugged: Multiple ways to enter the cell," *Cell research*, vol. 20, no. 3, pp. 256–275, 2010.

[74] L. Pelkmans and A. Helenius, "Endocytosis via caveolae," *Traffic*, vol. 3, no. 5, pp. 311–320, 2002.

[75] J. Rejman, M. Conese, and D. Hoekstra, "Gene transfer by means of lipo- and polyplexes: Role of clathrin and caveolae-mediated endocytosis," *Journal of liposome research*, vol. 16, no. 3, pp. 237–247, 2006.

[76] G. L. Rosano and E. A. Ceccarelli, "Recombinant protein expression in escherichia coli: Advances and challenges," *Frontiers in microbiology*, vol. 5, p. 172, 2014.

[77] J. Y. Lim, J. W. Yoon, and C. J. Hovde, "A brief overview of escherichia coli o157: H7 and its plasmid o157," *Journal of microbiology and biotechnology*, vol. 20, no. 1, p. 5, 2010.

[78] M. Kostylev, A. E. Otwell, R. E. Richardson, and Y. Suzuki, "Cloning should be simple: Escherichia coli dh5α-mediated assembly of multiple dna fragments with short end homologies," *PLoS One*, vol. 10, no. 9, 2015.

[79] M. Ivanković, A. Ćukušić, I. Gotić, *et al.*, "Telomerase activity in hela cervical carcinoma cell line proliferation," *Biogerontology*, vol. 8, no. 2, pp. 163–172, 2007.

[80] V. Smith, "Wonder woman: The life, death, and life after death of henrietta lacks, unwitting heroine of modern medical science," *Baltimore City Paper*, vol. 17, 2002.

[81] P. Scholz and C. M. Keck, "Nanoemulsions produced by rotor–stator high speed stirring," *International journal of pharmaceutics*, vol. 482, no. 1-2, pp. 110–117, 2015.

[82] J. B. Aswathanarayan and R. R. Vittal, "Nanoemulsions and their potential applications in food industry," *Frontiers in Sustainable Food Systems*, vol. 3, p. 95, 2019.

[83] R. P. Patel and J. R. Joshi, "An overview on nanoemulsion: A novel approach," *International Journal of Pharmaceutical Sciences and Research*, vol. 3, no. 12, p. 4640, 2012.

[84] A. Gupta, H. B. Eral, T. A. Hatton, and P. S. Doyle, "Nanoemulsions: Formation, properties and applications," *Soft matter*, vol. 12, no. 11, pp. 2826–2841, 2016.

[85] P. J. Espitia, C. A. Fuenmayor, and C. G. Otoni, "Nanoemulsions: Synthesis, characterization, and application in bio-based active food packaging," *Comprehensive Reviews in Food Science and Food Safety*, vol. 18, no. 1, pp. 264–285, 2019.

[86] N. Sharma, M. Bansal, S. Visht, P. Sharma, G. Kulkarni, *et al.*, "Nanoemulsion: A new concept of delivery system," *Chronicles of Young Scientists*, vol. 1, no. 2, pp. 2–6, 2010.

[87] P. Shah, D. Bhalodia, and P. Shelat, "Nanoemulsion: A pharmaceutical review.," *Systematic reviews in pharmacy*, vol. 1, no. 1, 2010.

[88] K. Schroën, J. de Ruiter, and C. Berton-Carabin, "The importance of interfacial tension in emulsification: Connecting scaling relations used in large scale preparation with microfluidic measurement methods," *ChemEngineering*, vol. 4, no. 4, p. 63, 2020.

[89] Y. Zhang and H. Liu, "Physics of multiphase microflows and microdroplets," in *Microdroplet Technology*, Springer, 2012, pp. 1–21.

[90] S. J. Gaskell, "Electrospray: Principles and practice," *Journal of mass spectrometry*, vol. 32, no. 7, pp. 677–688, 1997.

[91] M. Wilm, "Principles of electrospray ionization," *Molecular & cellular proteomics*, vol. 10, no. 7, 2011.

[92] J. B. Fenn, M. Mann, C. K. Meng, S. F. Wong, and C. M. Whitehouse, "Electrospray ionization for mass spectrometry of large biomolecules," *Science*, vol. 246, no. 4926, pp. 64–71, 1989.

[93] N. Bhardwaj and S. C. Kundu, "Electrospinning: A fascinating fiber fabrication technique," *Biotechnology advances*, vol. 28, no. 3, pp. 325–347, 2010.

[94] O. V. Salata, "Tools of nanotechnology: Electrospray," *Current nanoscience*, vol. 1, no. 1, pp. 25–33, 2005.

[95] N. Radacsi, R. Ambrus, T. Szunyogh, *et al.*, "Electrospray crystallization for nanosized pharmaceuticals with improved properties," *Crystal growth & design*, vol. 12, no. 7, pp. 3514–3520, 2012.

[96] Y. Wu, B. Yu, A. Jackson, W. Zha, L. J. Lee, and B. E. Wyslouzil, "Coaxial electrohydrodynamic spraying: A novel one-step technique to prepare oligodeoxynucleotide encapsulated lipoplex nanoparticles," *Molecular pharmaceutics*, vol. 6, no. 5, pp. 1371–1379, 2009.

[97] A. D. Duong, S. Sharma, K. J. Peine, *et al.*, "Electrospray encapsulation of toll-like receptor agonist resiquimod in polymer microparticles for the treatment of visceral leishmaniasis," *Molecular pharmaceutics*, vol. 10, no. 3, pp. 1045–1055, 2013.

[98] A. Maali and M. H. Mosavian, "Preparation and application of nanoemulsions in the last decade (2000–2010)," *Journal of dispersion science and technology*, vol. 34, no. 1, pp. 92–105, 2013.

[99] N. H. Che Marzuki, R. A. Wahab, and M. Abdul Hamid, "An overview of nanoemulsion: Concepts of development and cosmeceutical applications," *Biotechnology & biotechnological equipment*, vol. 33, no. 1, pp. 779–797, 2019.

[100] A. Håkansson and M. Rayner, "General Principles of Nanoemulsion Formation by High-Energy Mechanical Methods," in *Nanoemulsions*, Elsevier, 2018, pp. 103–139.

[101] Homogenizers part of Laboratory Supply Network. "Rotor stator homogenizers." (), [Online]. Available: `https://homogenizers.net/collections/rotor-stator-homogenizers` (visited on 10/07/2021).

[102] A. T. Utomo, M. Baker, and A. W. Pacek, "Flow pattern, periodicity and energy dissipation in a batch rotor–stator mixer," *Chemical engineering research and design*, vol. 86, no. 12, pp. 1397–1409, 2008.

[103] A. O'Driscoll. "Rotor stator homogenizers." (2019), [Online]. Available: `https://homogenizers.net/blogs/blog/forces-involved-in-homogenization` (visited on 10/08/2021).

[104] T. G. Mason, J. N. Wilking, K. Meleson, C. B. Chang, and S. M. Graves, "Nanoemulsions: Formation, structure, and physical properties," *Journal of Physics: condensed matter*, vol. 18, no. 41, R635, 2006.

[105] P. Tabeling, *Introduction to microfluidics*. OUP Oxford, 2005.

[106] S. Colin, *Microfluidics*. John Wiley & Sons, 2010.

[107] C. Kleinstreuer, *Microfluidics and nanofluidics: theory and selected applications*. John Wiley & Sons, 2013.

[108] P. Zhu and L. Wang, "Passive and active droplet generation with microfluidics: A review," *Lab on a Chip*, vol. 17, no. 1, pp. 34–75, 2017.

[109] D. Chakraborty and S. Chakraborty, "Microfluidic transport and micro-scale flow physics: An overview," *Microfluidics and Microfabrication*, pp. 1–85, 2010.

[110] H. Fatoyinbo and X. J. Li, "Microfluidic devices for cell manipulation," in *Microfluidic Devices for Biomedical Applications*, Elsevier, 2021, pp. 329–389.

[111] B. J. Kirby, *Micro-and nanoscale fluid mechanics: transport in microfluidic devices*. Cambridge university press, 2010.

[112] K. Loizou, V.-L. Wong, and B. Hewakandamby, "Examining the effect of flow rate ratio on droplet generation and regime transition in a microfluidic t-junction at constant capillary numbers," *Inventions*, vol. 3, no. 3, p. 54, 2018.

[113] H. N. Joensson and H. Andersson Svahn, "Droplet microfluidics—a tool for single-cell analysis," *Angewandte Chemie International Edition*, vol. 51, no. 49, pp. 12 176–12 192, 2012.

[114] P. Garstecki, M. J. Fuerstman, H. A. Stone, and G. M. Whitesides, "Formation of droplets and bubbles in a microfluidic t-junction—scaling and mechanism of break-up," *Lab on a Chip*, vol. 6, no. 3, pp. 437–446, 2006.

[115] M. De Menech, P. Garstecki, F. Jousse, and H. A. Stone, "Transition from squeezing to dripping in a microfluidic t-shaped junction," *journal of fluid mechanics*, vol. 595, pp. 141–161, 2008.

[116] S. L. Anna, "Droplets and bubbles in microfluidic devices," *Annual Review of Fluid Mechanics*, vol. 48, pp. 285–309, 2016.

[117] Z. Li and T. Ngai, "Microgel particles at the fluid–fluid interfaces," *Nanoscale*, vol. 5, no. 4, pp. 1399–1410, 2013.

[118] M. Antonietti, "Microgels," in *Encyclopedia of Materials: Science and Technology*, K. J. Buschow, R. W. Cahn, M. C. Flemings, *et al.*, Eds., Elsevier, 2001, pp. 5635–5636.

[119] M. Das, H. Zhang, and E. Kumacheva, "Microgels: Old materials with new applications," *Annu. Rev. Mater. Res.*, vol. 36, pp. 117–142, 2006.

[120] L. Gasperini, J. F. Mano, and R. L. Reis, "Natural polymers for the microencapsulation of cells," *Journal of the Royal Society Interface*, vol. 11, no. 100, p. 20 140 817, 2014.

[121] U. Remminghorst and B. H. Rehm, "Bacterial alginates: From biosynthesis to applications," *Biotechnology letters*, vol. 28, no. 21, pp. 1701–1712, 2006.

[122] R. Narayanaswamy, S. Kanagesan, A. Pandurangan, and P. Padmanabhan, "Basics to different imaging techniques, different nanobiomaterials for image enhancement," in *Nanobiomaterials in Medical Imaging*, Elsevier, 2016, pp. 101–129.

[123] G. A. Martău, M. Mihai, and D. C. Vodnar, "The use of chitosan, alginate, and pectin in the biomedical and food sector—biocompatibility, bioadhesiveness, and biodegradability," *Polymers*, vol. 11, no. 11, p. 1837, 2019.

[124] J.-Y. Leong, W.-H. Lam, K.-W. Ho, *et al.*, "Advances in fabricating spherical alginate hydrogels with controlled particle designs by ionotropic gelation as encapsulation systems," *Particuology*, vol. 24, pp. 44–60, 2016.

[125] L. Theodore and F. Ricci, *Mass transfer operations for the practicing engineer*. Wiley Online Library, 2010.

[126] J. Horvath, "A brief history of 3d printing," in *Mastering 3D Printing*, Springer, 2014, pp. 3–10.

[127] I. Gibson, D. Rosen, B. Stucker, and M. Khorasani, "Introduction and basic principles," in *Additive manufacturing technologies*, Springer, 2021, pp. 1–21.

[128] E. Sachs, M. Cima, P. Williams, D. Brancazio, and J. Cornie, "Three dimensional printing: Rapid tooling and prototypes directly from a cad model," 1992.

[129] J. Horvath, "The desktop 3d printer," in *Mastering 3D Printing*, Springer, 2014, pp. 11–20.

[130] N. Shahrubudin, T. C. Lee, and R. Ramlan, "An overview on 3d printing technology: Technological, materials, and applications," *Procedia Manufacturing*, vol. 35, pp. 1286–1296, 2019.

[131] Y.-C. Wang, T. Chen, and Y.-L. Yeh, "Advanced 3d printing technologies for the aircraft industry: A fuzzy systematic approach for assessing the critical factors," *The International Journal of Advanced Manufacturing Technology*, vol. 105, no. 10, pp. 4059–4069, 2019.

[132] V. Sreehitha, "Impact of 3d printing in automotive industry," *International Journal of Mechanical and Production Engineering*, vol. 5, no. 2, pp. 91–94, 2017.

[133] C. Y. Foo, H. N. Lim, M. A. Mahdi, M. H. Wahid, and N. M. Huang, "Three-dimensional printed electrode and its novel applications in electronic devices," *Scientific reports*, vol. 8, no. 1, pp. 1–11, 2018.

[134] Z. Liu, M. Zhang, B. Bhandari, and Y. Wang, "3d printing: Printing precision and application in food sector," *Trends in Food Science & Technology*, vol. 69, pp. 83–94, 2017.

[135] J. Norman, R. D. Madurawe, C. M. Moore, M. A. Khan, and A. Khairuzzaman, "A new chapter in pharmaceutical manufacturing: 3d-printed drug products," *Advanced drug delivery reviews*, vol. 108, pp. 39–50, 2017.

[136] A. De Mori, M. Peña Fernández, G. Blunn, G. Tozzi, and M. Roldo, "3d printing and electrospinning of composite hydrogels for cartilage and bone tissue engineering," *Polymers*, vol. 10, no. 3, p. 285, 2018.

[137] L. Xu and C. Siedlecki, "Surface texturing and control of bacterial adhesion," in *Comprehensive Biomaterials II*, Elsevier, 2017, pp. 303–320.

[138] B. S. Yilbas, A. Al-Sharafi, and H. Ali, "Chapter 3 - surfaces for self-cleaning," in *Self-Cleaning of Surfaces and Water Droplet Mobility*, Elsevier, 2019, pp. 45–98.

[139] Z. Ahmad and A. M. Rahman, "Plastics in waveguide application," in *Reference Module in Materials Science and Materials Engineering*, Elsevier, 2021.

[140] K. Anselme, P. Davidson, A. Popa, M. Giazzon, M. Liley, and L. Ploux, "The interaction of cells and bacteria with surfaces structured at the nanometre scale," *Acta biomaterialia*, vol. 6, no. 10, pp. 3824–3846, 2010.

[141] R. Martinez-Duarte and M. Madou, "Su-8 photolithography and its impact on microfluidics," *Microfluidics and nanofluidics handbook*, no. 2006, pp. 231–268, 2011.

[142] A. del Campo and C. Greiner, "Su-8: A photoresist for high-aspect-ratio and 3d submicron lithography," *Journal of micromechanics and microengineering*, vol. 17, no. 6, R81, 2007.

[143] J. Liu, B. Cai, J. Zhu, *et al.*, "Process research of high aspect ratio microstructure using su-8 resist," *Microsystem Technologies*, vol. 10, no. 4, pp. 265–268, 2004.

[144] B. Carr and M. Wright, "Nanoparticle tracking analysis," *Innovations in Pharmaceutical Technology*, vol. 26, pp. 38–40, 2008.

[145] D. McMullan, "Scanning electron microscopy 1928–1965," *Scanning*, vol. 17, no. 3, pp. 175–185, 1995.

[146] K. Akhtar, S. A. Khan, S. B. Khan, and A. M. Asiri, "Scanning electron microscopy: Principle and applications in nanomaterials characterization," in *Handbook of materials characterization*, Springer, 2018, pp. 113–145.

[147] D. Newbury, "Image formation in the scanning electron microscope," in *Practical scanning electron microscopy*, Springer, 1975, pp. 95–148.

[148] R. Heu, S. Shahbazmohamadi, J. Yorston, and P. Capeder, "Target material selection for sputter coating of sem samples," *Microscopy Today*, vol. 27, no. 4, pp. 32–36, 2019.

[149] I. C. Ghiran, "Introduction to fluorescence microscopy," in *Light microscopy*, Springer, 2011, pp. 93–136.

[150] J. W. Lichtman and J.-A. Conchello, "Fluorescence microscopy," *Nature methods*, vol. 2, no. 12, pp. 910–919, 2005.

[151] M. J. Sanderson, I. Smith, I. Parker, and M. D. Bootman, "Fluorescence microscopy," *Cold Spring Harbor Protocols*, vol. 2014, no. 10, pdb–top071795, 2014.

[152] A. Diaspro, P. Bianchini, F. C. Zanacchi, *et al.*, "Fluorescence microscopy," in *Springer Handbook of Microscopy*, Springer, 2019, pp. 1039–1088.

[153] J. B. Birks, "Photophysics of aromatic molecules," 1970.

[154] Spring, Kenneth R. and Davidson, Michael W. "Introduction to fluorescence microscopy." (), [Online]. Available: `https://www.microscopyu.com/techniques/fluorescence/introduction-to-fluorescence-microscopy`. Accessed 29.09.2021.

[155] D. J. Arndt-Jovin, M. Robert-Nicoud, S. J. Kaufman, and T. M. Jovin, "Fluorescence digital imaging microscopy in cell biology," *Science*, vol. 230, no. 4723, pp. 247–256, 1985.

[156] Abramowitz, Mortimer and Davidson, Michael W. "Fluorescence filters." (), [Online]. Available: https://www.olympus-lifescience.com/es/microscope-resource/primer/techniques/fluorescence/filters/. Accessed 10.11.2021.

[157] S. M. Sze and M.-K. Lee, "MOS Capacitor and MOSFET," in *Springer Handbook of Microscopy*, Wiley Global Education, 2012, pp. 160–194.

[158] Piston, David W. and Patterson, George H. and Lippincott-Schwartz, Jennifer and Claxton, Nathan S. and Davidson,Michael W. "Imaging Fluorescent Proteins." (), [Online]. Available: https://www.microscopyu.com/techniques/fluorescence/fluorescent-protein-imaging-parameters. Accessed 11.11.2021.

[159] A. Venkatanarayanan and E. Spain, "Review of recent developments in sensing materials," 2014.

[160] R. Hui, "Photodetectors," in *Introduction to Fiber-Optic Communications*, Academic Press, 2020, pp. 125–154.

[161] Autodesk. "What is AutoCAD?" (), [Online]. Available: https://www.autodesk.com/products/autocad/overview?term=1-YEAR&tab=subscription. Accessed 16.11.2021.

[162] T. Ferreira and W. Rasband, "ImageJ user guide," *ImageJ/Fiji*, vol. 1, pp. 155–161, 2012.

[163] C. A. Schneider, W. S. Rasband, and K. W. Eliceiri, "NIH Image to ImageJ: 25 years of image analysis," *Nature methods*, vol. 9, no. 7, pp. 671–675, 2012.

[164] V. Girish, A. Vijayalakshmi, *et al.*, "Affordable image analysis using nih image/imagej," *Indian journal of cancer*, vol. 41, no. 1, p. 47, 2004.

[165] LayoutEditor. "LayoutEditor: Basics." (), [Online]. Available: https://layouteditor.org/. Accessed: 24.11.2021.

[166] ——, "LayoutEditor: Macros/Scripting." (), [Online]. Available: https://layouteditor.org/layoutscript. Accessed: 24.11.2021.

[167] Thies, Jurgen. "Introduction: LayoutEditor." (2016), [Online]. Available: http://www.layouteditor.net/wiki/Introduction. Accessed: 24.11.2021.

[168] COMSOL Multiphysics. "CFD module user's guide." (2018), [Online]. Available: https://doc.comsol.com/5.6/docserer/#!/com.comsol.help.cfd/html_CFDModuleManual.html. Accessed: 29.11.2021.

[169] B. Binks and S. Lumsdon, "Effects of oil type and aqueous phase composition on oil–water mixtures containing particles of intermediate hydrophobicity," *Physical Chemistry Chemical Physics*, vol. 2, no. 13, pp. 2959–2967, 2000.

[170] B. P. Binks and C. Whitby, "Temperature-dependent stability of water-in-undecanol emulsions," *Colloids and Surfaces A: Physicochemical and Engineering Aspects*, vol. 224, no. 1-3, pp. 241–249, 2003.

[171] Anycubic. "Anycubic Photon S Technical Data." (), [Online]. Available: `https://www.anycubic.com/products/anycubic-photon-s?variant=30084941283388`. Accessed 18.02.2022.

[172] D. Joubert, J. van Zyl, A. Hawtrey, and M. Ariatti, "A note on poly-l-lysine-mediated gene transfer in hela cells," *Drug Delivery*, vol. 10, no. 3, pp. 209–211, 2003.

[173] C. Clausen Fynbo, M. Undall-Behrend Djernæs, and T. Israeli, "Cell Encapsulation in Alginate Microgels Fabricated with a Microfluidic Droplet Generator," Unpublished, 2020.

[174] C. Úbeda Nicolau, K. Møller Kristiansen, and O. Pihl Christiansen, "Microfluidic chip design for continuous transfection and encapsulation of *Pichia Pastoris*," Unpublished, 2021.

[175] F. J. Preiss, T. Dagenbach, M. Fischer, and H. P. Karbstein, "Development of a pressure stable inline droplet generator with live droplet size measurement," *ChemEngineering*, vol. 4, no. 4, p. 60, 2020.

[176] H. K. Sharma and J. Dutta, "Effect of physical parameters on droplet generation in two-phase flow microfluidics t-junction," *International Journal of Innovative Research in Science, Engineering and Technology*, vol. 5, pp. 484–490, 2016.

[177] S. Orrenius and P. Nicotera, "The calcium ion and cell death.," *Journal of neural transmission. Supplementum*, vol. 43, pp. 1–11, 1994.

[178] P. Pinton, C. Giorgi, R. Siviero, E. Zecchini, and R. Rizzuto, "Calcium and apoptosis: Er-mitochondria ca2+ transfer in the control of apoptosis," *Oncogene*, vol. 27, no. 50, pp. 6407–6418, 2008.

[179] M. J. Berridge, M. D. Bootman, and H. L. Roderick, "Calcium signalling: Dynamics, homeostasis and remodelling," *Nature reviews Molecular cell biology*, vol. 4, no. 7, pp. 517–529, 2003.

[180] R. Rizzuto and T. Pozzan, "Microdomains of intracellular ca2+: Molecular determinants and functional consequences," *Physiological reviews*, vol. 86, no. 1, pp. 369–408, 2006.

[181] M. J. Rosendo-Pineda, C. M. Moreno, and L. Vaca, "Role of ion channels during cell division," *Cell Calcium*, vol. 91, p. 102 258, 2020.

Appendices

Appendix A

Thread Design

A M5x0.5 nut was designed with AutoCAD to be able to connect the syringe-pump to the microfluidic chips.

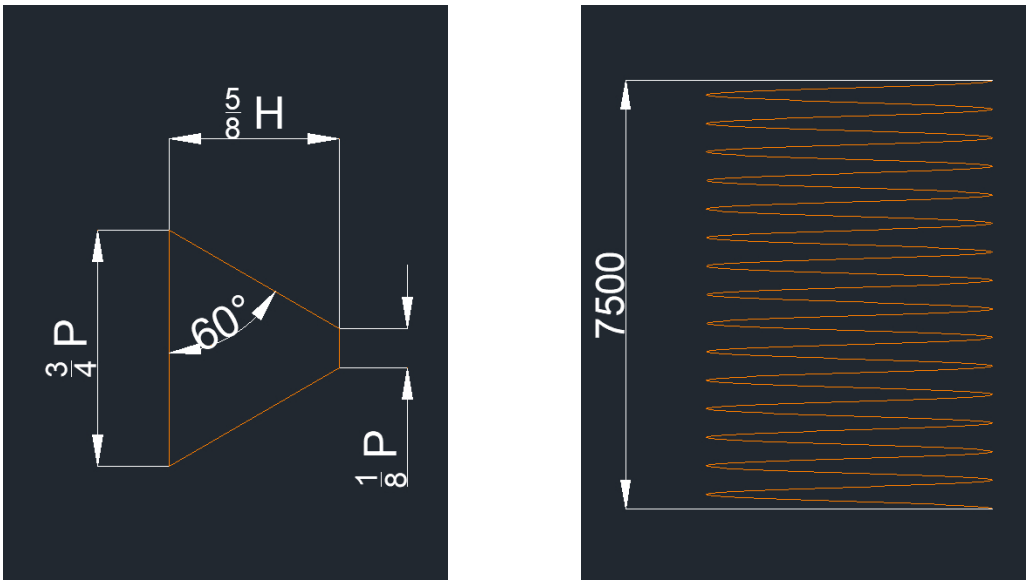

a) **b)**

Figure A.1. Screenshot of AutoCAD. Dimensions of the thread path and pitch of the M5x0.5 nut adapter. **a)** thread pitch, **b)** thread helical path. Dimensions are in micrometres.

The thread was created by doing a sweep of the pitch figure A.1 **a)**, along the helical path figure A.1 **b)**. The helical path had a radius of 2.5 mm, total length of 7.5 mm, a turn height of 0.5 mm, and a total of 15 turns. The sweep was carried out by setting as a base point the bottom right corner of the pitch to the top end of the path. The dimensions used for both path, and pitch are ISO standard for a M5x0.5 thread, where P is the pitch, and H is calculated according to equation A.1, where θ for a metric thread with M form type, is 60°.

$$H = \frac{1}{2 \cdot \tan\theta} \cdot P \tag{A.1}$$

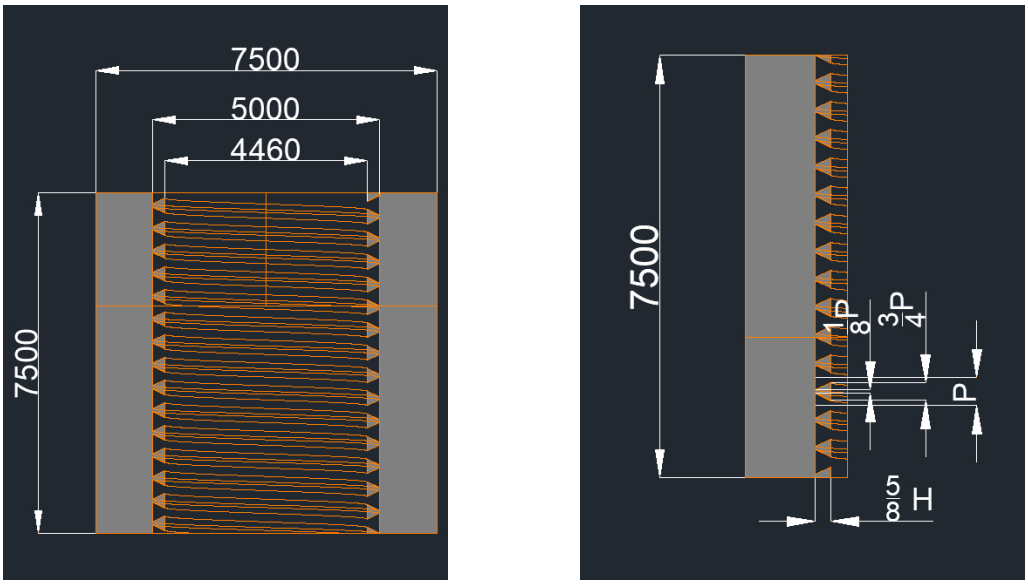

a) **b)**

Figure A.2. Screenshot of AutoCAD. Cross-section with the dimensions of the final adapter. **a)** cross-section of the whole nut, and **b)** cross-section of half nut. Dimensions are in micrometers.

The final nut was created by adding the thread from a 2.5 mm thick circle with inner diameter of 5 mm as shown in figure A.2. The final nut had a total height and external diameter of 7.5 mm. The major inner diameter was 5 mm, while the minor inner diameter was 4.46 mm. In figure A.2 **b)** it can be observed that the nut is the result of the addition of the thread to the circle.